

Dissecting the role of the mitochondrial carrier SLC25A47

Présentée le 26 août 2022

Faculté des sciences de la vie
Groupe Schoonjans (SV)
Programme doctoral en approches moléculaires du vivant

pour l'obtention du grade de Docteur ès Sciences

par

Nadia BRESCIANI

Acceptée sur proposition du jury

Dr C. Canto Alvarez, président du jury
Prof. K. Schoonjans, directrice de thèse
Prof. K. Sakamoto, rapporteur
Prof. S. Houten, rapporteur
Prof. M. Dal Peraro, rapporteur

Unbowed, unbent, unbroken

Acknowledgements

First of all, I would like to thank Prof. Kristina Schoonjans for the opportunity to perform my doctoral studies in her group, even without having any previous experience in the field of hepatic metabolism. I am grateful to all my colleagues that during these 4.5 years helped me going through my PhD. In particular, big thanks to Vera that taught me everything I know about mitochondria and was very patient in guiding me during my first year. Thanks to Alessia P. for the endless suggestions, for the long phone calls and the nice dinners (thanks to Carlo as well!). I would like to thank Hadrien for the help with the paper, for the never-ending *in vivo* experiments, for all the brainstorming, for the boat trips and great celebrations. Finally, thank you Ece and Yu for the mental (and also technical) support and for our nice chats; we went through the same rollercoaster of emotions during our PhD studies and it was very nice to have you by my side. Also, thanks to Francesca, Andie, Laura, Alex, Jérôme and Antoine for the help and support in- and outside the lab. I would like to thank Johan Auwerx and the members of his lab, especially Xiaoxu, Alexis B., Tanes, Alessia DM, Arwen, Gaby, Giacomo, Maria, Maxime, Ludger, Tertyty, Sandra for all the scientific and non-scientific discussions, for the Friday nights and all the funny dinners. A huge *thank you* goes to the tech team, Sabrina, Thibaud, Marie, Borany, Fabiana, Penelope and Carla that always said yes to all my help requests.

My Swiss life would have never been the same without the “Italians”, Carlotta, Jacopo, Nico, Chiara, Matteo, Luca, Georgie, Ema. Thanks for all our adventures and great time together!

I would also like to thank the *Buddies*, Aleksa, JP, Marco, Vale, Gabri and AP, for the quiz nights, the wild parties and memorable holidays!

Moreover, I really need to thank the people outside the “EPFL bubble” and, in particular, the girls from the Crossfit Venoge family: Harmonie, Andrea, Amira, Sabrina, Anna, Kristi, Nat, Tamires. You taught me that giving up is never an option!

Of course, I need to express my profound gratitude to my family, my mum, my brother, my grandparents, for the constant support and for giving me the opportunity to become the person (and the scientist) that I am now.

Infinite thanks to my best friends, Silvia, Flavia, Irene, Benny, Clelia, Stup, Dario, Puffo and Teo that have always been there for me and always believed in me (and in the fact that I could eventually win a Nobel prize). Thanks to Giulia and Laura, fellow *disadattate*, for our nice weekends, great memories, amazing talks and nasty Whatsapp discussions.

Thanks to all my friends that I cannot put in any “category”. Gio, thanks for the motivation to read One Piece and watch TV series and for all our combined hatefulness. Marco, Matteo and Lucia, thank you for being there for me even if we see each other once a year.

To conclude, my deepest gratitude goes to Mario, for saving my life in multiple occasions, for believing in me even when I wanted to quit everything. I will not be here, concluding my PhD studies, without him.

Table of Contents

List of Abbreviations.....	7
Summary.....	9
Riassunto.....	10
CHAPTER 1 Introduction	11
1.1 The liver: an integrative managing center	12
1.1.1 Hepatic roles in metabolic homeostasis.....	12
1.1.2 Hepatic metabolic flexibility	16
1.2 Mitochondria as hubs of intermediary metabolism.....	16
1.2.1 Mitochondrial structure and genome.....	16
1.2.2 Mitochondrial metabolic function	18
1.2.3 Mitochondrial stress signaling.....	20
1.3 Mitochondrial membrane transporters	23
1.3.1 SLC25 family	24
1.4.1 SLC25A47: an orphan mitochondrial carrier.....	27
CHAPTER 2 SLC25A47 is a novel determinant of hepatic mitochondrial function	28
2.1 Slc25a47 is a hepatocyte-specific mitochondrial carrier	29
2.2 Slc25a47-deficient mice display hepatic metabolic dysregulation	33
2.3 Hepatic Slc25a47 deficiency leads to impaired mitochondrial respiration	36
2.4 Slc25a47 deficiency leads to a strong induction of the mitochondrial stress response.....	38
2.5 Partial ablation of Slc25a47 is sufficient to trigger mitochondrial dysfunction.....	40
2.6 FGF21-dependent systemic phenotypes upon loss of Slc25a47	41
2.7 FGF21-independent hepatic phenotypes upon loss of Slc25a47	43
2.8 Disruption of SLC25A47 in hepatocytes predisposes to liver fibrosis.....	45
CHAPTER 3 Experimental procedures	48
CHAPTER 4 Discussion and perspectives	58
4.1. Discussion.....	59
4.2. Perspectives	60
4.2.1 SLC25A47 structure.....	60
4.2.2 SLC25A47 function.....	61
Curriculum Vitae.....	63
References.....	65

List of Abbreviations

ADM2, adrenomedullin 2

ALAT, alanine aminotransferase

ASAT, aspartate transaminase

ATF4, activating transcription factor 4

ATF5, activating transcription factor 5

BA, bile acid

ChIP, chromatin immunoprecipitation

CHOP, C/EBP homologous protein

ChREBP, carbohydrate response element binding protein

CI, complex I (OXPHOS)

COXIV, cytochrome c oxidase subunit 4

CoQ, coenzyme Q

CS, citrate synthase

EE, energy expenditure

EM, electron microscopy

ETC, electron transport chain

FA, fatty acid

FAO, fatty acids oxidation

FCCP, carbonyl cyanide-p-trifluoromethoxyphenylhydrazone;

FGF21, fibroblast growth factor 21

GDF15, growth differentiation factor 15

GSEA, gene set enrichment analysis

HCC, hepatocellular carcinoma

HFHS, high-fat high-sucrose

IMM, inner mitochondrial membrane

IMS, intermembrane space

ISR, integrated stress response

ITT, insulin tolerance test

KO, knockout

LDL, low density lipoproteins

LOF, loss-of-function

MSR, mitochondrial stress response

NASH, non-alcoholic steatohepatitis

OCR, oxygen consumption rate

OGTT, oral glucose tolerance test

OLIGO, oligomycin

OMM, outer mitochondrial membrane

OXPHOS, oxidative phosphorylation

PCA, principal component analysis

PKA, protein kinase A

PTM, post translational modifications

PTT, pyruvate tolerance test

scWAT: subcutaneous white adipose tissue

SLC, solute carrier

SUC, succinate

T2D, type 2 diabetes

TCA, tricarboxylic acid

TEM, transmission electron microscopy

TG, triglyceride

UCP, uncoupling protein

UPR^{mt}, mitochondrial unfolded protein response

VLDL, very-low-density lipoproteins

WAT, white adipose tissue

Summary

Transporters of the SLC25 mitochondrial carrier superfamily bridge cytoplasmic and mitochondrial metabolism by channeling metabolites across mitochondrial membranes and are pivotal for metabolic homeostasis. Despite their physiological relevance as gatekeepers of cellular metabolism, most of the SLC25 family members remain uncharacterized. During my PhD studies, I investigated the function of SLC25A47, an orphan carrier uniquely expressed in hepatocytes.

We used a murine loss-of-function (LOF) model to unravel the role of this transporter in mitochondrial and hepatic homeostasis. *Slc25a47*^{hep-/-} mice displayed a wide variety of metabolic abnormalities, as a result of sustained energy deficiency in the liver originating from impaired mitochondrial respiration in this organ. This mitochondrial phenotype was associated with a robust activation of the mitochondrial stress response (MSR) in the liver, which in turn, induced the secretion of several mitokines, amongst which FGF21 played a preponderant role in the translation of the effects of the MSR on systemic physiology. To dissect the FGF21-dependent and -independent physiological changes induced by the loss of *Slc25a47*, we generated a double *Slc25a47-Fgf21* LOF mouse model, and demonstrated that several aspects of the hypermetabolic state were entirely driven by hepatic secretion of FGF21. On the other hand, the metabolic fuel inflexibility induced by loss of *Slc25a47* could not be rescued by genetic removal of *Fgf21*. Finally, we challenged *Slc25a47*^{hep-/-} mice with high-fat high-sucrose (HFHS) diet and observed the development of liver fibrosis. Collectively, the data presented in this thesis show that SLC25A47 is a novel determinant of hepatic metabolism and place this carrier at the center of mitochondrial homeostasis.

Keywords: Mitochondria; Mitochondrial transporter; SLC25 family; Mitochondrial Stress Response; FGF21; Hepatic Metabolism; Fibrosis

Riassunto

I trasportatori della superfamiglia di trasportatori mitocondriali SLC25 sono fondamentali per la regolazione dell'omeostasi metabolica e connettono il metabolismo citoplasmatico a quello mitocondriale regolando lo scambio di metaboliti tra questi due compartimenti intracellulari. Nonostante la loro rilevanza fisiologica come *guardiani* del metabolismo cellulare, molti membri della famiglia SLC25 sono ancora poco caratterizzati.

Durante il mio dottorato ho studiato le funzioni fisiologiche di SLC25A47, un trasportatore orfano unicamente espresso negli epatociti.

Per raggiungere questo obiettivo, e comprendere il ruolo di questo trasportatore nel contesto del metabolismo epatico e mitocondriale, abbiamo usato un modello animale (murino) caratterizzato dalla delezione epatica di SLC25A47. I topi *Slc25a47^{hep-/-}* mostrano una grande varietà di anomalie metaboliche dovute alla perenne deficienza epatica di energia, che deriva da una compromessa respirazione mitocondriale negli epatociti. Nel fegato, questo fenotipo mitocondriale risulta associato a una massiccia attivazione della *risposta allo stress mitocondriale* (MSR) che, a sua volta, induce la secrezione di mitochine. Tra le diverse mitochine sovra-regolate nei topi *Slc25a47^{hep-/-}*, FGF21 gioca un ruolo fondamentale nel tradurre gli effetti della MSR agli altri organi. Per meglio studiare i cambiamenti fisiologici indotti dalla mancanza di *Slc25a47*, e per capire quali sono quelli dipendenti (o indipendenti) da FGF21, abbiamo generato un modello murino con una doppia delezione di *Slc25a47* e *Fgf21*. Con questi topi abbiamo quindi dimostrato che molti aspetti dell'iper-metabolismo osservato nei topi *Slc25a47^{hep-/-}* sono, in realtà, completamente dipendenti dalla secrezione di FGF21. Al contrario, i topi affetti dalla mancanza di entrambi *Slc25a47* e *Fgf21*, continuano a presentare inflessibilità metabolica, dimostrando che quest'ultima è indipendente dalla produzione epatica di FGF21 nel contesto del nostro modello animale. Inoltre, abbiamo somministrato ai topi *Slc25a47^{hep-/-}* una dieta ad alto contenuto di grassi e zuccheri (HFHS) e abbiamo osservato che, in queste condizioni, i topi sviluppano fibrosi epatica.

Per concludere, i dati mostrati in questa tesi dimostrano che SLC25A47 è un nuovo regolatore decisivo nel contesto del metabolismo epatico e pongono questo trasportatore al centro dell'omeostasi mitocondriale.

Parole chiave: Mitocondri; Trasportatore mitocondriale; SLC25; MSR; FGF21; Metabolismo epatico; Fibrosi

CHAPTER 1 Introduction

1.1 The liver: an integrative managing center

1.1.1 Hepatic roles in metabolic homeostasis

The liver is a central organ that performs critical functions for physiological homeostasis, including detoxification, digestion, endocrine functions, blood clotting, plasma protein synthesis and energy metabolism¹. It is a highly structured organ composed of anatomical units named liver lobules². The hepatic tissue is extremely heterogeneous in terms of cell-type composition, with hepatocytes being the most abundant cells, representing 70% of the total cell number in the liver. The remaining cell types include cholangiocytes (or biliary epithelial cells), endothelial cells (the interface between blood cells and hepatocytes in the sinusoid), Kupffer cells (the resident macrophages) and stellate cells (quiescent fibroblasts). Liver tissue is spatially structured, with hepatocytes located in different areas performing different metabolic functions. The blood flowing from portal veins and hepatic arteries, at the corner of the lobules, towards central veins, generates a gradient of oxygen, nutrients and hormones^{3,4} (Figure 1.1), that causes the liver lobules to show functional variance along the portal-central axis, a phenomenon called “liver zonation”⁵. For instance, some energetically demanding processes (such as gluconeogenesis or protein synthesis) are allocated to the portal layers (periportal), where oxygen is more abundant, whereas pericentral layers (closer to the central vein) are responsible for bile acid synthesis, glycolysis and xenobiotic metabolism (Figure 1.1).

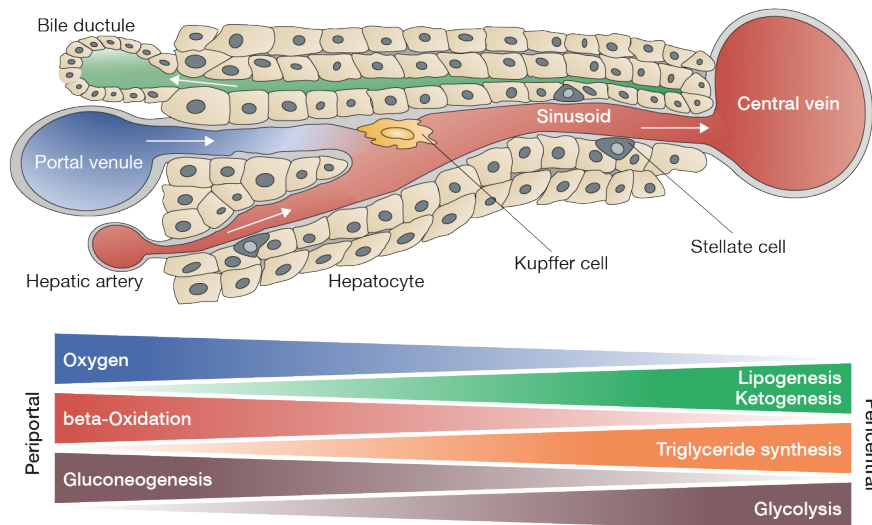


Figure 1.1. Structure of the hepatic lobule and metabolic zonation. The liver contains different zones that separate distinct metabolic functions. Bile ductules are localized in the periportal zone (left). Blood from portal vein travels through the liver sinusoids and reaches the central vein (right). Adapted from⁶.

The liver orchestrates whole-body carbohydrate, lipid, and protein metabolism by responding to external cues, storing nutrients and partitioning them to the rest of the body, thus playing a significant role in the intermediary metabolism by coordinating the energy demand of peripheral tissues⁷ (Figure 1.2).

In the context of carbohydrate metabolism, the liver is a prime target of hormone signaling, like insulin and glucagon, (Figure 1.2) and contributes to balancing glucose blood levels by regulating gluconeogenesis and glycogen synthesis in hepatocytes⁸. While in the fed state glucose enters hepatic cells stimulated by insulin and is used to synthesize glycogen, in the fasted state glycogen is hydrolyzed to generate glucose⁹. The latter process, called glycogenolysis, is the first route by which mobilization of glucose from glycogen helps to restore glycemic levels. However, during prolonged fasting, glycogen is depleted and hepatocytes, stimulated by glucagon, synthesize glucose *de novo* through gluconeogenesis using lactate, pyruvate, glycerol and amino acids as substrates. The rate of gluconeogenesis is determined by the availability of gluconeogenic substrates and the expression of gluconeogenic enzymes⁸. Additionally, hormones, like glucagon and catecholamines, positively regulate gluconeogenesis through cyclic adenosyl monophosphate (cAMP)-dependent protein kinase A (PKA) activation¹⁰. In physiological conditions, hepatic glucose metabolism is tightly controlled, and a dysregulation of this pathway is central to the pathogenesis of metabolic disorders, including type 2 diabetes (T2D)¹⁰.

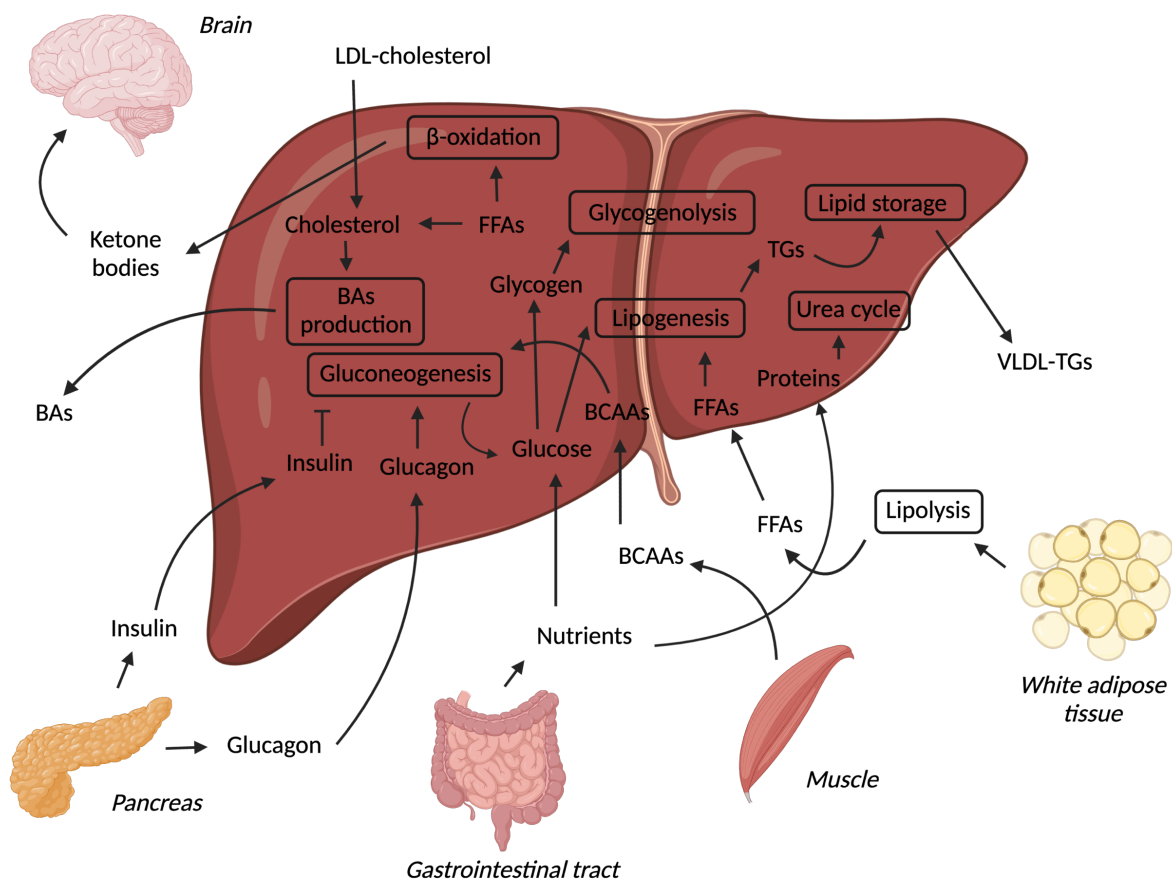


Figure1. 2. Role of liver in controlling the whole-body metabolic homeostasis. FFAs: free fatty acids. BAs: bile acids. TGs: triglycerides. BCAAs: branched-chain amino acids. LDL: low density lipoproteins. VLDL: very-low density lipoproteins. Created with BioRender.com.

In addition to carbohydrates, the liver is the main organ to synthesize fatty acids by *de novo* lipogenesis^{11,12} (Figure 1.3), which is the metabolic process that generates fatty acids (FAs) from excess carbohydrates in the fed state. The newly generated FAs, as well as dietary FAs and non-esterified FAs (NEFAs) derived from adipose tissue, can be re-esterified into TGs in the liver and stored as very-low-density lipoproteins (VLDL). VLDL-TGs can subsequently leave the liver and reach peripheral tissues.

Additionally, with muscle, the liver is a major site of β -oxidation (Figure 1.3), that provides energy for gluconeogenic processes in the fasted state. During fasting, rising levels of glucagon and epinephrine stimulate the hydrolysis of TGs from adipose tissues. As a consequence, TGs-derived free fatty acids (FFAs) are released in the blood stream and reach the liver where they can be metabolized. The β -oxidation pathway also generates ketone bodies, which are secreted in the blood to reach extrahepatic tissues⁸ (Figure 1.2).

Excessive lipid synthesis, defective VLDL assembly, and impaired FA oxidation are the main causes of TG accumulation in the liver. This condition is known as hepatic steatosis¹³ and it is also the principal hallmark of hepatic metabolic disorders, like non-alcoholic fatty liver disease (NAFLD)¹⁴.

Another critical, and unique, role of hepatocytes in coordinating lipid metabolism is the synthesis of bile acids (BAs). Indeed, BAs are products of cholesterol catabolism that are secreted into the bile and stored in the gallbladder together with other bile constituents, including cholesterol, phospholipids, glutathione and bilirubin¹⁵. Food intake is the main trigger of bile secretion in the intestinal tract, where BAs exert a detergent-like activity by forming micelles with dietary lipids and fat-soluble vitamins, to facilitate their intestinal absorption. BAs can then return to the liver via the portal vein and undergo several enterohepatic cycles a day¹⁶.

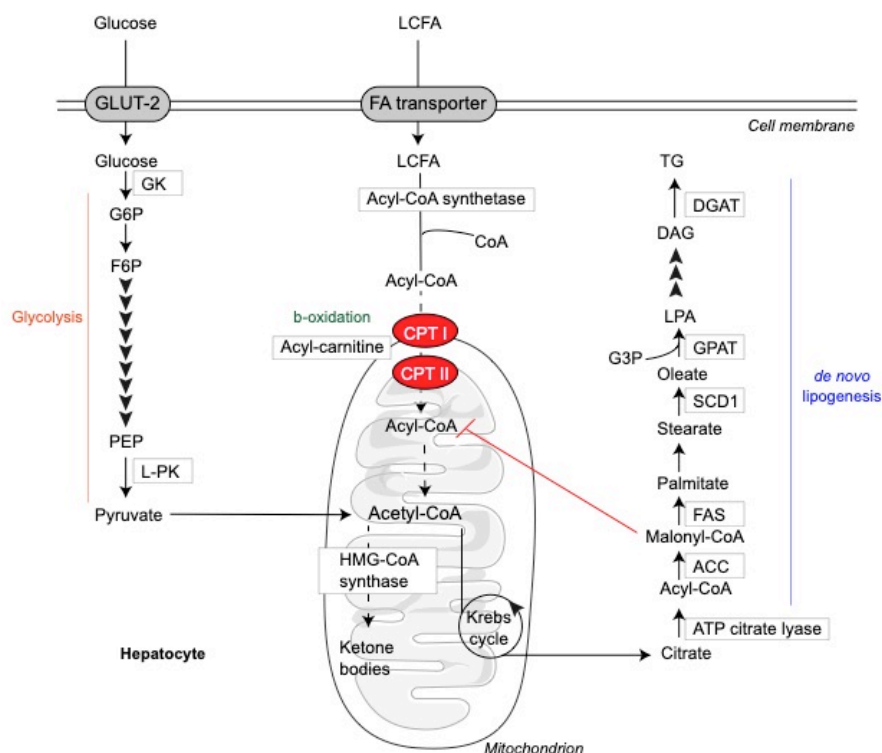


Figure 1.3. Lipid synthesis and lipid catabolism in liver. GLUT-2: glucose transporter 2. GK: glucose kinase. G6P: glucose-6-phosphate. F6P: fructose-6-phosphate. PEP: phosphoenolpyruvate. LCFA: long-chain fatty acids. CPT I/II: carnitine palmitoyltransferase I/II. HMG-CoA: β -hydroxyl β -methylglutaryl-CoA. ACC: Acetyl-CoA carboxylase. FAS: fatty acid synthase. SCD1: steryl-CoA desaturase 1. GPAT: glycerol-3-phosphate acyltransferase. DGAT: diacylglycerol O-Acyltransferase. Adapted from¹³.

Unlike carbohydrates and lipids, amino acids are not stored in the body. The liver plays a pivotal role in regulating amino acid metabolism for the entire organism as it is involved in ammonia detoxification. Indeed, excessive ammonia is toxic for the organs and requires to be properly disposed. Almost all ammonia produced by deamination is converted into urea in hepatocytes, through the urea cycle¹⁷, an essential pathway for ammonia and reactive nitrogenous molecule detoxification, which also allows the conversion of the carbon skeleton of specific amino acids to gluconeogenic substrates¹⁸ (Figure 1.2). The liver is the only organ to possess all the enzymes necessary for the urea cycle reactions. Particularly, the responsible proteins are restricted to hepatic mitochondria¹⁹ and defects in urea cycle enzymes or transporters lead to severe pathologies known as urea cycle disorders (UCDs)²⁰. Amino acid catabolism starts in the hepatocytes surrounding the portal veins, with the exception of branched-chained amino acids (BCCAs) that are initially catabolized in the skeletal muscle (Figure 1.2).

Besides its role in amino acid catabolism, the liver is responsible for ~90% of the circulating protein volume¹, as it secretes albumin, fibrinogen, lipoproteins, growth factors and most of the α and β globulins. Because of the essential role of the liver in controlling the synthesis of plasma proteins, any hepatic dysfunction results in the alteration of their levels, as exemplified by the fact that a decreased amount of plasma albumin is a typical hallmark of liver failure²¹.

1.1.2 Hepatic metabolic flexibility

The liver constantly adapts to external cues and rapidly modifies the oxidation of nutrients according to their availability. Hepatocytes in general, and hepatic mitochondria in particular, play a central role in regulating this process, defined as metabolic flexibility, and allow the organism to switch from fatty acid uptake and lipid oxidation during the fasted state to enhanced glucose oxidation during the fed state^{22,23}. Consequently, impaired hepatic mitochondrial activity characterizes metabolic inflexibility, the loss of adaptive capacity to nutritional transitions, frequently observed in obesity and T2D²². Most chronic hepatic diseases correlate with the accumulation of dysfunctional mitochondria responsible for several metabolic abnormalities^{24,25}. Depending on its nature and severity, mitochondrial dysfunction may induce lipid accumulation, apoptosis, and/or necrosis, causing hepatic cytolysis and inflammation^{26,27}. These occurrences can lead to different clinical pathological features, like fibrogenesis, lactic acidosis, hypoglycemia, elevated serum transaminases, higher conjugated bilirubinemia, and hyper-ammonemia²⁸.

Metabolic disorders, like obesity and insulin resistance, correlate with decreased mitochondrial bioenergetics, which can lead to pathological states such as NAFLD^{29,30}. Evidence suggests that oxidative metabolism of liver mitochondria undergoes an adaptive program in response to hepatic steatosis^{29–32}. This adaptation and remodeling play a major role in the progression to nonalcoholic steatohepatitis (NASH)²⁹. Importantly, mitochondrial dysfunction might cause a disruption of cellular homeostasis and eventually contribute to the development of chronic liver diseases that can culminate in hepatocellular carcinoma (HCC)³³. Thus, hepatic mitochondrial fitness is an essential hallmark of metabolic flexibility and a better understanding of liver mitochondrial metabolism may reveal new approaches to manage metabolic disorders.

1.2 Mitochondria as hubs of intermediary metabolism

1.2.1 Mitochondrial structure and genome

Mitochondria are eukaryotic bean-shaped organelles comprised of double and functionally distinct membranes (inner mitochondrial membrane-IMM and outer mitochondrial membrane-OMM), intermembrane space (IMS) and matrix compartments (Figure 1.4). According to the endosymbiotic theory³⁴, mitochondria derive from an *alpha-proteobacterium*, engulfed by an eukaryotic progenitor that survived endocytosis and became incorporated in the cytosol. Consequently, mitochondria still present their own genome (mitochondrial DNA, mtDNA), organized into nucleoids in the matrix. Interestingly, mtDNA has more sequence resemblance to its prokaryotic precursor than its eukaryotic host³⁵.

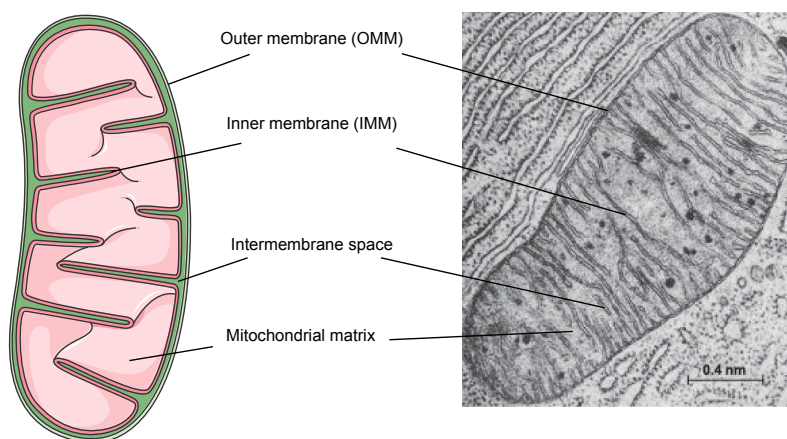


Figure 1.4. Structure of a mitochondrion. Schematic representation (left) and transmission electron microscopy image (right) of mitochondrial structure (from³⁶).

Indeed, the mitochondrial genome consists of a circular, double-stranded DNA molecule of 15,000-17,000 base pairs, encoding 37 genes. Twenty-four genes encode the translational machinery of the mtDNA itself (22 tRNAs and 2 rRNAs) and 13 genes represent different electron transport chain (ETC) complex subunits^{37,38}. Until 2019, mtDNA inheritance was thought to be exclusively maternal, with the paternal mtDNA being actively destroyed after fertilization by autophagy³⁹. However, maternal and paternal mtDNA traces have been recently found in individuals with heteroplasmy, a condition in which normal and mutant mtDNA molecules coexist in a single cell, opening the hypothesis for biparental inheritance of the mtDNA⁴⁰.

In mammals, the entire mitochondrial genome is transcribed as one long polycistronic transcript, which needs to be processed (i.e. chemically modified) before becoming individual RNA species⁴¹. The translation of the mitochondrially encoded proteins (mt-translation), then, occurs on a dedicated set of mitochondrial ribosomes, called mitoribosomes that are more similar to prokaryote than cytoplasmic ribosomes⁴². Mitoribosomes specifically synthesize some peptide chains of the IMM-bound respiratory chain proteins and are, therefore, associated with the IMM. For this reason, defects in mitochondrial transcription or translation and mt-DNA mutations lead to respiratory dysfunction and are the main cause of mitochondrial diseases in humans⁴³⁻⁴⁵. For example, mutations in the mitochondrial-specific tRNA-modifying enzyme (*TMRU*) causes reduced mitochondrial tRNA levels and is responsible for acute infantile liver failure⁴⁶. Moreover, recent studies show that mutations in mt-DNA are associated with hepatocellular dysfunction, such as biliary atresia, a condition resulting in severe bile blockage⁴⁷.

1.2.2 Mitochondrial metabolic function

Mitochondria are the hub of intermediary metabolism and are essential to metabolic homeostasis,

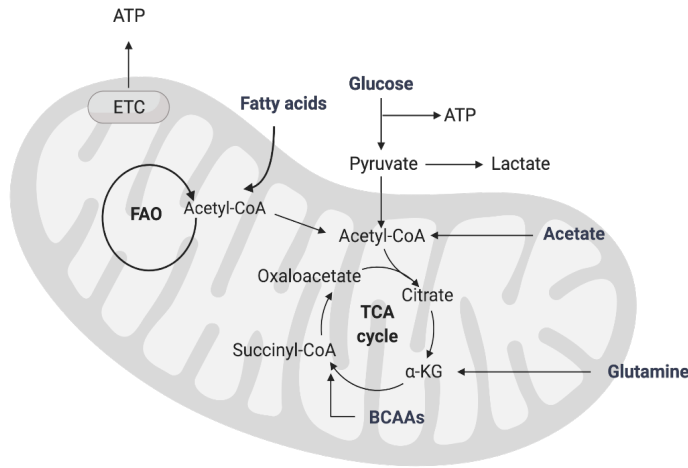


Figure 1.5 Mitochondria are the hub of intermediary metabolism. Scheme depicting the role of mitochondria in intermediary metabolism. TCA: tricarboxylic acid. FAO: fatty acid oxidation. BCAAs: branched chain amino acids. ATP: adenosine triphosphate. Created with BioRender.com.

as they are the site of catabolism of different metabolic fuels, including glucose, fatty acids, and proteins (Figure 1.5). These unique organelles are best known for harvesting the energy of nutrients into adenosine triphosphate (ATP) via oxidative phosphorylation (OXPHOS), which can be responsible for up to 90% of ATP molecules in the cell. The

process happens in the mitochondrial matrix, where the tricarboxylic acid cycle (TCA, Figure 1.5) enzymes generate nicotinamide adenine

dinucleotide (NADH) and flavin adenine dinucleotide (FADH_2), two electron carriers that, during the process of oxidation, donate electrons to the IMM-localized ETC. In the ETC, the electrons pass through a series of four protein complexes (I-IV, Figure 1.6). Three of these complexes (I, II, IV) act as redox-driven proton pumps and transfer protons to the IMS. The ETC comprises the two-electron carrier molecules, ubiquinone (known as coenzyme Q [CoQ] or ubiquinol when in the fully reduced state [CoQH_2]), and cytochrome c (cyt c), which carry electrons from one IMM-integrated complex to another. The proton gradient, commonly called proton motive force, generated by complex I, III, and IV drives the rotation of a fifth complex (complex V, also named ATP synthase, Figure 1.6), leading to phosphorylation of adenosine diphosphate (ADP) and generation of ATP. The entire OXPHOS process requires oxygen, which act as a terminal electron acceptor and is reduced to a water molecule by complex IV using the electrons derived from NADH and FADH_2 .

The TCA cycle is not the only pathway fueling the ETC with electrons. The mitochondrial fatty acid β -oxidation (FAO) is tightly linked to the OXPHOS, with FAO providing reducing equivalents to the OXPHOS complexes (Figure 1.6). In particular, the dehydrogenase steps of FAO produce FADH_2 and NADH molecules, whose electrons are transferred to ubiquinone (through electron transfer flavoprotein (ETF) CoQ oxidoreductase, ETF:QO) and OXPHOS complex I, respectively (Figure 1.6). Interestingly, many studies demonstrated that FAO proteins and OXPHOS complexes physically interact^{48,49} and primary FAO deficiencies show secondary defects in OXPHOS enzyme activity^{50,51}.

Because of the OXPHOS process, mitochondria account for about 85% of oxygen consumed by cells. Therefore, despite being the primary source of energy, mitochondria are also the main source of reactive oxygen species (ROS) production. ROS species, if not neutralized, are hazardous for the cells since their accumulation can damage DNA, proteins and lipids⁵². Despite the constant production of ROS in the mitochondria, the mitochondrial antioxidant defenses (specifically thioredoxin, glutaredoxin, glutathione, and manganese superoxide dismutase) prevent oxidative damage generated during regular aerobic metabolism⁵³.

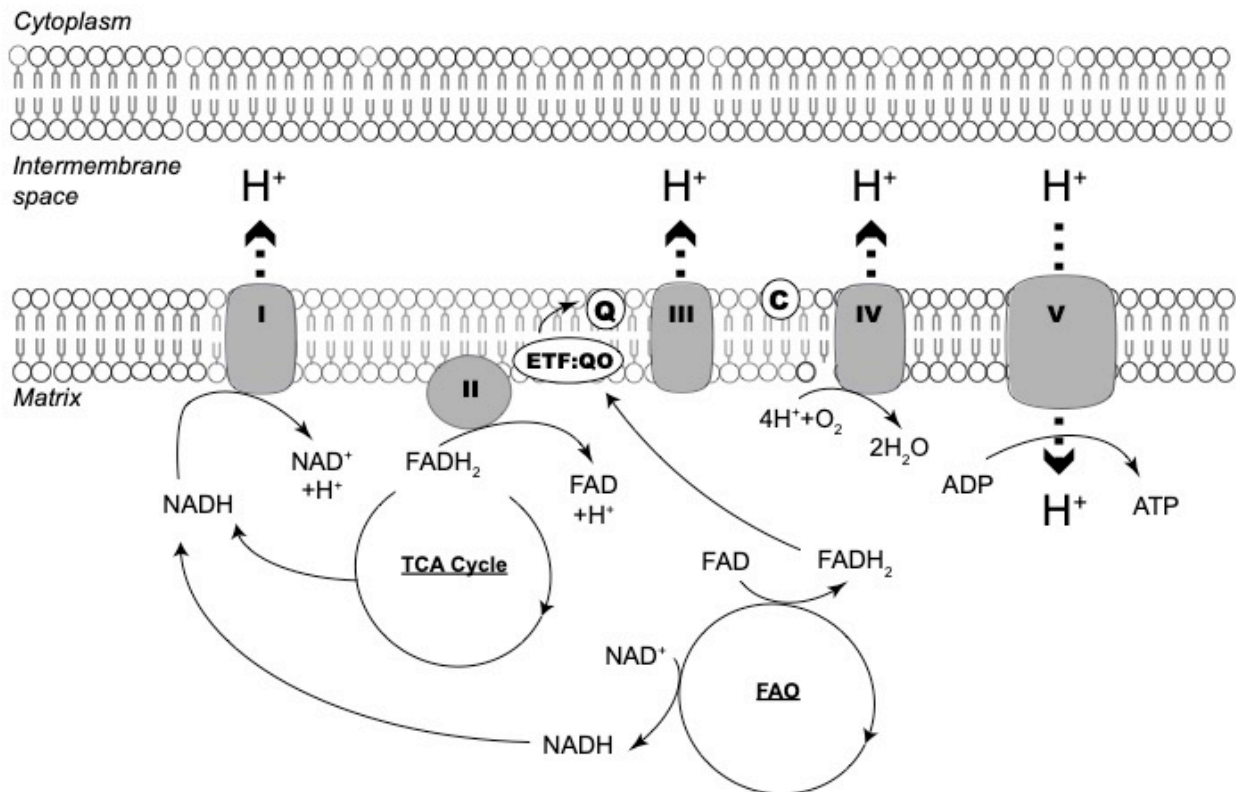


Figure 1.6. Scheme depicting oxidative phosphorylation (OXPHOS) in the mitochondria. The energy released by stepwise oxidation reactions between NADH (nicotinamide adenine dinucleotide), FADH₂ (flavin adenine dinucleotide) and ubiquinol (Q) pumps protons (H⁺) from the mitochondrial matrix to the intermembrane space. The energy potential of the proton gradient is used by ATP synthase (complex V) to phosphorylate adenosine diphosphate (ADP) to generate adenosine triphosphate (ATP). Both tricarboxylic acid (TCA) cycle and fatty acid β -oxidation (FAO) generate electron donors for the OXPHOS process. Complex II (II, known as succinate dehydrogenase) is the only TCA cycle enzyme to be an IMM-protein and part of the electron transport chain. ETF:QO: electron transfer flavoprotein coenzyme Q oxidoreductase. C: cytochrome C. I-IV: Complex I-IV.

1.2.3 Mitochondrial stress signaling

Mitochondria are highly dynamic organelles that communicate with the rest of the cell, and with the organism, by exchanging different molecules such as ions, metabolites, nucleotides, proteins and lipids⁵⁴. The correct crosstalk between nucleus and mitochondria is essential to coordinate transcription, translation, and import of mitochondrial proteins⁵⁴. Consequently, impairments in mitochondrial transport, OXPHOS alterations, loss of membrane potential, ATP depletion, and mitochondrial transcription and translation defects disrupt this communication equilibrium⁵⁵.

These challenges trigger a crosstalk between the mitochondria, the nucleus and the cytosol, activating transcriptional, translational and post-translational programs to restore mitochondrial homeostasis. One of the major adaptive pathways is the mitochondrial unfolded protein response (UPR^{mt}), a highly conserved mitonuclear communication network crucial to maintain mitochondrial function^{56,57}. UPR^{mt} has been extensively characterized in the nematode *Caenorhabditis elegans*, where the response starts after cleavage of unfolded proteins mediated by the mitochondrial protease

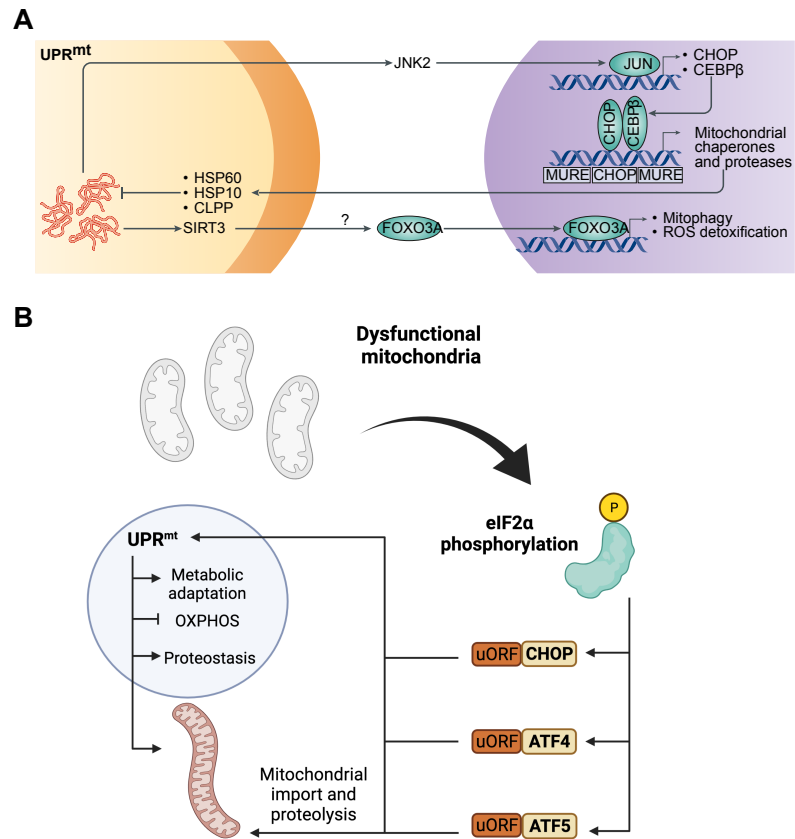


Figure 1.7. Mitonuclear communication in mammals. (A) In mammals, JUN activation by c-Jun N-terminal kinase 2 (JNK2) induces CEBP homologous protein (CHOP) and CCAAT/enhancer-binding protein-β (CEBPβ), which activate UPR^{mt} genes. Proteotoxic stress activates sirtuin 3 (SIRT3) that deacetylates forkhead box transcription factor FOXO3A. FOXO3A translocates into the nucleus to induce the expression of reactive oxygen species (ROS) detoxification and mitophagy genes. Adapted from⁵⁷. (B) Mitochondrial dysfunction stimulates the phosphorylation of eIF2α, which induces the transcription of CHOP, activating transcription factor 4 and 5 (ATF4 and ATF5). CHOP, ATF4 and ATF5 stimulate the transcription of genes that enable recovery from mitochondrial insults. Adapted from⁶⁰ and created with BioRender.com.

caseinolytic mitochondrial matrix peptidase proteolytic subunit (CLPP). The cleaved peptides, then, induce metabolic and transcriptional changes coordinated by the activating transcription factor associated with stress-1 (ATFS-1) and various chaperones⁵⁸.

In mammals, the UPR^{mt} is far more complicated than its nematode counterpart (Figure 1.7A). Transcription of UPR^{mt} genes (Figure 1.7A) is mediated by the activation of JUN by c-Jun N-terminal kinase 2 (JNK2), which induces CEBP homologous protein (CHOP) and CCAAT/enhancer-binding

protein- β (CEBP β). Proteotoxic stress can activate sirtuin 3 (SIRT3) that deacetylates forkhead box transcription factor FOXO3A. As a result, FOXO3A translocates into the nucleus to induce the expression of reactive oxygen species (ROS) detoxification and mitophagy genes (Figure 1.7A).

The mammalian UPR^{mt} is embedded in a broader program named integrated stress response (ISR)⁵⁹, a mechanism by which cells remodel gene expression to adapt to intrinsic and extrinsic stressors⁶⁰. The ISR is an adaptive translation program regulated by four distinct kinases (PKR-like ER kinase: PERK; general control nonderepressible 2: GCN2; protein kinase RNA-activated: PKR; heme regulator inhibitor of translation: HRI), that respond to different cues⁶¹. In more detail, PERK is mainly activated by endoplasmic reticulum (ER) and hypoxic stress, GCN2 responds to amino acid starvation, glucose deprivation and UV radiation, PKR is activated upon viral infection and HRI upon iron deprivation and proteasome inhibition^{60,61}. The responses of the different kinases converge on phosphorylation of the Serine 51 (S51) residue of the α -subunit of the eukaryotic translation initiation factor 2 (eIF2) complex⁶⁰. The result is a global reduction in protein synthesis paralleled by the induction of the translation of specific proteins. In fact, while global translation is attenuated upon activation of the ISR, some mRNAs with upstream open reading frames (uORFs) are selectively translated⁶². The transcription factors (TFs) activating transcription factor 4 (ATF4), 5 (ATF5) and CHOP harbor uORFs and are the main mediators of the ISR^{59,60} (Figure 1.7 B). Even though they have been studied explicitly in the context of ER stress responses, these TFs enable mitochondrial recovery upon mitochondrial dysfunction, such as OXPHOS impairments, alterations of mitochondrial dynamics and proteostasis^{63,64}.

In particular, both ATF4 and ATF5 play a preponderant role as major regulators of the stress response in the mitochondria^{63,65}.

ATF4 is a basic leucine zipper (bZIP) transcription factor, belonging to the ATF/CREB subfamily, that acts by forming homodimers or heterodimers with other TFs (such as CREBP β), repressing or transactivating different target genes. Increasing evidence has shown that a plethora of mitochondrial defects can induce ATF4, including OXPHOS inhibition, mitophagy defects and mitonuclear imbalance^{66–68}. Accordingly, in the liver, the glucose-lowering drug metformin can induce the ATF4 pathway via inhibition of complex I activity⁶⁹, and dysfunction in mitochondrial respiratory genes in both cardiac and skeletal muscles induce the ISR through ATF4^{70,71}.

Similar to ATF4, ATF5 belongs to the ATF/CREB subfamily of TFs, but little is known about its dimerization partners. ATF5 shares sequence homology with ATF4 and has similar downstream regulation effects⁷². Indeed, ATF5 takes part in the mitochondrial stress response, being the transcriptional regulator of many proteases and chaperones, such as *Hsp60*, *Hsp70* and *Lonp1*⁶⁴.

ATF5 is highly expressed in the liver but its role in this organ is still poorly characterized. Recently, ATF5 has been shown to be the first ISR responder in primary hepatocytes carrying impaired mitochondrial dynamics due to a deletion of the mitochondrial fission 1 protein (*Fis1*)⁷³.

While the ISR is beneficial for mitochondrial homeostasis, its chronic upregulation can contribute to the development of pathological conditions⁷¹.

Role of mitokines in the ISR

In the context of the ISR, ATF4 and CHOP have been widely described as transcriptional regulators of a class of circulating molecules known as mitokines^{74,75}. Indeed, these signaling proteins contribute to the mitochondrial stress response (MSR) by inducing metabolic responses in different tissues in a non-cell autonomous manner⁷⁶. For example, mitokines produced by several organs (like liver, muscle, white adipose tissue [WAT]) can mediate metabolic adaptation in distal tissues by inducing oxidative metabolism, lipolysis, and ketogenesis as a reaction to energy deficiencies caused by mitochondrial dysfunction. Fibroblast growth factor 21 (FGF21), growth differentiation factor 15 (GDF15) and adrenomedullin 2 (ADM2) are amongst the most studied mitokines known to be induced during mitochondrial stress in an ATF4 or CHOP-dependent manner^{77–79}. Ectopic expression and exogenous treatment with these mitokines have been described to ameliorate several metabolic diseases, including obesity, NAFLD, T2D, and cancer cachexia^{80–85}.

FGF21 is part of the FGF family, which includes 22 members involved in cell survival, growth, differentiation, and tumor formation⁸⁶. FGF21, together with FGF19 and FGF23, is structurally and functionally different from the other FGFs, as its interaction with FGF receptors depends on the presence of the beta-glucuronidases Klotho (beta-Klotho) coreceptors^{87,88}. In physiological conditions, FGF21 has pleiotropic effects when released by hepatocytes in response to nutritional cues, such as fasting, ketogenic diet (KD), and protein restriction^{89–91}. It has multiple roles in controlling lipid and glucose metabolism, food intake, insulin sensitivity, glucose clearance and beiging of the WAT⁹². The expression of FGF21 during fasting or feeding with ketogenic diets is dependent on peroxisome proliferator-activated receptor alpha (PPAR α), which regulates lipid oxidation, ketogenesis, and gluconeogenesis^{93,94}. Additionally, the liver signals to the brain through FGF21 in order to regulate glucose homeostasis, sugar preference and protein status^{95–99}. Importantly, FGF21 administration has been shown to benefit a cluster of obesity-related complications, including body weight reduction, improvement of insulin sensitivity, decrease in hepatic lipid accumulation, increase in uncoupling protein 1 (UCP1)-independent energy expenditure (EE)^{92,100,101}. However, FGF21 is not only a metabolic regulator but it is also considered a hepatic stress hormone. As mentioned above, FGF21 is part of the ISR pathway, induced by ATF4 binding on the two functional amino acid/carbohydrate response elements (AARE/CARE) in the *Fgf21* promoter^{78,102}. Methionine restriction (MR) can induce a robust hepatic secretion of FGF21 in an ATF4-dependent way, leading to a dramatic decrease of body weight and adiposity, paralleled by improved glucose and lipid homeostasis¹⁰³. Similarly, KD feeding is associated with the induction of *Fgf21* and the correction of metabolic dysfunction in obese wild type mice, while in FGF21-deficient mice KD leads to hepatic steatosis and prevents weight loss¹⁰⁴.

In terms of energy metabolism, FGF21 has some overlapping roles with GDF15, a peptide hormone member of the transforming growth factor beta (TGF β) family. Physiologically, GDF15 is expressed at low levels in multiple tissues, but its levels increase during malignant transformations, aging, metabolic diseases and inflammation¹⁰⁵. GDF15 signals to the brain via the glial cell-derived neurotrophic factor (GDNF) family receptor alpha-like (GFRAL)^{106,107}, where it exerts an anorexigenic effect; indeed, GDF15 administration induces weight loss through appetite suppression¹⁰⁸. Additionally, GDF15 has been reported to alleviate hepatic steatosis and inflammation, and to improve insulin sensitivity, lipolysis of adipose tissue and muscle atrophy via different mechanisms^{80,109–112}. On the contrary, ablation of *Gdf15* in murine models fed methionine-choline-deficient diet (MCD) aggravates the NASH phenotype, leading to increased hepatic steatosis and inflammation¹¹³.

Similarly to FGF21, GDF15 is considered a stress factor and, accordingly, its levels increase sequentially with the progression of the hepatic metabolic disease, being the highest in advanced fibrosis, followed by NASH and NAFLD¹¹⁴. This is due to the activation of the ISR, which leads to GDF15 upregulation in a CHOP-dependent manner¹¹⁴. In particular, GDF15 has a role in mediating ISR responses in mitochondrial DNA/ribosome pathologies, during OXPHOS inhibition and ER stress^{113,115,116}.

Finally, ADM2 is an endogenous peptide belonging to the calcitonin gene-related peptide family and its expression is induced upon mitochondrial stress caused by OXPHOS inhibition through the ATF4 pathway⁷⁷. ADM2 overexpression *in vivo* ameliorates obesity and insulin resistance by increasing thermogenesis in brown adipose tissue (BAT) of high-fat diet fed mice^{117,118}.

Lastly, mitochondrial-derived peptides, like Humanin, small humanin-like peptide (SHLP) 1-6 and mitochondrial ORF of the 12S rRNA type-c (MOTS-c), are synthesized by the mitochondrial genome as signaling molecules¹¹⁹. Their role in the context of mitochondrial stress is still understudied but recent evidence shows that these peptides promote metabolic homeostasis and ameliorate a variety of mitochondrial disorders^{120–123}.

1.3 Mitochondrial membrane transporters

The stress response pathways ensure the maintenance of mitochondrial homeostasis. Quality control mechanisms, as the UPR^{mt} mentioned above, are activated by a plethora of stressors, including the loss of proteostasis due to defective translocation of mitochondrial proteins through mitochondrial carriers. In this frame, the mitochondrial stress responses establish the proper communication network among different cellular compartments, such as nucleus, cytosol, and mitochondria.

Compartmentalization plays a crucial role in metabolic regulation¹²⁴, allowing spatial separation of opposing anabolic and catabolic pathways in distinct organelles. The functionality of compartmentalization relies on the expression of specific transporters that fine-tune the channeling

of metabolites across subcellular compartments¹²⁵. Together with enzymes, such carriers define the metabolic identity of a cell and dictate its metabolism.

In the mitochondrial compartment, the OMM has a 1:1 protein-to-phospholipid ratio similar to that of the plasma membrane¹²⁶. Porins (voltage-dependent anion channels) are integrated into the OMM, allowing the membrane to be permeable to small molecules (solutes up to 5kDa). Larger proteins need to carry an N-terminus signaling sequence, which is recognized by the translocase of the outer membrane (TOM), in order to enter the mitochondria¹²⁷. In contrast, the IMM – similar to the bacterial membrane- has a very high protein-to-phospholipid (3:1) ratio, comprising about 20% of the total protein content in a mitochondrion and is characterized by a distinct lipid composition that varies amongst cell types^{126,128}. Additionally, the IMM is rich in an unusual phospholipid called cardiolipin (25.4%), which is not found in the OMM¹²⁶. Cardiolipin can interact with mitochondrial respiratory complexes and carrier proteins, affecting mitochondrial function¹²⁹. These features make the IMM selectively permeable to maintain efficient oxidative phosphorylation and membrane potential¹³⁰. Therefore, the IMM requires the presence of a large number of carriers and channels that control the entry and exit of solutes, linking cytosolic and mitochondrial metabolism. Indeed, all major groups of nutrients pass through the mitochondria as part of intermediary metabolism, including degradation products of lipids, carbohydrates, vitamins, nucleotides and inorganic ions. Many mitochondrial transporter families exist in the mitochondria: solute carrier (SLC) 54 (SLC54, also known as mitochondrial pyruvate carrier family)¹³¹, the mitochondrial ABC transporters¹³², the sideroflexins (SLC56)¹³³ and the SLC25¹³⁴.

1.3.1 SLC25 family

The SLC25 family is responsible for most of the transport occurring in the mitochondria. SLC25 transporters are small transmembrane proteins with a molecular mass of about 30-34kDa and display structural features that make them different from any other known transporter family¹³⁵. All SLC25 members have a common 3-fold repeated signature motif: three tandemly repeated homologous domains of about 100 amino acids in length with two hydrophobic transmembrane α -helices connected by a long hydrophilic matrix loop (Figure 1.9). Both N- and C-termini are located in the intermembrane space¹³⁵. Contrary to most nuclear-encoded mitochondrial proteins, the mature form of the protein bears the mitochondrial-targeting sequence¹³⁵.

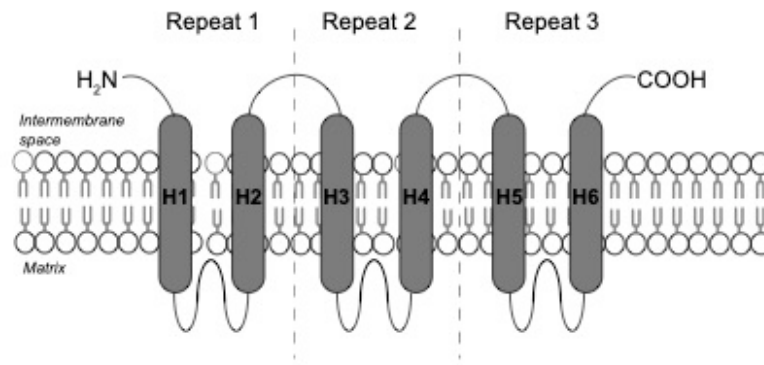


Figure 1.9. Structural model of signature motif in SLC25 family of mitochondrial transporters. H1-6 represent the three-fold tandemly repeated domains of two transmembrane α -helices. Each α -helix in the repeat is connected by a long matrix loop. Adapted from¹³⁸.

This family comprises 53 nuclear-encoded proteins (Figure 1.10) that are mostly localized in the IMM, with few exceptions in peroxisomes¹³⁶ or OMM¹³⁷. SLC25 members can transport a variety of anions, nucleotides and metabolites, bridging biochemical processes occurring outside and inside the mitochondria¹³⁴. Due to the plethora of transported molecules, SLC25 proteins are involved and control many metabolic processes, such as oxidative phosphorylation, TCA-mediated acetyl-CoA oxidation, FAO, amino acid degradation, gluconeogenesis, and urea synthesis from amino acids (urea cycle)¹³⁸ (Figure 1.11).

According to their solute specificity, SLC25 have been divided into subfamilies, each one characterized by distinctive structural features¹³⁹. The majority of SLC25 members catalyzes an

antiport (exchange of solutes), but few can catalyze uniport (unidirectional transport) of molecules.

Many solutes transported by SLC25 carriers have been already characterized (Figure 1.11). For example, uncoupling protein-1 (UCP1 or SLC25A7) is the H^+ ion carrier¹⁴⁰ and ADP-ATP carrier protein 1 (AAC1 or SLC25A4) is a very well-studied ATP/ADP transporter¹⁴¹. Additionally, mitochondrial carriers can be promiscuous and transport more than one solute with different binding efficiencies¹²⁵. For instance, SLC25A1 can mediate the exchange of citrate, but also malate, isocitrate, aconitate and phosphoenolpyruvate (PEP)¹⁴².

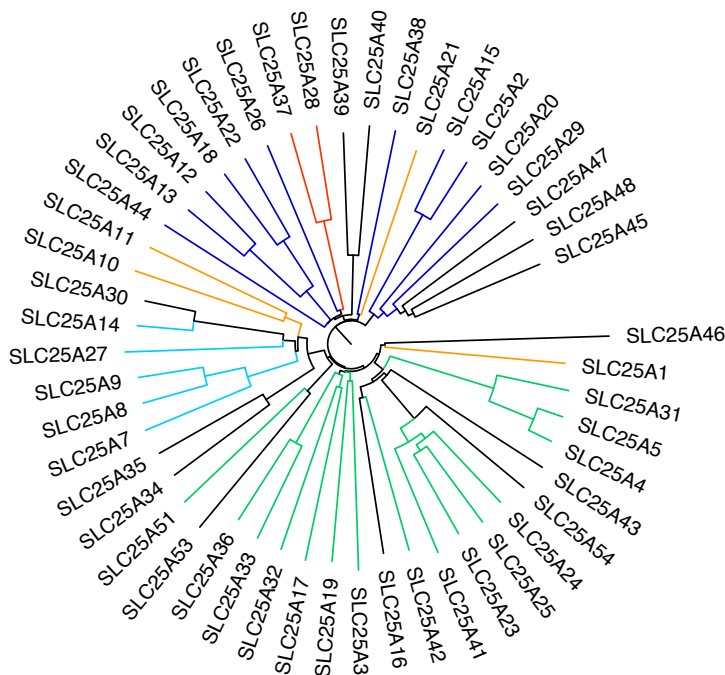


Figure 1.10. Solute carrier 25 family in mammals. Branch colors represent the functional annotation. Blue: amino acid carriers. Red: iron transporters. Light blue: uncoupling proteins (UCPs). Orange: carboxylate carriers. Green: nucleotide carriers. Black: unknown.

Similarly, the oxoglutarate carrier SLC25A11 is involved in the transport of oxoglutarate in exchange of dicarboxylate (malate) and is an important component of the malate-aspartate shuttle¹⁴³; however, it also contributes to the mitochondrial uptake of glutathione (GSH)¹⁴⁴. Despite the fact that some SLC25 members have been extensively studied, several remain orphan transporters and their function is still uncharacterized¹³⁸. Nonetheless, mutations and defects in mitochondrial carriers have been associated with various metabolic diseases¹⁴⁵. To date, mutations in 18 different SLC25 carriers have been reported to cause pathologies in humans¹⁴⁵. These mutations lead to accumulation of given solute(s), causing dysfunction in mitochondrial and cellular metabolism. The symptomatology is very variable and depends on the nature of the metabolite, its relevance in specific tissues, the tissue distribution of the dysfunctional carrier, and the presence in the same tissue of other transporters that can compensate the function. For example, mutations in the liver-specific aspartate/glutamate carrier (AGC2 or SLC25A13) causes neonatal onset of type-II citrullinemia and fatty liver, due to a dysfunction of the urea cycle^{146,147}.

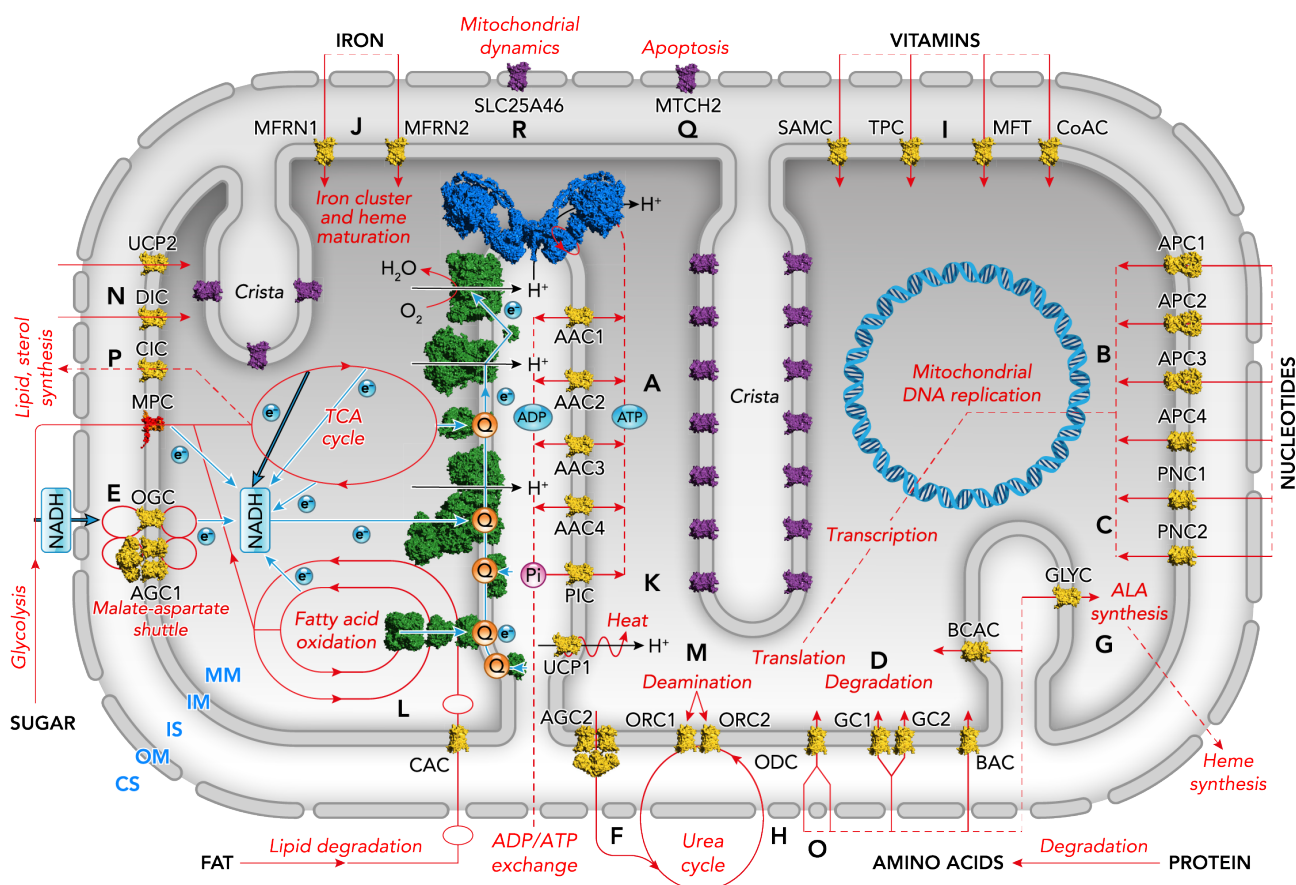


Figure 1.11. Role of solute carrier 25 family in metabolism. Schematic representation of the human SLC25 family members, involved in mitochondrial function and cellular metabolism. In green: OXPHOS complexes. In blue: ATP synthase. In red: MPC: mitochondrial pyruvate carrier. Uncharacterized and characterized carriers are shown in yellow and purple, respectively. AAC1-4: ADP/ATP carriers. AGC1-2: aspartate/glutamate carriers. GC1-2: glutamate carriers. GLYC: glycine carrier. MFRN11-2: mitoferrins. ODC: oxoadipate carrier. CIC: citrate carrier. APC1-4: ATP-Mg/Pi carriers. BAC: basic amino acid carrier. CAC: carnitine/acylcarnitine translocase. DIC: dicarboxylate transporter. OGC: oxoglutarate carrier. ORC1-2: ornithine transporters. PIC: phosphate carrier. SAMC: S-adenosylmethionine carrier. TPC: thiamine pyrophosphate carrier. UCP1-2: uncoupling proteins. CS: cytosol. OM: outer mitochondrial membrane. IM: inner mitochondrial membrane. MM: mitochondrial matrix. Q: ubiquinone. Pi: phosphate. ALA: aminolevulinic acid. Scheme taken from¹⁵¹.

By regulating the transport of small molecules across membranes, solute carriers in general play a pivotal role in physiology and act as gatekeepers of intermediary metabolism. Some SLC25 transporters have gained relevance in the context of drug discovery, being considered as promising targets for the treatment of cancer or metabolic disorders¹²⁵. For example, SLC25 members (such as SLC25A1, SLC25A8 and SLC25A33) were found to be upregulated in tumors, as consequence of the metabolic rewiring happening during carcinogenesis^{148–151}. However, despite their importance, many SLC25 transporters are still understudied and their function is poorly understood¹⁵². Given the potential biomedical relevance of these transporters and their fundamental role in mitochondrial and cellular metabolism, there is an urgent need to study orphan SLC25 members and characterize their pathophysiological role.

1.4.1 SLC25A47: an orphan mitochondrial carrier

SLC25A47 is a member of the SLC25 family whose gene was first cloned and identified in 2004 by sequencing specific clones downregulated in a patient with HCC, hence being named hepatocellular carcinoma downregulated mitochondrial carrier protein (HDMCP)¹⁵³. In this context, the lower expression of *Slc25a47* was proposed to help tumor resistance by counteracting apoptosis¹⁵³. However, despite this finding, the link between SLC25A47 and HCC has never been investigated. Nevertheless, these initial observations have underscored this carrier as a hallmark of liver identity. More recently, SLC25A47 has been reported to act as an uncoupler¹⁵⁴, and proposed to function as the hepatic-specific uncoupling protein (UCP). Indeed, the mitochondrial membrane potential of HEK-293T cells was disrupted upon overexpression of *Slc25a47*, suggesting possible roles of SLC25A47 in mediating uncoupling¹⁵⁴. However, these studies failed to demonstrate a direct link between SLC25A47 and its putative UCP activity, as *Slc25a47*-overexpressing mitochondria were insensitive to the classical UCP inhibitor guanoside diphosphate (GDP)¹⁵⁴. Moreover, SLC25A47 was furthermore proposed to play a role in the onset of hepatic steatosis^{154,155} and to be induced during NASH progression. However, these results were contradictory and incomplete. Despite these few available reports, SLC25A47 is largely understudied, with its structure, function or solute specificity still uncharacterized. Given the relevance of this hepatic-specific carrier and its possible implications in the development of liver diseases, SLC25A47 represents an interesting and novel research target.

Based on this important knowledge gap, my project aimed to provide a full characterization of this orphan SLC25 carrier. In particular, we extensively investigated the biological role of SLC25A47 and its involvement in liver physiology and metabolism, as well as liver disease.

CHAPTER 2 SLC25A47 is a novel determinant of hepatic mitochondrial function

Partially adapted from

The Slc25a47 locus is a novel determinant of hepatic mitochondrial function implicated in liver fibrosis. Nadia Bresciani[#], Hadrien Demagny[#], Vera Lemos, Francesca Pontanari^{\$}, Xiaoxu Li^{\$}, Yu Sun, Hao Li, Alessia Perino, Johan Auwerx, and Kristina Schoonjans. Journal of Hepatology 2022*

[#]Equal contribution

^{\$}Equal contribution

***Author contributions:** K.S. conceived, designed, and supervised the project. N.B., H.D., V.L., F.P. and A.P. performed animal experiments. N.B. performed *in vitro* experiments. X.L. analyzed the RNA-seq data. H.L. analyzed the scRNA-seq data. Y.S. performed ChIP experiments. J.A. provided expertise and funding. N.B., H.D., and K.S. wrote the manuscript.

2.1 *Slc25a47* is a hepatocyte-specific mitochondrial carrier

Despite their roles as gatekeepers of metabolic fluxes, mitochondrial carriers have been surprisingly understudied¹²⁵. To better characterize this family of transporters, we analyzed published RNA sequencing (RNA-seq) data obtained from three C57BL/6J males and evaluated the tissue distribution of all SLC25 family members across twelve metabolic organs (ENA: ERP104395) (Figure 2.1).

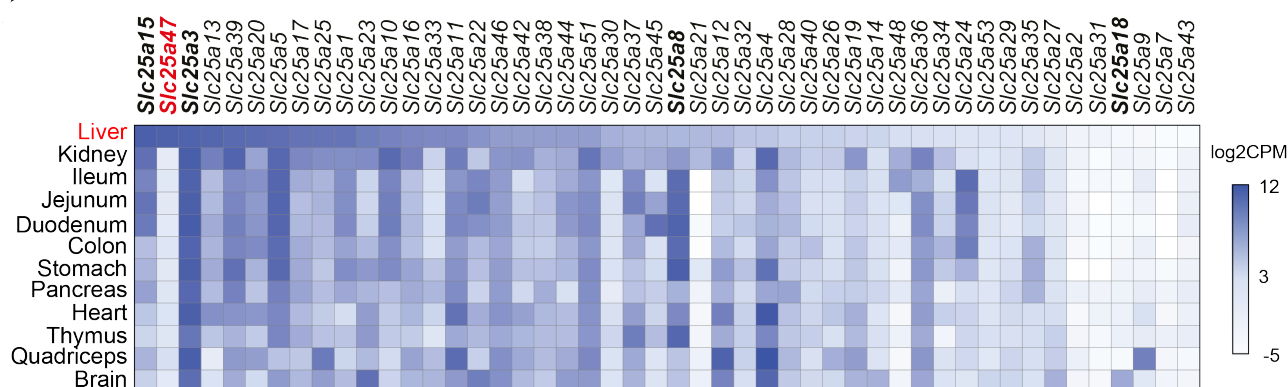


Figure 2.1. Expression and tissue distribution of the SLC25 carriers. Heatmap representing mRNA levels (log2 counts per million, CPM) of murine SLC25 family members in different tissues. Average values of three 7-8-week-old male mice (C57BL/6J) (ENA accession number: ERP104395). SLC25 members are ranked (left to right) according to their relative abundance in the liver.

This analysis revealed that members of the *Slc25* family vary greatly in their pattern of expression with some members widely expressed across tissues such as the phosphate carrier, *Slc25a3* (Figure 2.1), while others displayed a highly restricted pattern of expression, such as *Slc25a18*, a glutamate transporter solely expressed in the brain¹⁵⁶, or *Slc25a8*, which appeared to be particularly enriched in the various parts of the intestinal tract (Figure 2.1). Only one carrier, *Slc25a47*, was strictly confined to the liver, where it was as highly expressed as some major mitochondrial carriers such as the ornithine transporter *Slc25a15* (Figure 2.1). The liver-specific expression of *Slc25a47* was further confirmed by RT-qPCR and immunoblotting on different mouse tissues, including liver, epididymal WAT (eWAT), kidney, quadriceps, spleen, pancreas, and muscle (Figure 2.2).

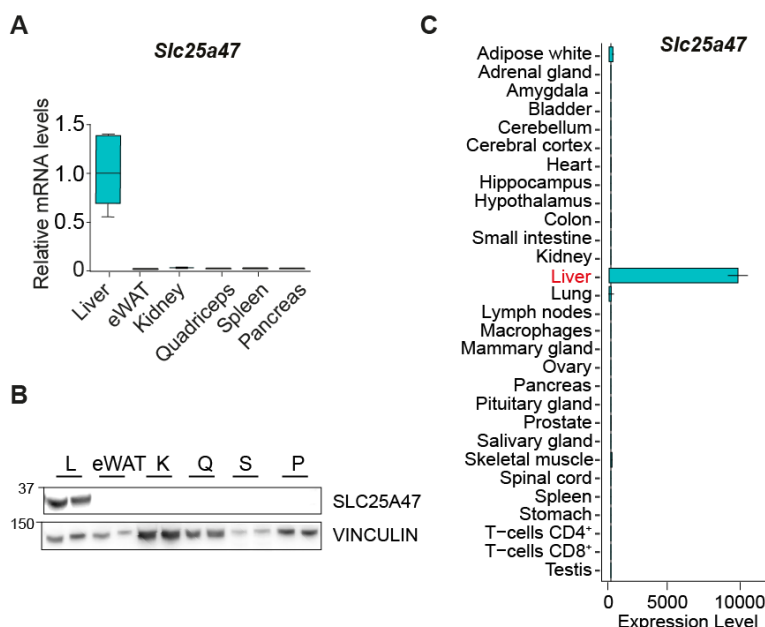


Figure 2.2. *Slc25a47* expression is hepatic-specific. (A, B) *Slc25a47* gene expression (A, n=3) and protein levels (B, n=2) in different tissues from 14-week-old C57BL/6 mice (L: liver, eWAT; epididymal white adipose tissue, K: kidney, Q: quadriceps, S: spleen, P: pancreas). VINCULIN was used as a loading control. (C) Mus musculus tissue expression profile of *Slc25a47* from BioGPS portal (GSE10246, from 8-10-week-old male and female C57BL/6 mice, n=6).

spleen and pancreas (Figure 2.2A, B). Moreover, we interrogated over 29 murine tissues available on published datasets (Figure 2.2C) and corroborated the restricted hepatic expression of SLC25A47. To gain further insight into the expression of this carrier at the cellular level, we analyzed published single-cell RNA-seq (scRNA-seq) data obtained from C57BL/6 mice. These analyses revealed that *Slc25a47* is uniquely expressed in hepatocytes (Figure 2.3A). Interestingly, the highest expression of *Slc25a47* was observed in periportal hepatocytes (Figure 2.3B), as confirmed by *in situ* hybridization (RNAscope) in livers of C57BL/6J mice (Figure 2.3C). At the sub-cellular level, when we overexpressed Flag-tagged *Slc25a47* in cells we observed SLC25A47-FLAG to co-localize with the inner mitochondrial membrane protein, Cytochrome c oxidase subunit 4 (COXIV, Figure 2.3D), underscoring the putative mitochondrial localization of SLC25A47.

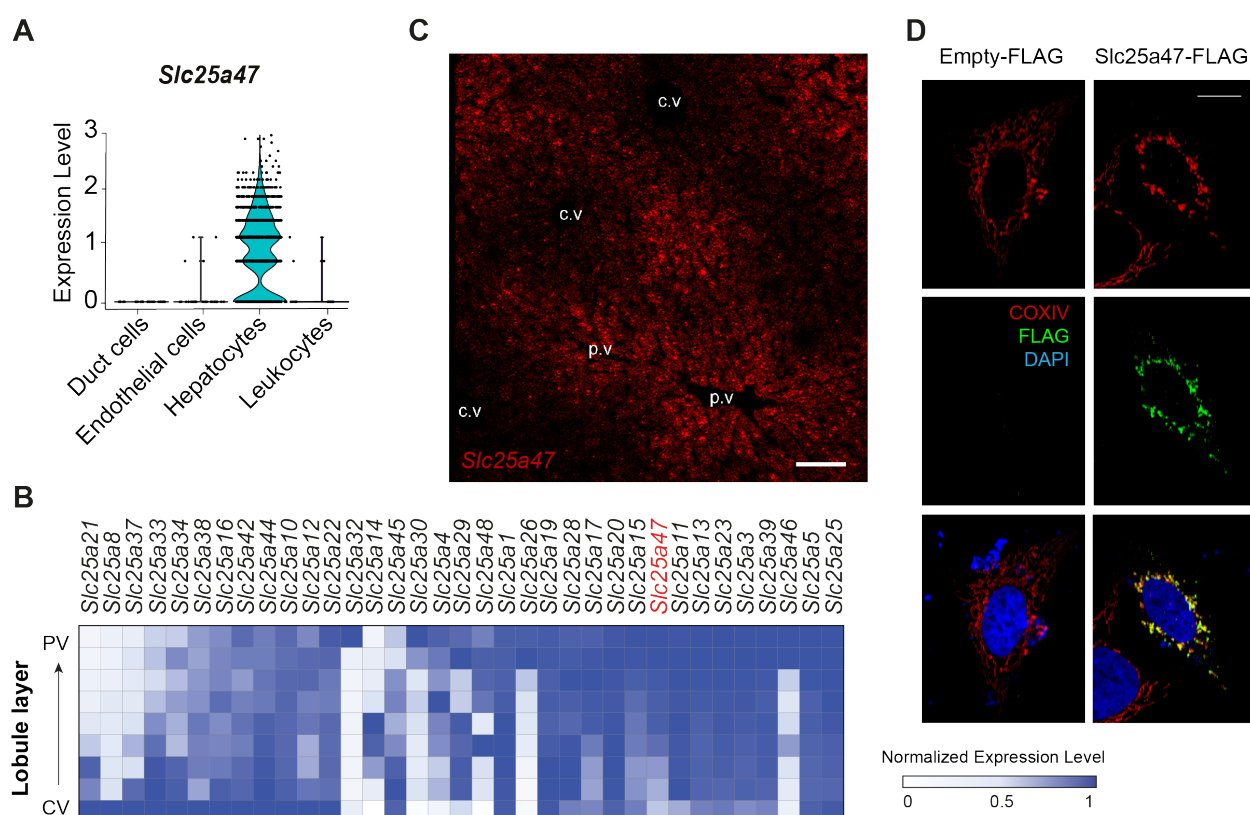


Figure 2.3. SLC25A47 is a hepatocyte-specific mitochondrial carrier. (A) Single-cell RNA sequencing (scRNA-seq) data of murine liver cell populations (from 3 females and 4 males C57BL/6 mice, 10-15-week-old) from Tabula Muris (GEO #109774, microfluidic droplet counting), showing *Slc25a47* as uniquely expressed in hepatocytes. (B) Heatmap representing the mRNA levels of murine SLC25 family members across the different hepatic layers. Data was obtained from GSE84498 (CV: central vein, PV: portal vein). (C) RNAscope image depicting *Slc25a47* mRNA presence and zonation on a C57BL/6J mouse liver section (c.v: central vein, p.v: portal vein). Scale bar: 100 μ m. (D) FLAG (green) and COXIV (red) immunofluorescence staining of HeLa cells overexpressing Empty-FLAG or FLAG-tagged SLC25A47. DAPI (blue) was used to stain nuclei. Scale bar: 50 μ m.

To better understand the function of SLC25A47, the laboratory in collaboration with Nuria Cirauqui (former laboratory member of Prof. Matteo dal Peraro, EPFL), previously performed protein sequence alignment between SLC25A47 and its closest homologs, including the carnitine/acyl carnitine translocase SLC25A20 and the amino acid carriers SLC25A15 (ornithine transporter 1, ORNT1), SLC25A2 (ornithine transporter 2, ORNT2) and SLC25A29 (ornithine and basic amino acid

carrier) (Figure 2.4A). The analysis revealed a low sequence similarity (about 30%) between the sequences, indicating that SLC25 family is more similar in structure rather than sequence. We then obtained SLC25A47 structure by homology modeling with the first structurally characterized SLC25, the ADP/ATP carrier¹⁵⁷ (SLC25A4, Figure 2.4B, C). The model showed a positively charged core that putatively allows the transport of negatively charged solutes (Figure 2.4B). Moreover, one portion of the protein sequence of SLC25A47 did not align with the other transporters (Figure 2.4B-D), highlighting a unique feature of SLC25A47. This region of the protein consists of a 30 amino acid-long stretch, defining a loop protruding in the mitochondrial matrix (Fig. 2.4D). Preliminary *in silico* analysis showed a known consensus sequence (R-R-X-S)¹⁵⁸ for PKA phosphorylation (Serine 137, Figure 2.4D) within the unknown loop of this carrier, suggesting that, if verified, PKA-mediated phosphorylation can possibly control the opening/closing of the channel.

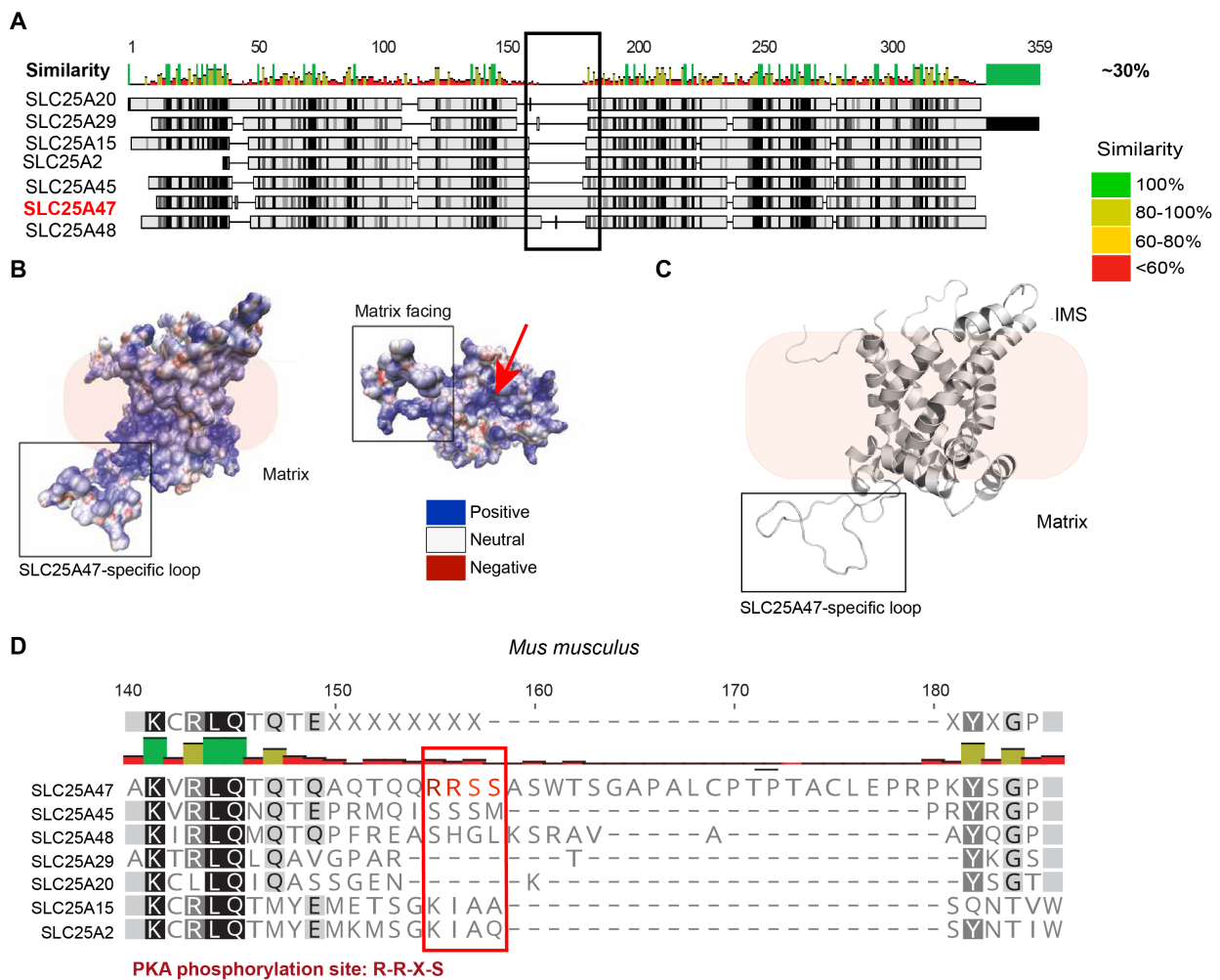


Figure 2.4. SLC25A47 structure. (A) Protein sequence alignment between SLC25A47 and its closest homologs. (B-C) 3-D (B) and 2-D (C) structure of SLC25A47 obtained by homology modeling to SLC25A4, depicting the SLC25A47-specific loop (black rectangle). The red arrow indicates the interior of the channel observed from the mitochondrial matrix. (D) Protein sequence alignment between the loop region of SLC25A47 and its closest homologs. The red rectangle shows the protein kinase A (PKA) consensus sequence only in SLC25A47.

Subsequently, in order to investigate the role of SLC25A47 in hepatocytes, we performed gene module association determination (G-MAD) analysis using mouse liver data and gene/pathways

annotations¹⁵⁹. This analysis revealed positive correlations between *Slc25a47* and mitochondrial metabolic functions, such as mitochondrial protein complexes, TCA cycle, ETC, IMM, peroxisome proliferator-activated receptor (PPAR) signaling, lipid catabolism, and fatty acid oxidation (Figure 2.5). Conversely, *Slc25a47* negatively correlated with cell cycle and cholesterol biosynthesis (Figure 2.5).

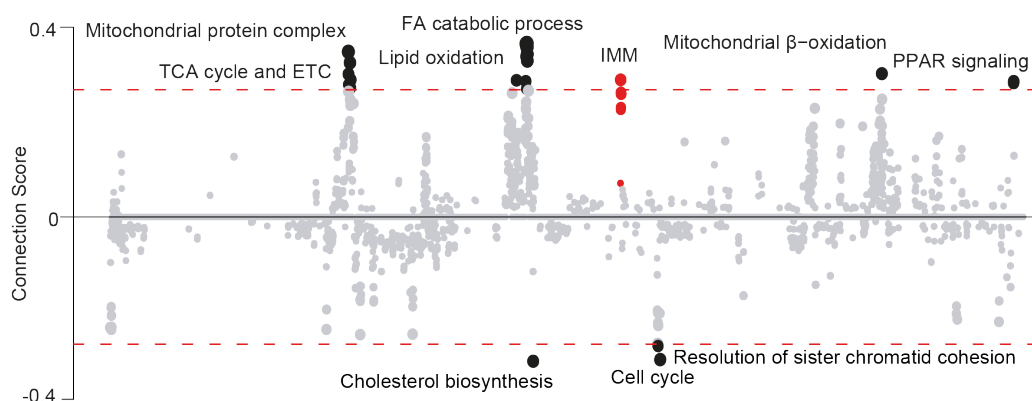


Figure 2.5. *Slc25a47* correlates with mitochondrial pathways. Gene module association determination (GMAD) analysis of *Slc25a47* in mouse liver datasets displaying both positive and negative connection scores. The threshold of significant gene-module association (0.26) is indicated by the red dashed lines. Known modules connected to *Slc25a47* from gene associations are shown with red dots, and other modules with scores over the threshold are shown as black dots. FA: fatty acid; TCA: tricarboxylic acid; ETC: electron transport chain; IMM: inner mitochondrial membrane; PPAR: peroxisome proliferator-activated receptor.

Two earlier reports proposed that SLC25A47 can act as an uncoupler^{153,160}. To further establish this point, we used a Crispr/Cas9 system (Crispr/dCas9) to boost the endogenous expression of *Slc25a47* in AML12 cells (Figure 2.6A). A moderate, but significant, increase in respiration was found upon induction of *Slc25a47* transcript levels (Figure 2.6B). In contrast to previous reports, however, overexpression of *Slc25a47* stimulated coupled (ATP-linked, Figure 2.6C), but not uncoupled respiration (Figure 2.6C), and increased ATP levels (Figure 2.6D), suggesting that, in this experimental setup, SLC25A47 did not act as an uncoupler.

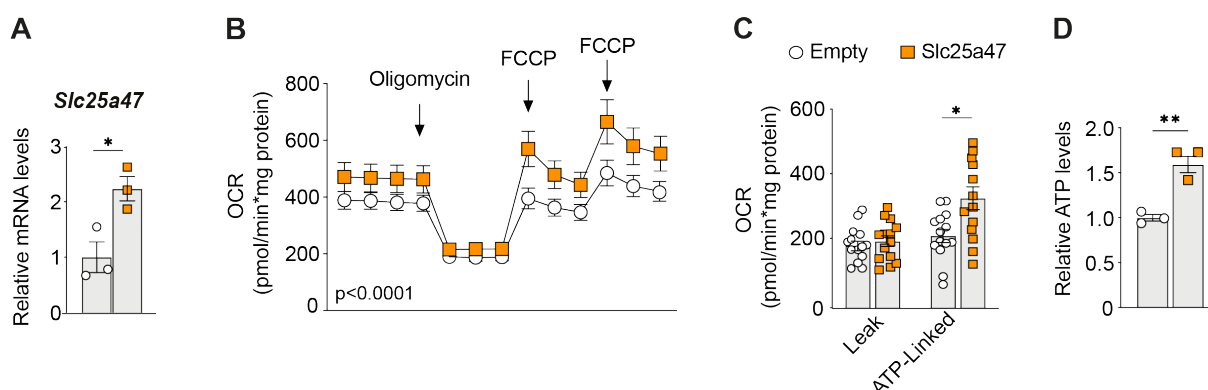


Figure 2.6. *In vitro* Crispr-activation of *Slc25a47*. (A) *Slc25a47* mRNA levels in Empty or *Slc25a47* Crispr/dCas9 AML12 cells (n=3). Data are relative to mRNA levels from Empty cells. (B) Oxygen consumption rate (OCR) measured in Empty or *Slc25a47* Crispr/dCas9 AML12 cells (n=15). FCCP: Carbonyl cyanide-p-trifluoromethoxyphenylhydrazone. (C) Proton leak (calculated by subtracting oligomycin to basal respiration) and ATP-linked respiration (obtained after oligomycin injection) in Empty or *Slc25a47* Crispr/dCas9 AML12 cells measured using Seahorse instrument (n=15). (D) Relative ATP levels measured in Empty or *Slc25a47* Crispr/dCas9 AML12 cells (n=3). Data are relative to ATP levels from Empty cells. Error bars represent mean

± S.E.M. * $p < 0.05$, ** $p < 0.01$ relative to Empty cells, as determined by unpaired Student's t-test (A, C, D) or two-way ANOVA and Bonferroni *post-hoc* correction (B).

Collectively, our data reveal that SLC25A47 is an inner mitochondrial membrane transporter highly and exclusively expressed in hepatocytes, playing a putative critical role in hepatocytes, yet different from uncoupling.

2.2 *Slc25a47*-deficient mice display hepatic metabolic dysregulation

To better understand the role of SLC25A47 in hepatic metabolism, we crossed C57BL/6 *Slc25a47*-floxed mice (*Slc25a47*^{lox/lox}) with albumin (Alb) Cre mice (JAX stock #003574) to generate a new

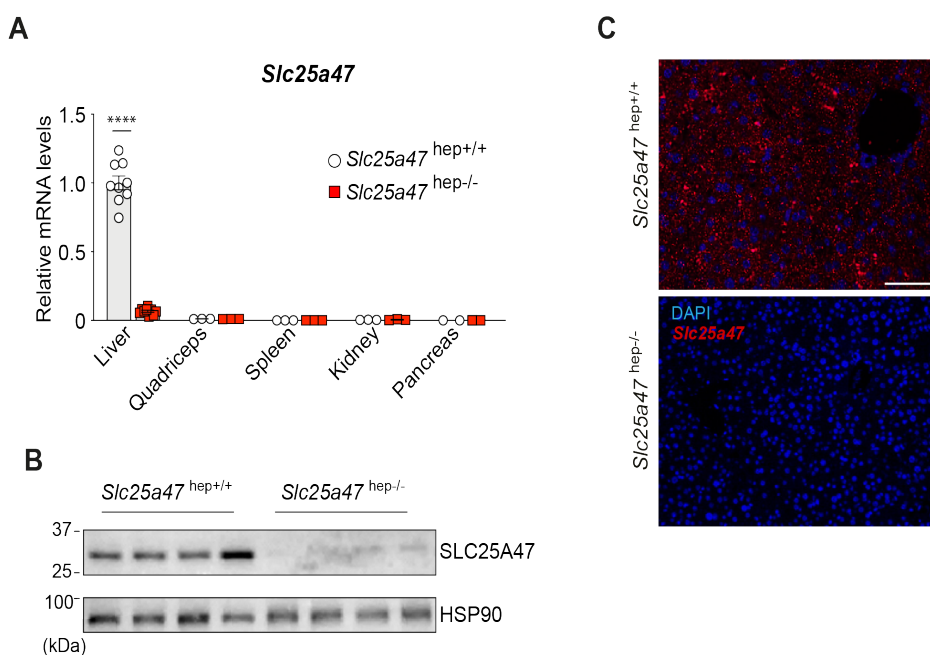


Figure 2.7. *Slc25a47*^{hep-/-} mice validation. (A) Relative *Slc25a47* mRNA level in different tissues from *Slc25a47*^{hep+/+} and *Slc25a47*^{hep-/-} mice (9-week-old, n=8 for liver, n=3 for other tissues). (B) Immunoblot validating the deletion of SLC25A47 in hepatic mitochondria from *Slc25a47*^{hep-/-} mice (9-week-old mice, n=4). HSP90 is used as a mitochondrial loading control. (C) RNAscope images depicting *Slc25a47* mRNA presence (red) only in the livers from *Slc25a47*^{hep+/+} mice. Nuclei are stained with DAPI (blue). Scale bar: 50 μ m. Error bars represent mean \pm S.E.M. **** $p < 0.0001$ relative to *Slc25a47*^{hep+/+} mice, as determined by unpaired Student's t-test.

mouse line carrying a somatic deletion of *Slc25a47* in hepatocytes (*Slc25a47*^{hep-/-}). RT-qPCR (Figure 2.7A), immunoblotting (Figure 2.7B), and RNAscope (Figure 2.7C) analyses confirmed deletion of the carrier in *Slc25a47*^{hep-/-} livers. 8-week-old *Slc25a47*^{hep-/-} male mice (fed a regular Chow diet) were distinctively shorter and lighter than their wild-type littermates (Figure 2.8A-C), suggesting that hepatic deletion of this

transporter has a broad impact on whole-body physiology. Moreover, 8-week-old *Slc25a47*^{hep-/-} male mice displayed a reduced liver to body weight ratio both in the fed and fasted state (Figure 2.8D). Furthermore, alanine transaminase (ALAT) and aspartate aminotransferase (ASAT) plasma levels were elevated, indicative of hepatic damage, which was more pronounced in the fasted state than when animals were fed *ad libitum* (Figure 2.8E-F).

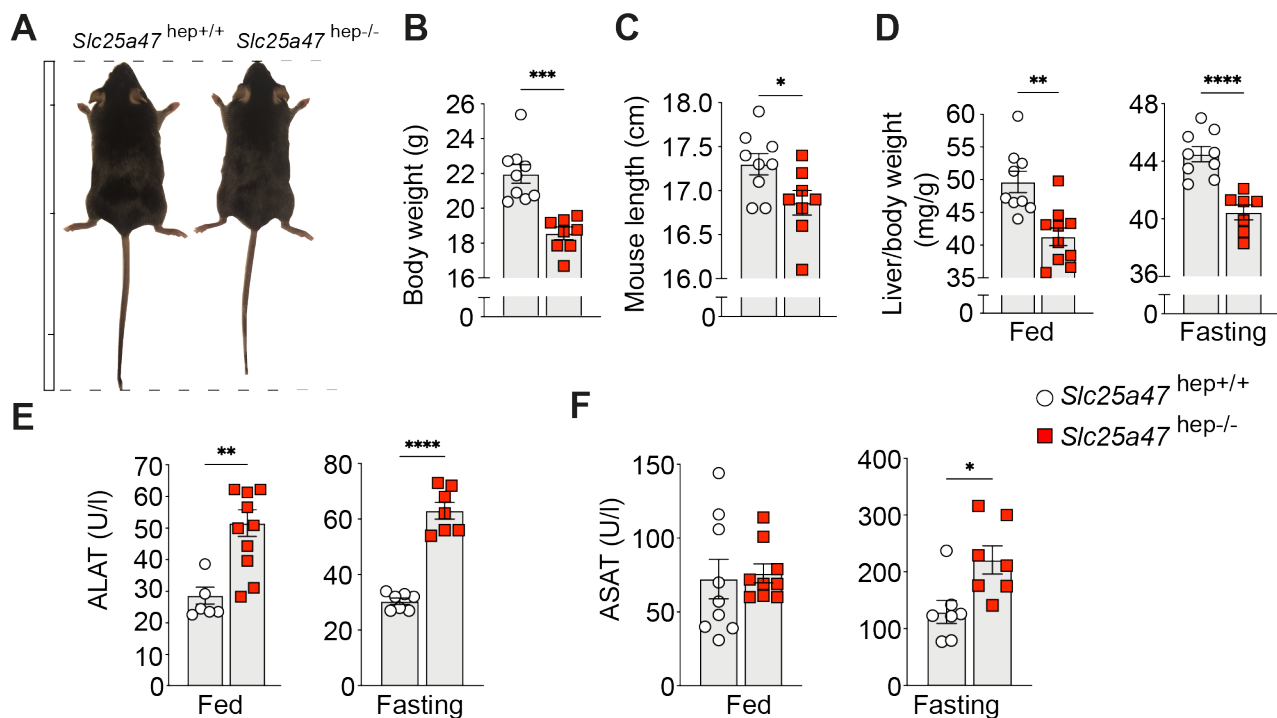


Figure 2.8. Deletion of *Slc25a47* is detrimental to hepatic function. (A) Representative pictures of *Slc25a47*^{hep+/+} and *Slc25a47*^{hep-/-} mice. Ruler represents 5 cm marks. (B) Body weight of 8-week-old *Slc25a47*^{hep+/+} (n=9) and *Slc25a47*^{hep-/-} (n=8) mice. (C) Length (cm) of 8-week-old *Slc25a47*^{hep+/+} and *Slc25a47*^{hep-/-} mice (n=9) measured from the nose to the tip of the tail. (D) Liver weight normalized to body weight in fed and fasted *Slc25a47*^{hep+/+} and *Slc25a47*^{hep-/-} mice (n=9). (E-F) Circulating plasma levels of hepatic markers alanine aminotransferase (ALAT, E) and aspartate transaminase (ASAT, F) in fed and fasted *Slc25a47*^{hep+/+} and *Slc25a47*^{hep-/-} mice (n=7-8). Error bars represent mean ± S.E.M. *p<0.05, **p<0.01, ***p<0.001, ****p<0.0001 relative to *Slc25a47*^{hep+/+} mice, as determined by unpaired Student's t-test.

Of note, during fasting the livers of these *Slc25a47*^{hep-/-} mice were paler suggestive of lipid accumulation (Figure 2.9A). Accordingly, light microscopy (Figure 2.9A), electron microscopy (EM) (Figure 2.9B), and biochemical analyses (Figure 2.9C-E) revealed abnormal lipid and cholesterol accumulation in the liver of both fed and fasted *Slc25a47*^{hep-/-} mice, consistent with GMAD analysis (Figure 2.5). Moreover, in the fed state, EM images and biochemical quantification revealed a depletion of glycogen stores (Figure 2.9F-G) in *Slc25a47*^{hep-/-} livers suggestive of dysregulated glucose management in hepatocytes. This observation prompted us to further assess the role of SLC25A47 in the regulation of glucose homeostasis. We found that fasted *Slc25a47*^{hep-/-} mice were markedly hypoglycemic (Figure 2.9H). Interestingly, *Slc25a47*^{hep-/-} mice displayed increased levels of circulating lactic acid in both fed and fasted state compared to their control littermates (Figure 2.9I). To investigate whether the hypoglycemic phenotype could arise from an impairment in *de novo* glucose production, we subjected the mice to a pyruvate tolerance test (PTT). Glycemic excursion in response to pyruvate was significantly compromised in the *Slc25a47*^{hep-/-} mice (Figure 2.9J). In sum, *Slc25a47*^{hep-/-} mice display a wide range of metabolic alterations ranging from altered gluconeogenesis and liver lipid metabolism to decreased glycogen storage.

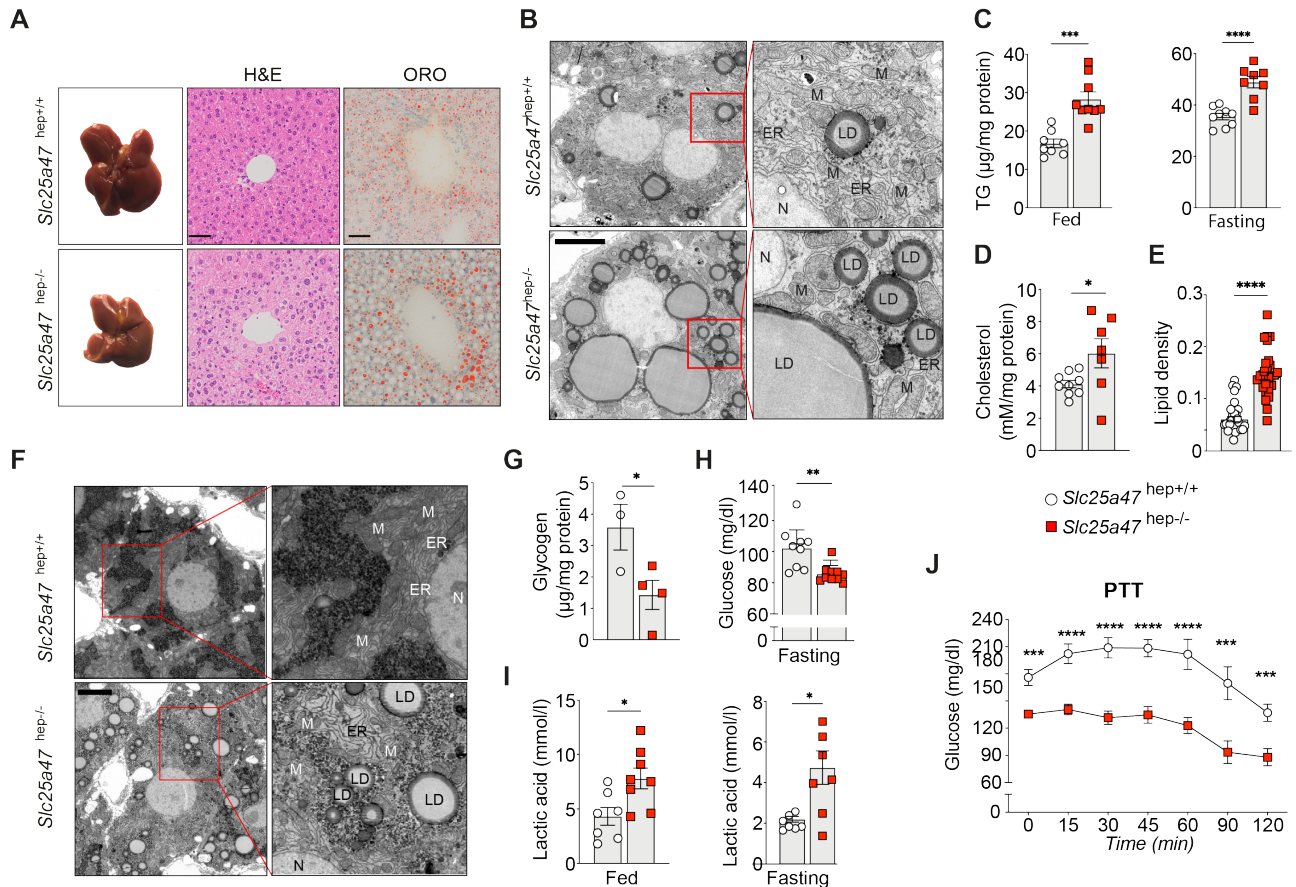


Figure 2.9. Hepatic deletion of *Slc25a47* leads to a wide range of metabolic alterations. (A) Representative pictures of livers and their staining with hematoxylin/eosin (H&E) and oil red O (ORO) to visualize tissue structure and neutral lipids, respectively, from fasted *Slc25a47*^{hep+/+} and *Slc25a47*^{hep-/-} mice. Scale bar: 20 μ m. (B) Representative pictures of livers from fasted *Slc25a47*^{hep+/+} and *Slc25a47*^{hep-/-} mice taken by transmission electron microscopy (EM). Magnifications (right panels) are delineated by the red square. LD: lipid droplet; ER: endoplasmic reticulum; N: nucleus; M: mitochondria. Scale bar: 5 μ m. (C) Quantification of triglyceride (TG) content in hepatic lipid extracts from fed or fasted 8-week-old *Slc25a47*^{hep+/+} and *Slc25a47*^{hep-/-} (n=8-9) mice. (D) Hepatic cholesterol levels in 8-week-old fasted *Slc25a47*^{hep+/+} (n=9) and *Slc25a47*^{hep-/-} (n=7) mice. (E) Lipid density in hepatocytes from fasted *Slc25a47*^{hep+/+} and *Slc25a47*^{hep-/-} mice obtained by lipid droplet number per hepatocyte area on EM pictures (average of 30 hepatocytes in 2 biological replicates per genotype). (F) Representative pictures of livers from fed *Slc25a47*^{hep+/+} and *Slc25a47*^{hep-/-} mice taken by EM. The red square shows a magnification (right panels) to depict glycogen content (black dots) in a single hepatocyte. (G) Quantification of glycogen content in extracts from control (n=3) and *Slc25a47*-deficient (n=4) livers (from 8-week-old mice). (H) Blood glucose levels in fasted 12-week-old *Slc25a47*^{hep+/+} and *Slc25a47*^{hep-/-} mice (n=8). (I) Circulating lactic acid measured in the plasma of 8-week-old fed and fasted *Slc25a47*^{hep+/+} and *Slc25a47*^{hep-/-} mice (n=7). (J) Blood glucose levels over time measured during pyruvate tolerance test (PTT) in 10-week-old *Slc25a47*^{hep+/+} and *Slc25a47*^{hep-/-} mice (n=8). Error bars represent mean \pm S.E.M. *p<0.05, **p<0.01, ***p<0.001 and ****p<0.0001 relative to *Slc25a47*^{hep+/+} mice, as determined by unpaired Student's t-test (C, D, E, G, H, I) or two-way ANOVA and Bonferroni post-hoc correction (J).

2.3 Hepatic *Slc25a47* deficiency leads to impaired mitochondrial respiration

We next interrogated if a chronic energy deficiency in *Slc25a47*^{hep-/-} hepatocytes due to mitochondrial dysfunction could underlie the broad and diverse metabolic phenotypes described above. In line with this assumption, ATP levels were strongly diminished in the livers of 8-week-old *Slc25a47*^{hep-/-} male mice (Figure 2.10A) suggesting impaired OXPHOS. To assess the role of SLC25A47 in regulating mitochondrial function, we performed high-resolution respirometry assays on liver lysates and isolated mitochondria from fed and fasted *Slc25a47*^{hep-/-} mice and their control littermates. We used a combination of drugs and substrates to assess leaked and coupled, complex I- and complex II-driven respiration. Compared to *Slc25a47*^{hep+/+} mice, liver and mitochondrial extracts from fed and fasted *Slc25a47*^{hep-/-} mice respired significantly less, even in the presence of the complex I inhibitor, Rotenone (ROT) (Figure 2.10B-E). Importantly, the defect in respiration did not appear to be restricted to any given complex or limited to coupled or uncoupled respiration. In line with our cellular data (Figure 2.6B, C), addition of the chemical uncoupling agent FCCP failed to rescue the respiratory phenotype observed in mitochondria isolated from *Slc25a47*^{hep-/-} livers, confirming that SLC25A47 do not show uncoupling function. We then extended these results by assessing the fatty acid oxidation potential of *Slc25a47*^{hep-/-} mitochondria and found that palmitoyl- and octanoyl-carnitine (C-POM)-driven respiration was also severely impaired in mitochondria extracted from *Slc25a47*^{hep-/-} livers (Figure 2.10F). Taken together, our results demonstrate that *Slc25a47*^{hep-/-} livers suffer from a shortage of cellular ATP as a consequence of impaired respiration most likely arising from a global mitochondrial defect. SLC25A47 seems thus essentially required for proper mitochondrial respiration in the liver.

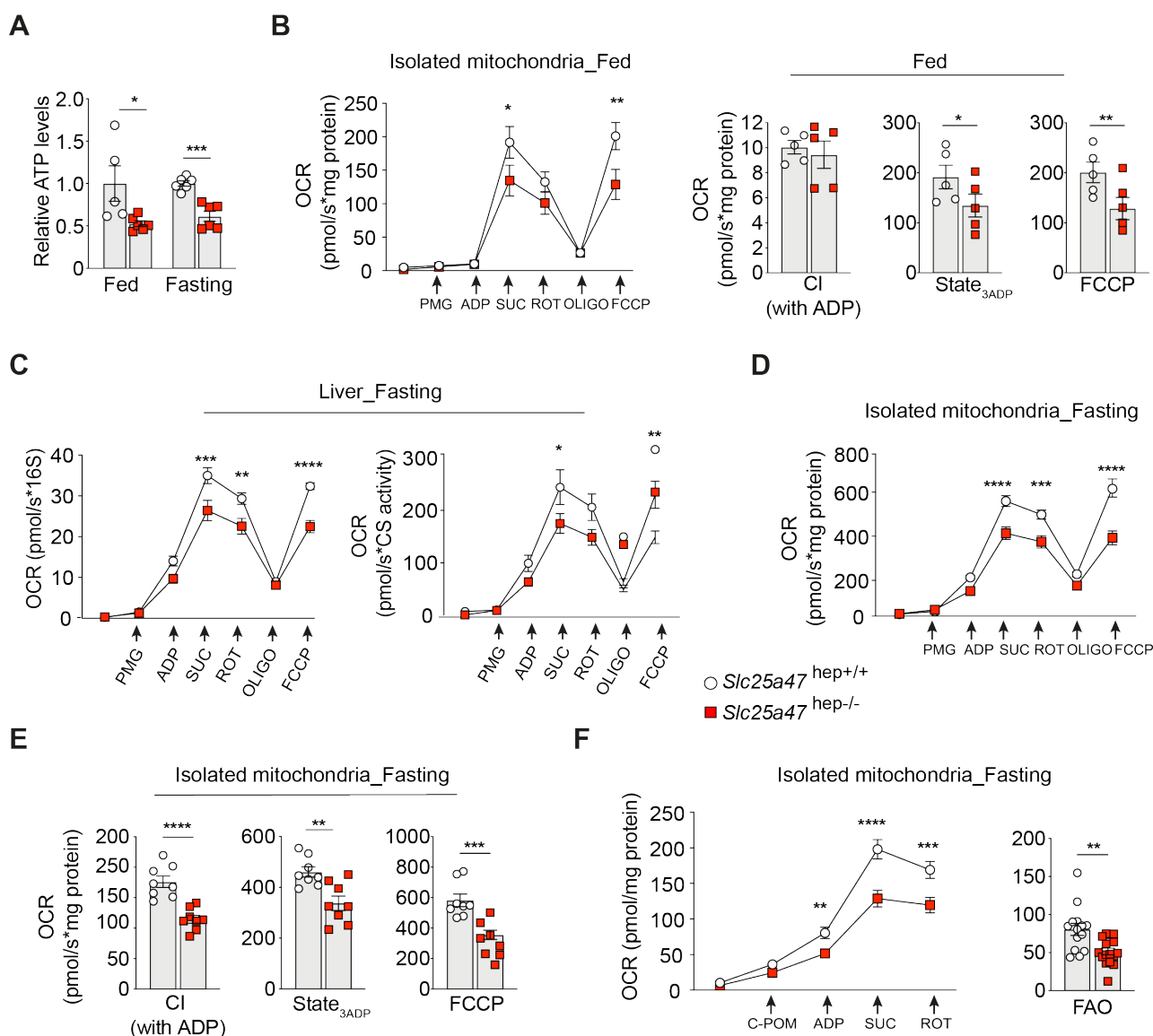


Figure 2.10. *Slc25a47*^{hep-/-} mice display hepatic mitochondrial dysfunction. (A) Relative ATP levels assessed in whole liver lysate from fed and fasted 8-week-old *Slc25a47*^{hep+/+} and *Slc25a47*^{hep-/-} mice and normalized to *Slc25a47*^{hep+/+} ATP content (n=5-6). (B) Time course (left) and bar graph quantification (right) representing OCR of freshly isolated mitochondria from livers of fed 8-week-old *Slc25a47*^{hep+/+} and *Slc25a47*^{hep-/-} mice (n=5). PMG: Pyruvate, Malate, Glutamate; SUC: Succinate, ROT: Rotenone, OLIGO: Oligomycin. (C) Time course oxygen consumption rate (OCR) of liver homogenate from fasted 9-week-old *Slc25a47*^{hep+/+} and *Slc25a47*^{hep-/-} mice normalized on mtDNA content (16S) (left) or citrate synthase (CS) (right) (n=8). (D, E) Time course (D) and bar graph quantification (E) representing OCR of freshly isolated mitochondria from livers of fasted 8-week-old *Slc25a47*^{hep+/+} and *Slc25a47*^{hep-/-} mice (n=8). CI (with ADP): Complex I substrates (PMG) in the presence of ADP. State_{3ADP} corresponds to ADP-stimulated respiration obtained with PMG, Succinate, Rotenone, and ADP. (F) Time course and bar graphs representing OCR of freshly isolated mitochondria from livers of fasted 8-week-old *Slc25a47*^{hep+/+} and *Slc25a47*^{hep-/-} mice (n=8). C-POM: palmitoyl- and octanoyl-carnitine with malate. FAO: Fatty acid oxidation substrates (C-POM) were added in the presence of ADP. Error bars represent mean \pm S.E.M. *p<0.05, **p<0.01, ***p<0.001 and ****p<0.0001 relative to *Slc25a47*^{hep+/+} mice, as determined by unpaired Student's t-test (A, E and bar graphs in B, F) or two-way ANOVA and Bonferroni post-hoc correction (B, C, D, F).

2.4 *Slc25a47* deficiency leads to a strong induction of the mitochondrial stress response

We then performed RNA-seq analysis on livers from fasted and *ad libitum* fed 9-week-old *Slc25a47*^{hep-/-} and *Slc25a47*^{hep+/+} mice in order to investigate the molecular responses triggered by SLC25A47 LOF. Principal component analysis (PCA) revealed a marked separation between the two genotypes suggesting robust transcriptional changes induced upon loss of hepatic *Slc25a47* (Figure 2.11A). Gene set enrichment analysis (GSEA) indicated that the mitochondrial stress response (MSR) was the most significantly enriched signature in our dataset in both fed and fasted state (Figure 2.11B, C). The MSR is a highly conserved pathway triggered by various mitochondrial stressors that activates a wide range of factors to restore normal mitochondrial functions⁵⁴. Accordingly, the transcriptome of *Slc25a47*^{hep-/-} livers was characterized by a strong upregulation of mitochondrial stress markers, including TFs (*Atf3*, *Atf4*, *Atf5*, *Ddit3* or *Chop*), enzymes (*Asns*, *Pck2*) and transporters (*Slc1a4*, *Slc1a5*) (Figure 2.11D, E).

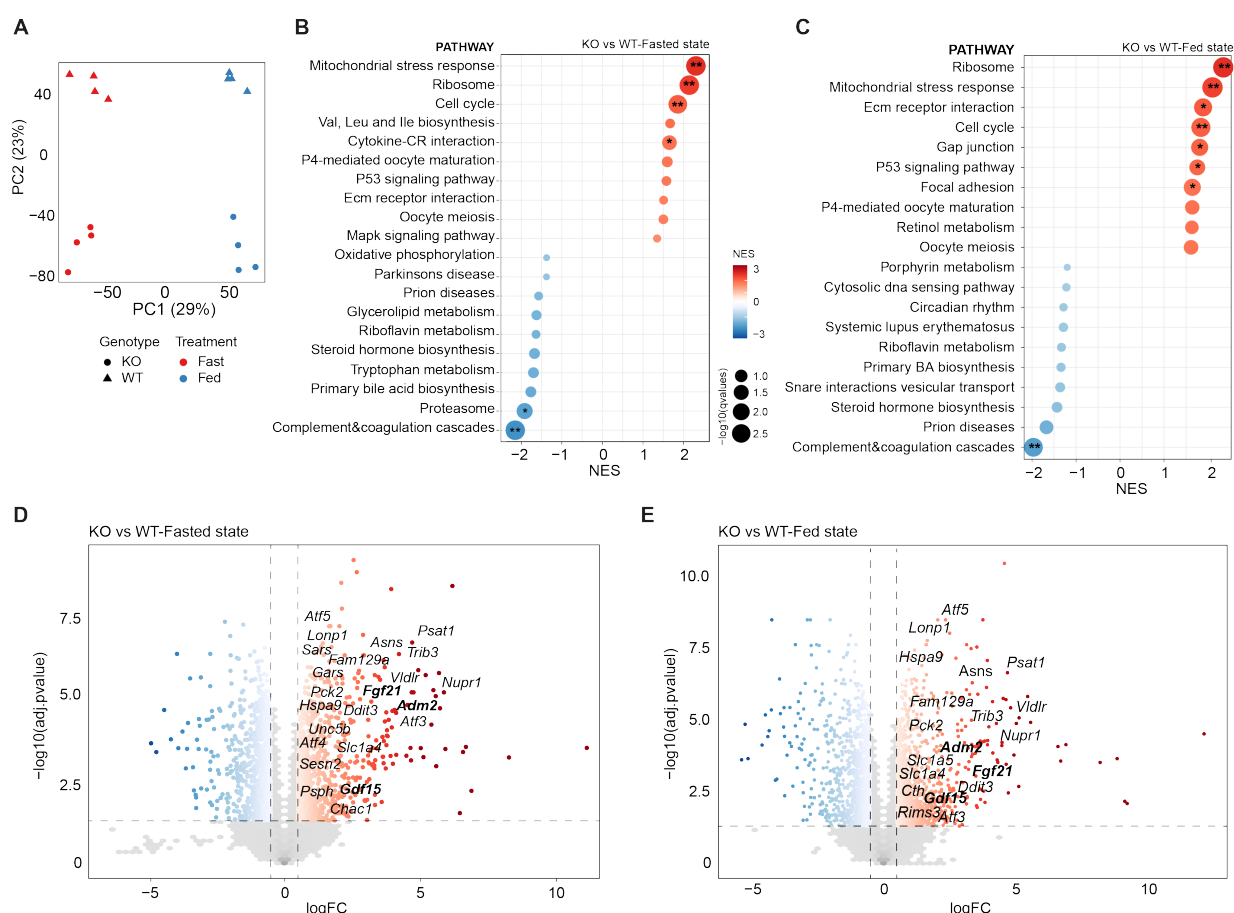


Figure 2.11. Loss of hepatic SLC25A47 triggers the mitochondrial stress response. (A) Principal component analysis (PCA) performed on RNA-seq data of livers from fed and fasted 9-week-old *Slc25a47*^{hep+/+} (WT) and *Slc25a47*^{hep-/-} (KO) mice (n=4). (B-C) Gene Set Enrichment Analysis (GSEA) from RNA-seq data, showing mitochondrial stress response as the most enriched pathway in KO compared to WT livers in both fasted (B) and (C) fed state. *qvalue<0.05, **qvalue<0.01. NES: normalized enrichment score. (D-E) Volcano plots representing all the significantly downregulated (blue) and upregulated (red) genes in the liver from fasted (D) or fed (E) 9-week-old KO mice compared to controls. The displayed names represent mitochondrial stress genes. Mitokine genes are highlighted in bold. FC: fold change.

The MSR encompasses and overlaps with the UPR^{mt}, activated to restore protein homeostasis upon mitochondrial protein misfolding^{58,161}. RNA and protein levels of the prototypical UPR^{mt} mediators, such as mitochondrial heat shock proteins (*Hspa9*, *Hspd1*, *Hspa1a*) and proteases (*Yme1l1*, *Lonp1*) were robustly induced in *Slc25a47*^{hep-/-} livers in both fasted and fed state (Figure 2.12A, B). In addition to cell-autonomous communication from mitochondria to the nucleus, mitochondrial stress is also typified by the expression, and secretion, of non-cell-autonomous factors that mediate inter-tissue communication to integrate the cellular mitochondrial stress response within a global metabolic reprogramming of the organism^{54,57,162}. These factors are referred to as mitokines and were first described in invertebrates^{163,164}. In mammals, FGF21^{165–167}, GDF15⁸⁰ and ADM2^{117,118} are the best characterized. All three mitokines were strongly induced in the livers of *Slc25a47*^{hep-/-} mice (Figure 2.11D, E) but FGF21 seemed to be the main secreted factor, as evidenced by its plasma levels in both fasted and fed conditions (Figure 2.12C). Collectively, our data demonstrate that *Slc25a47* LOF has a profound impact on mitochondrial homeostasis and leads to potent and chronic activation of the MSR. This results in the hepatic secretion of mitokines, that communicate the MSR to distant tissues with potential effects on whole-body physiology.

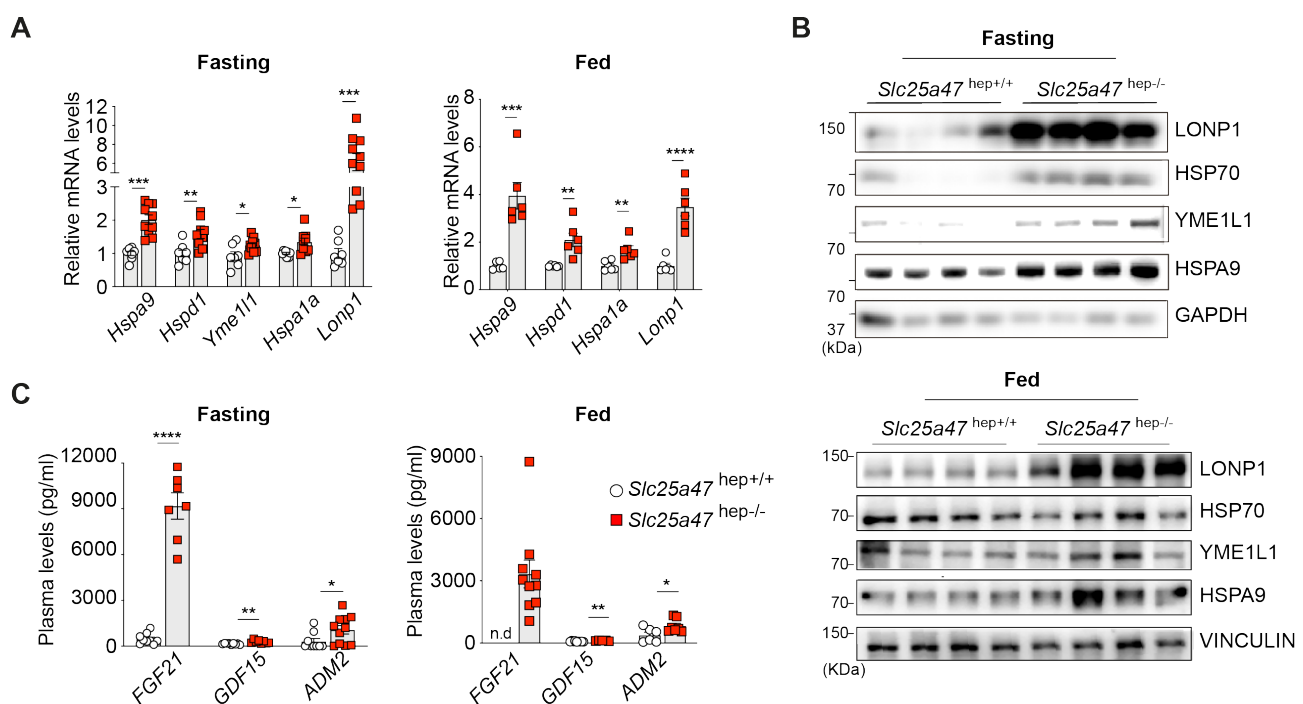


Figure 2.12. Loss of hepatic SLC25A47 triggers the mitochondrial stress response. (A-B) Relative gene expression (**A**, n=6-10) and immunoblot (**B**, n=4) of prototypical mitochondrial unfolded protein response (UPR^{mt}) mediators from livers of fasted and fed 8-week-old *Slc25a47*^{hep+/+} and *Slc25a47*^{hep-/-} mice. **(C)** Plasma quantification of FGF21, GDF15 and ADM2 mitokines in fasted and fed 8-week-old *Slc25a47*^{hep+/+} (n=8) and *Slc25a47*^{hep-/-} (n=7) mice. n.d: not detected. Error bars represent mean ± S.E.M. *p<0.05, **p<0.01, ***p<0.001 and ****p<0.0001 relative to *Slc25a47*^{hep+/+} mice, as determined by unpaired Student's t-test.

2.5 Partial ablation of *Slc25a47* is sufficient to trigger mitochondrial dysfunction

To study whether a modulation of *Slc25a47* expression could lead to the metabolic alterations observed in *Slc25a47*^{hep-/-} mice, we took advantage of the *Slc25a47* heterozygous (*Slc25a47*^{hep+/-}) mice, which carry a single allele of the gene. These mice showed a partial (~50%) reduction in *Slc25a47* mRNA levels (Figure 2.13A), without displaying differences in body weight, stature or liver over body weight ratio compared to control littermates (Figure 2.13B-D). Nevertheless, as *Slc25a47*^{hep-/-} mice (Figure 2.9), *Slc25a47*^{hep+/-} mice showed reduced hepatic *de novo* glucose production (Figure 2.13E) and increased plasma lactic acid levels (Figure 2.13F). Moreover, heterozygous livers presented reduced mitochondrial respiration (Figure 2.13G) and decreased ATP content compared to controls. Interestingly, *Slc25a47*^{hep+/-} mice showed a mild induction of the prototypical UPR^{mt} genes and a significant increase of FGF21 levels (Figure 2.13J).

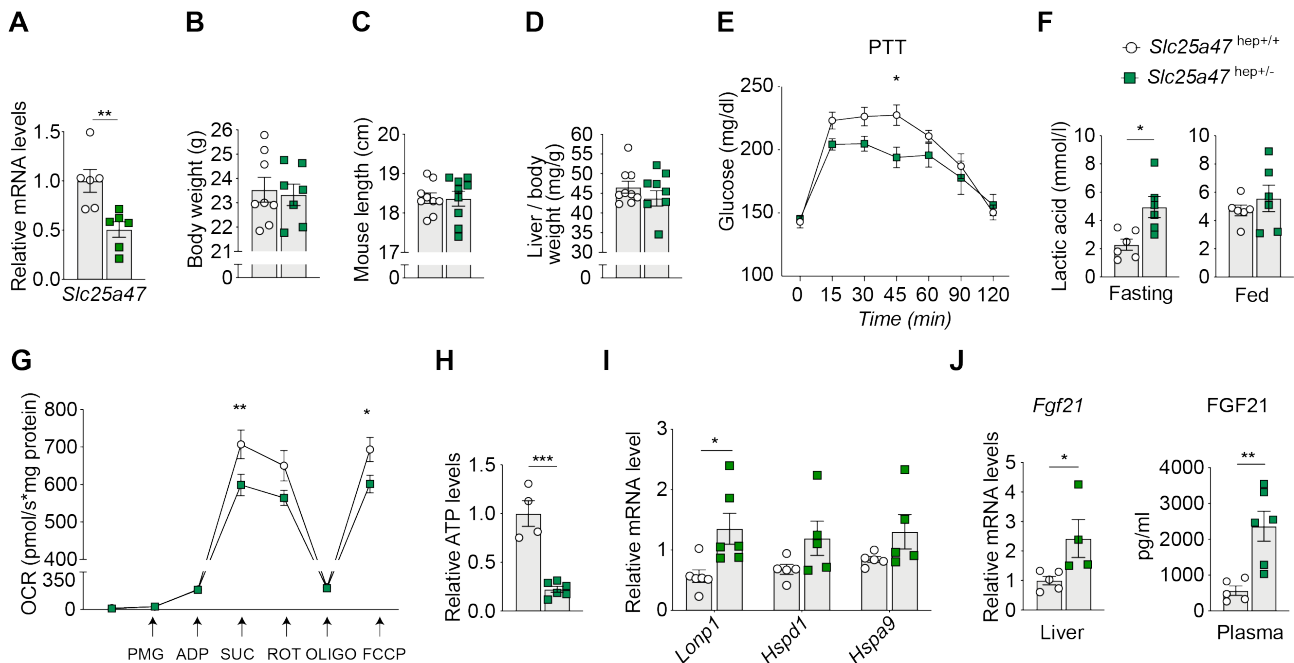


Figure 2.13. *Slc25a47* heterozygous mice. (A) Relative hepatic levels of *Slc25a47* in 8-week-old fasted *Slc25a47*^{hep+/+} and heterozygous *Slc25a47*^{hep+/-} mice (n=6). (B-D) Body weight (B), length (C) and liver over body weight ratio (D) of 8-week-old fasted *Slc25a47*^{hep+/+} and *Slc25a47*^{hep+/-} mice (n=7-8). (E) Blood glucose levels during pyruvate tolerance test (PTT) in *Slc25a47*^{hep+/+} and *Slc25a47*^{hep+/-} mice (n=8). (F) Plasma lactate levels in fasted and fed 8-week-old *Slc25a47*^{hep+/+} and *Slc25a47*^{hep+/-} mice (n=6). (G) Oxygen consumption rate (OCR) in freshly isolated mitochondria from livers of mice described in panel A (n=6). (H) Relative hepatic ATP levels in mice described in panel A (n=4-6). (I) Relative hepatic mRNA levels of prototypical UPR^{mt} markers in fasted mice (n=6). (J) Relative hepatic mRNA levels (left) and plasma levels of FGF21 in mice described in panel A (n=4-6). Error bars represent mean \pm S.E.M. *p<0.05, **p<0.01 relative to *Slc25a47*^{hep+/+} mice, as determined by unpaired Student's t-test (A-D, F, H-J) or two-way ANOVA and Bonferroni post-hoc correction (E, G).

2.6 FGF21-dependent systemic phenotypes upon loss of Slc25a47

Because FGF21 plasma levels were very high in the *Slc25a47*^{hep-/-} and *Slc25a47*^{hep+/-} mice, we examined the molecular link between the loss of this carrier and the induction of this mitokine. We first performed an *in silico* analysis of the murine *Fgf21* promoter region and found putative binding sites for over 30 transcription factors (top 10 TFs depicted in Figure 2.14A). We then reused our RNA-seq data, from *Slc25a47*^{hep-/-} mice (Figure 2.11), to perform correlation analyses between these transcription factors and *Fgf21* mRNA levels. We found that the stress-induced proteins ATF4 and ATF5 strongly correlated with *Fgf21*, suggesting a causative link between these transcription factors and the induction of this mitokine (Figure 2.14B). This was confirmed by chromatin immunoprecipitation (ChIP) assays, which revealed a robust recruitment of both ATF4 and ATF5 to the *Fgf21* promoter specifically in *Slc25a47*^{hep-/-} livers (Figure 2.14C).

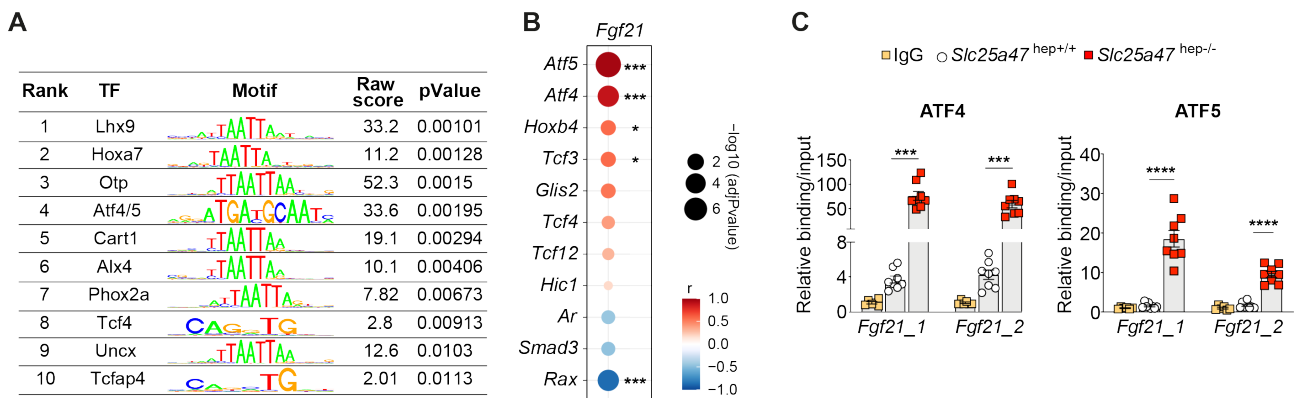


Figure 2.14. *Fgf21* upregulation in *Slc25a47*^{hep-/-} mice is mediated by ATF4 and ATF5. (A) 10 most statistically significant transcription factors (TF) binding the *Fgf21* promoter obtained through motif enrichment analysis. (B) Pearson's correlation analysis between transcription factors (TFs) and *Fgf21* obtained using RNAseq data from livers of both fed and fasted *Slc25a47*^{hep+/-} and *Slc25a47*^{hep-/-} mice. (C) Chromatin immunoprecipitation (ChIP) for ATF4 and ATF5 followed by qPCR on two binding sites (*Fgf21*_1 and *Fgf21*_2) on the *Fgf21* promoter, showing increased binding for both TFs in *Slc25a47*^{hep-/-} compared to control mice. IgG was used as negative control for the ChIP. Error bars represent mean \pm S.E.M. * $p < 0.05$, ** $p < 0.01$, *** $p < 0.001$ and **** $p < 0.0001$ relative to *Slc25a47*^{hep+/-} mice, as determined by one-way ANOVA.

We, thus, concluded that the mitochondrial stress triggered by the loss of SLC25A47 led to an induction of *Fgf21* mediated by the stress-related factors ATF4 and ATF5. FGF21 mediates a multitude of metabolic actions, ranging from the regulation of food intake to the control of lipid and glucose homeostasis, and beiging of white adipose tissue (WAT) and its chronic upregulation is known to induce a profound and persistent hypermetabolic state^{166,168}.

To investigate the contribution of FGF21 on the metabolic phenotypes observed in *Slc25a47*^{hep-/-} mice, we generated a new mouse line in which both *Slc25a47* and *Fgf21* were genetically ablated in hepatocytes of C57BL/6 mice (*Slc25a47-Fgf21*^{hep-/-}, Figure 2.15 A, B) and conducted complete metabolic phenotyping of these animals (Figure 2.16, 2.17).

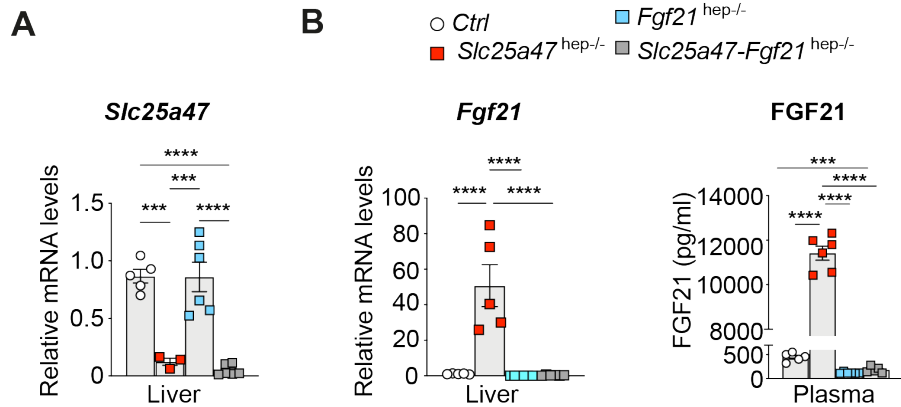


Figure 2.15. Validation of *Slc25a47-Fgf21*^{hep-/-} mice. (A) Relative mRNA levels of *Slc25a47* in livers from control (Ctrl), *Slc25a47*^{hep-/-}, *Fgf21*^{hep-/-} and *Slc25a47-Fgf21*^{hep-/-} mice (n=3-5). (B) Relative hepatic mRNA (left) and plasma protein (right) levels of FGF21 from fasted Ctrl, *Slc25a47*^{hep-/-}, *Fgf21*^{hep-/-} and *Slc25a47-Fgf21*^{hep-/-} mice. Error bars represent mean ± S.E.M. **p<0.01, ***p<0.001 and ****p<0.0001 relative to Ctrl mice, as determined by one-way ANOVA and Tukey's multiple comparison test.

Most of the morphological and systemic phenotypes of *Slc25a47*^{hep-/-} mice were fully rescued in double-mutant mice. In particular, body length (Figure 2.16A, B) and body weight (Figure 2.16C) were normal in 8-week-old control and *Slc25a47-Fgf21*^{hep-/-} animals, while abnormally reduced in *Slc25a47*^{hep-/-} mice. Similarly, food intake was markedly increased in *Slc25a47*^{hep-/-} animals while completely normalized upon double ablation of *Slc25a47* and *Fgf21* (Figure 2.16D).

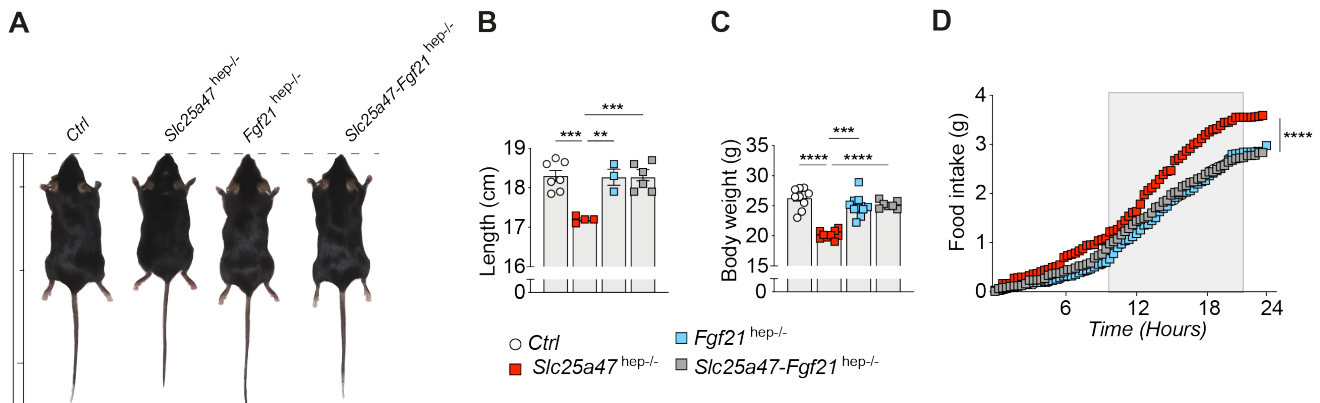


Figure 2.16. FGF21-dependent phenotypes in *Slc25a47*^{hep-/-} mice. (A) Representative pictures of Ctrl, *Slc25a47*^{hep-/-}, *Fgf21*^{hep-/-} and *Slc25a47-Fgf21*^{hep-/-} mice. The ruler shows 4 cm marks. (B, C) Length (measured from the nose to the tip of the tail) (B) and body weight (C) of 8-week-old Ctrl, *Slc25a47*^{hep-/-}, *Fgf21*^{hep-/-} and *Slc25a47-Fgf21*^{hep-/-} mice (n=3-10) (D) Cumulative food intake over time (24h) measured in 17-week-old mice (n=8). The grey rectangle represents the dark/night phase. Error bars represent mean ± S.E.M. **p<0.01, ***p<0.001 and ****p<0.0001 relative to Ctrl mice, as determined by one-way ANOVA and Tukey's multiple comparison test (B, C) or two-way ANOVA and Bonferroni *post-hoc* correction (D). Asterisks in panel D represent only *Slc25a47*^{hep-/-} versus Ctrl.

The combination of reduced body weight and increased food intake in *Slc25a47*^{hep-/-} mice prompted us to investigate energy homeostasis in these animals. Consistent with the physiological role of FGF21, *Slc25a47*^{hep-/-} mice presented a profound beiging of subcutaneous WAT (scWAT, Figure 2.17A), which involved the activation of brown-fat specific genes in white adipocytes (Figure 2.17B).

This phenomenon was associated with a strong increase in energy expenditure (EE) both during the day and night (Figure 2.17C) which was not linked to increased activity (Figure 2.17D). In contrast, scWAT beiging and EE were normal in *Slc25a47-Fgf21*^{hep-/-} animals (Figure 2.17 A-D). Altogether, these results support a model in which the profound hepatic mitochondrial stress induced in *Slc25a47*^{hep-/-} livers triggers an FGF21-driven hypermetabolic phenotype in *Slc25a47*^{hep-/-} mice.

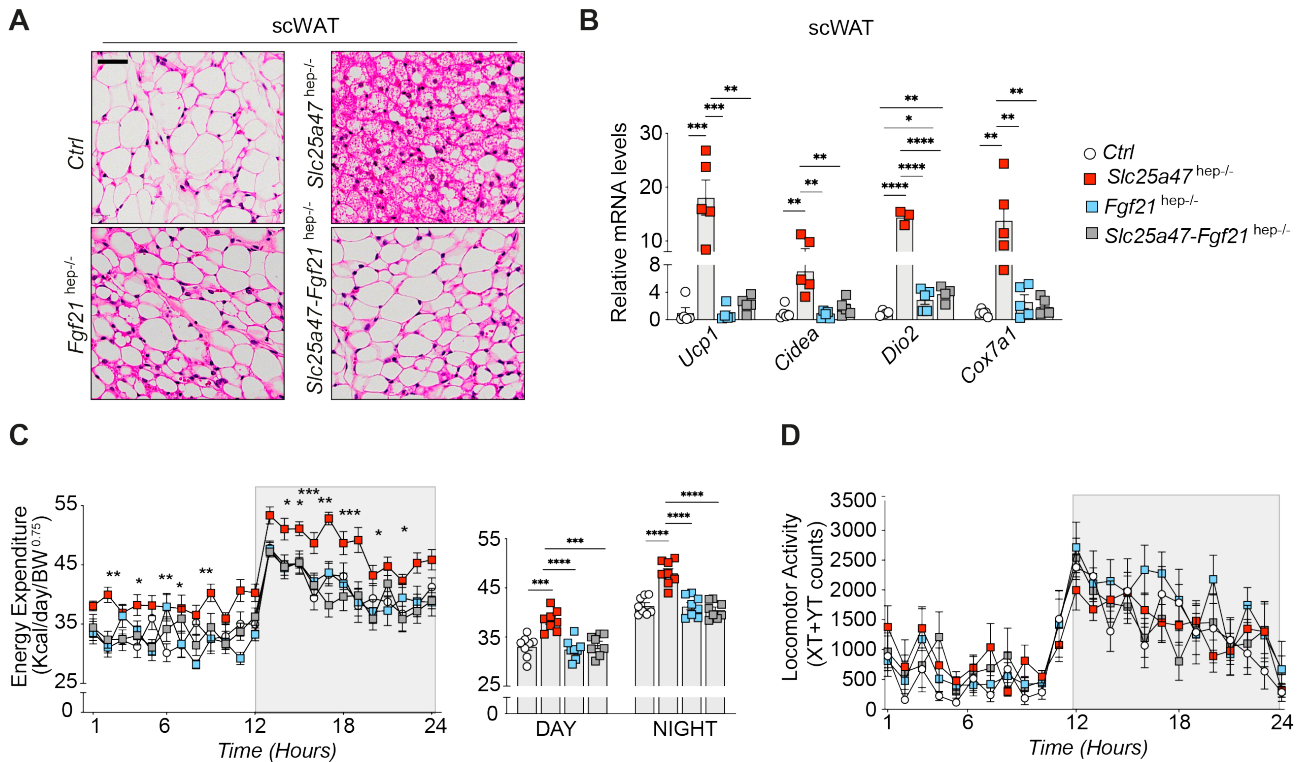


Figure 2.17. FGF21 drives the hypermetabolic phenotype in *Slc25a47*^{hep-/-} mice. (A) Representative pictures of subcutaneous white adipose tissue (scWAT) stained with H&E to visualize the tissue structure in 8-week-old fasted Ctrl, *Slc25a47*^{hep-/-}, *Fgf21*^{hep-/-} and *Slc25a47-Fgf21*^{hep-/-} mice. Scale bar: 20 μm. (B) Relative gene expression of beiging markers in scWAT of mice described in panel A (n=5). (C) Energy expenditure (EE) measured in 13-week-old mice (n=8). The grey rectangle represents the dark/night phase. The bar graph shows the average EE during the light (DAY) or dark (NIGHT) phase. (E) Total locomotor activity (obtained as a sum of XT and YT counts) in 13-week-old mice measured in the TSE System (n=8). Error bars represent mean ± S.E.M. *p<0.05, **p<0.01, ***p<0.001 and ****p<0.0001, as determined by one-way ANOVA and Tukey's multiple comparison test (B, bar graph in C) or two-way ANOVA and Bonferroni post-hoc correction (C, D). Asterisks in C represent only *Slc25a47*^{hep-/-} versus Ctrl.

2.7 FGF21-independent hepatic phenotypes upon loss of *Slc25a47*

Contrary to what we observed at the systemic level, the liver-specific phenotypes of *Slc25a47*^{hep-/-} animals remained after the genetic deletion of *Fgf21*. In particular, 8-week-old male single *Slc25a47*^{hep-/-} and double *Slc25a47-Fgf21*^{hep-/-} mice were similarly affected by a strong decrease in the liver to body weight ratio (Figure 2.18A-B) and displayed comparable changes in histological representations, liver triglyceride (TG) (Figure 2.18A, C) and ALAT/ASAT (Figure 2.18D) levels upon fasting.

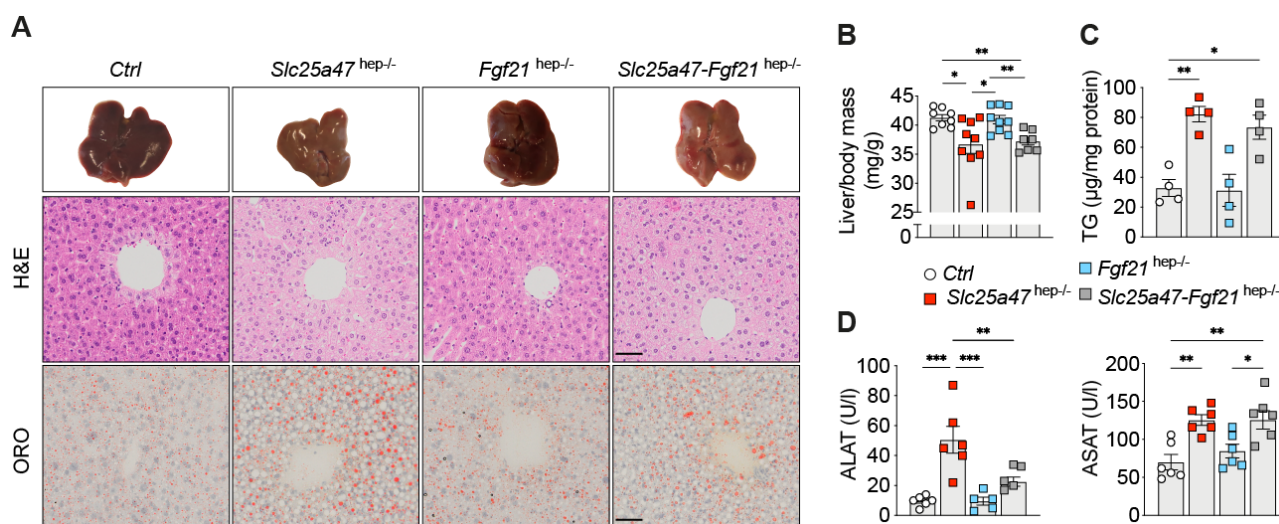


Figure 2.18. *Slc25a47-Fgf21*^{hep-/-} mice present FGF21-independent phenotypes. (A) Representative pictures of livers and their staining with hematoxylin and eosin (H&E) and Oil Red O (ORO) from Ctrl, *Slc25a47*^{hep-/-}, *Fgf21*^{hep-/-} and *Slc25a47-Fgf21*^{hep-/-} mice. Scale bar 20 μm. (B) Liver weight normalized on body weight in fasted 8-week-old Ctrl (n=8), *Slc25a47*^{hep-/-} (n=9), *Fgf21*^{hep-/-} (n=9) and *Slc25a47-Fgf21*^{hep-/-} (n=7) mice. (C) Hepatic triglyceride (TG) content in mice described in panel B (n=4). (D) Circulating plasma levels of ALAT and ASAT in 22-week-old fasted mice (n=6). Error bars represent mean ± S.E.M. *p<0.05, **p<0.01 and ***p<0.001 as determined by one-way ANOVA and Tukey's multiple comparison test (B-D).

All phenotypes associated with glucose homeostasis were also independent of FGF21 expression and its induction of scWAT beiging. Indeed, single *Slc25a47*^{hep-/-} and double *Slc25a47-Fgf21*^{hep-/-} mice displayed similar improved glucose clearance rates during oral glucose tolerance test (OGTT, Figure 2.19A). Accelerated glucose clearance can be indicative of increased insulin sensitivity or increased glucose consumption through enhanced glycolytic fluxes in metabolically active organs. To distinguish between these two possibilities, we subjected our transgenic animals to an insulin tolerance test (ITT) after mild (6-hour) fasting. Before insulin injection, single *Slc25a47*^{hep-/-} and double *Slc25a47-Fgf21*^{hep-/-} mice were already strikingly hypoglycemic (Figure 2.19B-C) but responded similarly to the actions of insulin (Figure 2.19B) demonstrating normal insulin signaling in *Slc25a47*-deficient animals. We then explored whether the impaired mitochondrial activity in SLC25A47-depleted livers forces hepatocytes to rely more on glycolytic metabolism. In line with this hypothesis, hepatic ATP levels were robustly reduced in both single *Slc25a47*^{hep-/-} and double *Slc25a47-Fgf21*^{hep-/-} mice (Figure 2.19D). Moreover, genetic ablation of *Fgf21* in *Slc25a47*^{hep-/-} mice failed to rescue the defects in mitochondrial respiration (Figure 2.19E). Both mouse lines also displayed elevated plasma lactate levels during OGTT (Figure 2.19F). Additionally, glycemic excursion after oral pyruvate administration (PTT, Figure 2.19G) was no longer observed in both single *Slc25a47*^{hep-/-} and double *Slc25a47-Fgf21*^{hep-/-} mice suggesting that ATP depletion in the liver of SLC25A47-deficient mice impairs normal gluconeogenesis, a hypothesis in line with the fasting-induced hypoglycemia observed in both *Slc25a47*^{hep-/-} and *Slc25a47-Fgf21*^{hep-/-} mice. Collectively, these data demonstrate that deletion of *Slc25a47* has a broad metabolic impact not only in the liver, but also on the whole organism. While several of the hypermetabolic phenotypes could be attributed

to chronic FGF21 signaling, those involved in glycemic control remain defective, even after removal of FGF21.

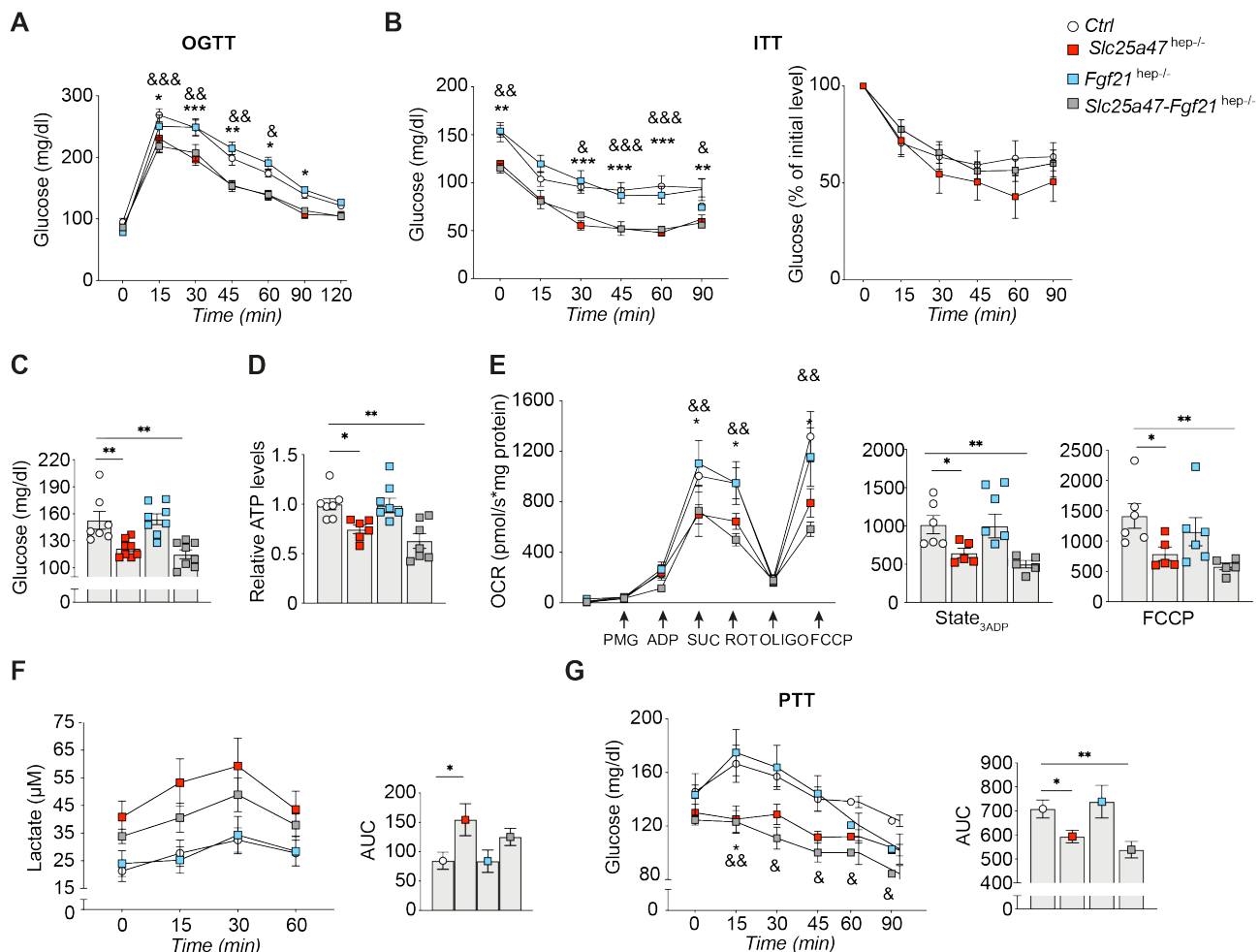


Figure 2.19. *Slc25a47-Fgf21^{hep-/-}* mice present FGF21-independent phenotypes. (A-B) Blood glucose levels measured during an oral glucose tolerance test (OGTT) (A) and insulin tolerance test (ITT) (B) in 12- and 15-week-old *Ctrl*, *Slc25a47^{hep-/-}*, *Fgf21^{hep-/-}* and *Slc25a47-Fgf21^{hep-/-}* mice, respectively (n=8). (C) Blood glucose levels measured after 6 hours fasting (7am-1pm) in *Ctrl*, *Slc25a47^{hep-/-}*, *Fgf21^{hep-/-}* and *Slc25a47-Fgf21^{hep-/-}* mice (n=7-8). (D) Relative ATP levels in whole liver lysate from fasted 22-week-old *Ctrl* (n=7), *Slc25a47^{hep-/-}* (n=6), *Fgf21^{hep-/-}* (n=7) and *Slc25a47-Fgf21^{hep-/-}* (n=7) mice. (E) Time course (left) and bar graphs (right) representing OCR of freshly isolated hepatic mitochondria from 22-week-old fasted *Ctrl* (n=6), *Slc25a47^{hep-/-}* (n=5), *Fgf21^{hep-/-}* (n=6), and *Slc25a47-Fgf21^{hep-/-}* (n=5) mice. (F) Blood lactate levels measured during OGTT in *Ctrl*, *Slc25a47^{hep-/-}*, *Fgf21^{hep-/-}* and *Slc25a47-Fgf21^{hep-/-}* mice, respectively (n=6). (G) Blood glucose levels measured during pyruvate tolerance test (PTT) in 20-week-old *Ctrl*, *Slc25a47^{hep-/-}*, *Fgf21^{hep-/-}* and *Slc25a47-Fgf21^{hep-/-}* mice (n=8). AUC: area under the curve. Error bars represent mean \pm S.E.M. For bar graphs in C, D, E, F, G: *p<0.05, **p<0.01 and ***p<0.001 as determined by one-way ANOVA and Tukey's multiple comparison test. For time course graphs in A, B, E, F, G: *p<0.05, **p<0.01 and ***p<0.001 for *Slc25a47^{hep-/-}* vs *Ctrl*; &p<0.05, &&p<0.01 and &&&p<0.001 for *Slc25a47-Fgf21^{hep-/-}* vs *Ctrl* as determined by two-way ANOVA and Bonferroni post-hoc correction.

2.8 Disruption of SLC25A47 in hepatocytes predisposes to liver fibrosis

To gain insights into the mechanism leading to liver injury in *Slc25a47^{hep-/-}* mice (Figure 2.8E-F), we performed cell type enrichment analysis on our RNA-seq data (Figure 2.20A). This analysis revealed

the presence of numerous inflammatory cells in the liver of knock-out animals (KO) along with an up-regulation of hepatic stellate cells (Figure 2.16A) suggesting a possible link between SLC25A47 LOF and hepatic fibrosis. To confirm this observation, we performed Sirius red staining and qRT-PCR on livers of young (8 weeks), mid-aged (32 weeks), and old (80 weeks) *Slc25a47*^{hep-/-} mice and control littermates (Figure 2.20B-D, Chow diet). Chronic loss of SLC25A47 was sufficient to trigger age-dependent collagen deposition and induce signs of inflammation, as shown by Sirius Red staining and gene expression analysis (Figure 2.20B-D).

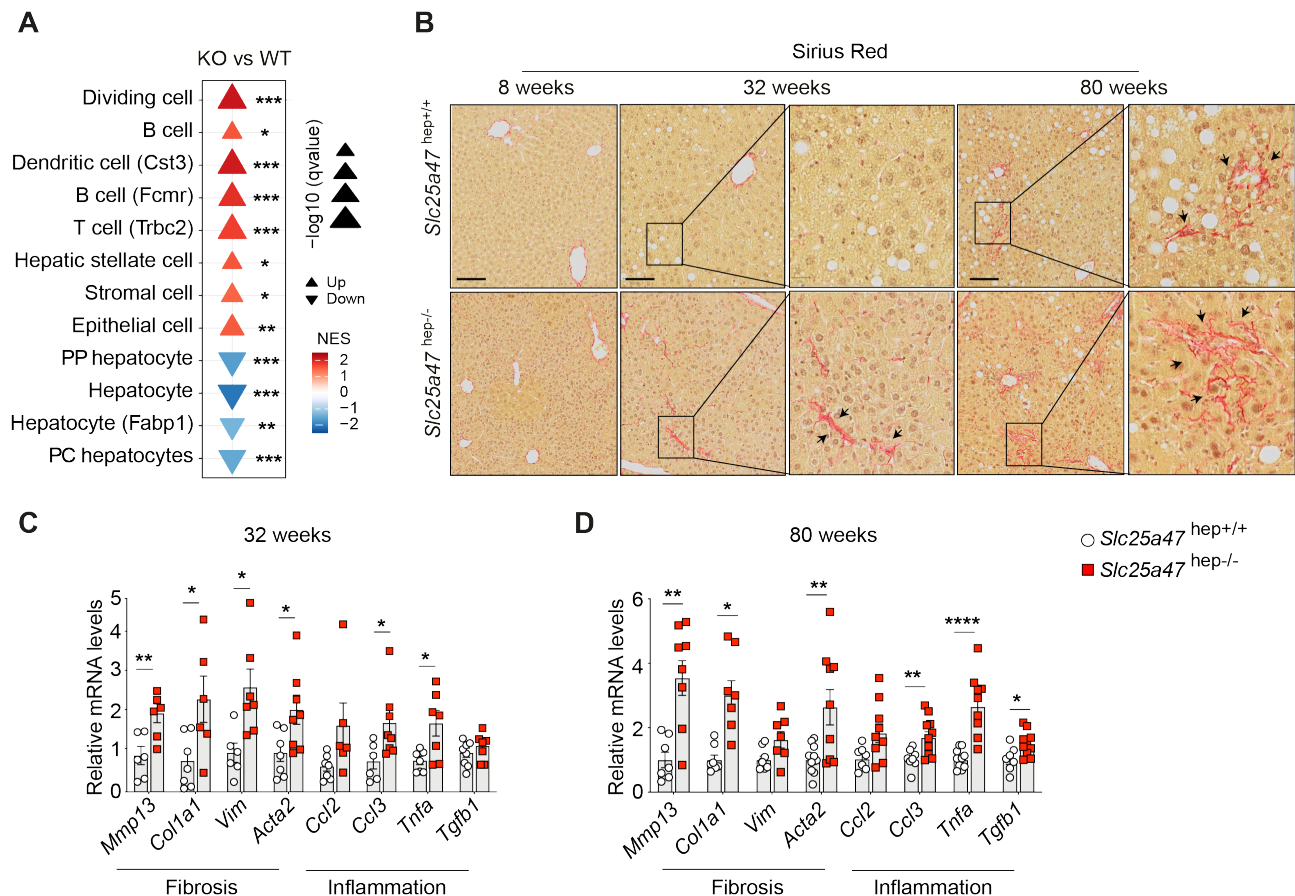


Figure 2.20. Chronic deletion of SLC25A47 leads to a fibrotic phenotype. (A) Cell type enrichment analysis from 8-week-old *Slc25a47*-deficient (KO) and *Slc25a47*^{hep+/+} (WT) livers. *qvalue<0.05, **qvalue<0.01, ***qvalue<0.001. (B) Representative pictures of livers stained with Sirius red to visualize hepatic fibrosis (collagen – in red) from fasted 8-week, 32-week and 80-week-old *Slc25a47*^{hep+/+} and *Slc25a47*^{hep-/-} mice (Chow Diet). The arrows indicate collagen deposition. Scale bar: 50 μm. (C-D) Relative hepatic mRNA levels of genes related to fibrosis and inflammation in 32- (C) and 80-week old (D) *Slc25a47*^{hep+/+} and *Slc25a47*^{hep-/-} mice (Chow Diet, n=6-10). Error bars represent mean ± S.E.M. *p<0.05, **p<0.01 and ****p<0.0001 relative to *Slc25a47*^{hep+/+} mice, as determined by unpaired Student's t-test.

We then challenged the knock-out animals with a pro-fibrotic, high-fat high-sucrose (HFHS) diet to further exacerbate the metabolic pressure in the liver. *Slc25a47*^{hep-/-} livers were much more inflamed than controls and displayed fibrosis, as shown by histological staining and gene expression levels for collagen deposition and immune cells infiltration markers (Figure 2.21A-B). These molecular and histological markers indicate that *Slc25a47*^{hep-/-} mice are predisposed to develop non-alcoholic

steatohepatitis (NASH) and hepatic fibrosis. Interestingly, *Slc25a47* hepatic deletion protected the mice against obesity (Figure 2.21C) and diabetes (Figure 2.21D-F) in accordance with their increased energy expenditure (Figure 2.17C) and improved glycemic profile (Figure 2.19) observed in normal Chow diet.

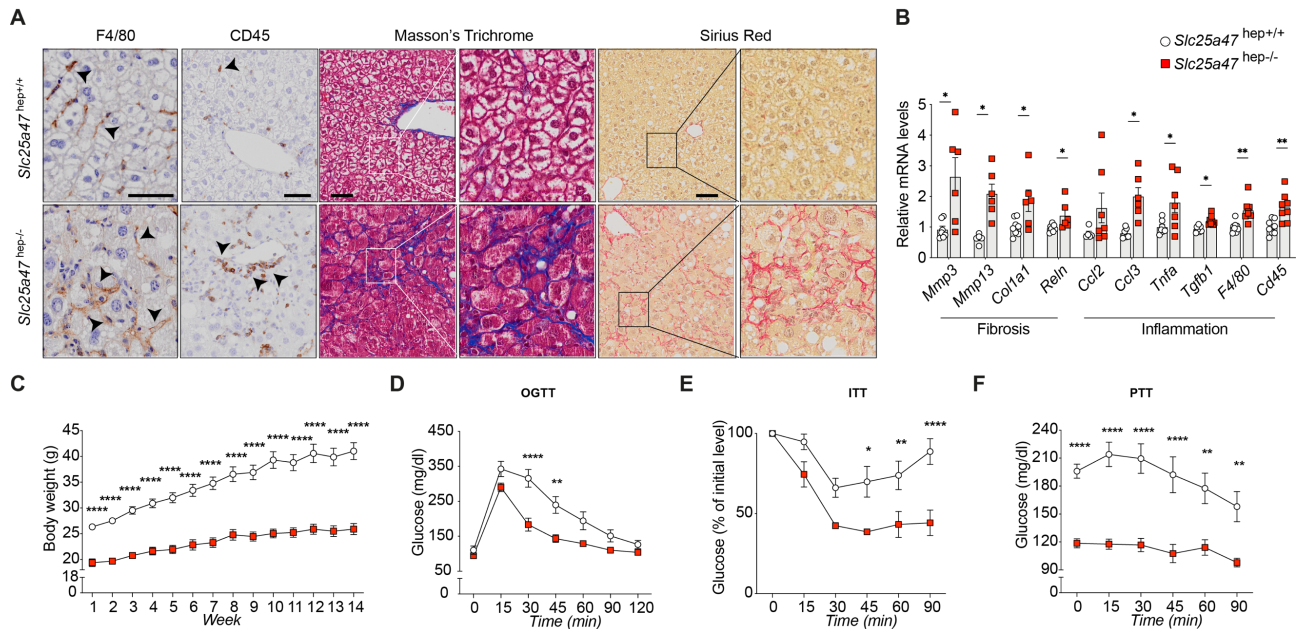


Figure 2.21. Disruption of SLC25A47 in hepatocytes predisposes to liver fibrosis. (A) Representative images of hepatic tissue stained for F4/80 and CD45 positive cells, Masson's trichrome, and Sirius red in high-fat high-sucrose (HFHS) diet fed *Slc25a47*^{hep+/+} and *Slc25a47*^{hep-/-} 22-week-old mice. Scale bar: 50 μ m. Arrows indicate F4/80 and CD45 positive cells. (B) Relative hepatic mRNA levels of genes related to fibrosis and inflammation from 22-week-old HFHS diet fed *Slc25a47*^{hep+/+} and *Slc25a47*^{hep-/-} mice (n=6-8). (C) Body weight measurement curve during HFHS diet feeding in *Slc25a47*^{hep+/+} (n=10) and *Slc25a47*^{hep-/-} (n=9) mice. HFHS diet started at week 1. (D, E, F) Blood glucose levels during oral glucose tolerance test (OGTT, D), insulin tolerance test (ITT, E) and pyruvate tolerance test (PTT, F) in 12-, 15-, 20-week-old *Slc25a47*^{hep+/+} and *Slc25a47*^{hep-/-} mice (n=8), respectively. Error bars represent mean \pm S.E.M. *p<0.05, **p<0.01, ***p<0.001 and ****p<0.0001, as determined by unpaired Student's t-test (B) or two-way ANOVA and Bonferroni post-hoc correction (C-F).

CHAPTER 3 Experimental procedures

Animal studies. C57BL/6 *Slc25a47*^{tm1a(EUCOMM)Hmgu} were obtained from the European Mouse Mutant Cell Repository (EuMMCR); in this model, a LoxP- and FRT-flanked neomycin resistance cassette is inserted upstream of exon 5 of *Slc25a47*. LoxP sites are inserted upstream of exon 5 and downstream of exon 6, thus flanking exons 5 and 6. *Slc25a47*^{tm1a(EUCOMM)Hmgu} were crossed with CMV-Flp mice (The Jackson Laboratories, JAX stock #012930) to remove the neomycin cassette leaving exons 5 and 6 floxed (*Slc25a47*^{tm1c(EUCOMM)Hmgu}, also referred to as *Slc25a47*^{flx/flx} mice). These 2 exons encode most of the protein (209/310 amino acids). *Slc25a47*^{tm1c(EUCOMM)Hmgu} mice were then crossed with an Alb-Cre recombinase mouse line (The Jackson Laboratories, JAX stock #003574) to generate *Slc25a47*^{hep-/-} mice harboring a hepatocyte-specific deletion of *Slc25a47* (Fig. 3.1A). *Slc25a47-Fgf21*^{hep-/-} animals were obtained by crossing *Slc25a47*^{hep-/-} with *Fgf21*^{flx/flx} mice (The Jackson Laboratories, JAX stock #022361; Fig. 3.1B). Mice were housed with ad libitum access to water and food (chow diet, Safe 150 or high-fat high-sucrose diet, Envigo TD.08811) and kept under a 12-hour dark/12-hour light cycle (7 pm/7 am) with a temperature of 22°C±1°C and a humidity of 60%±20%. Only male mice were used in this study. For fasting protocols, mice were fasted overnight (from 6 pm until 9am) before euthanizing. For fed experiments, food was removed at 7am (beginning of the light phase) and mice were euthanized 2 hours later (9 am). For fed electron microscopy (EM) analysis, food was not removed. For the high-fat high-sucrose (HFHS) diet study, 8-week-old mice were fed HFHS diet for 14 weeks.

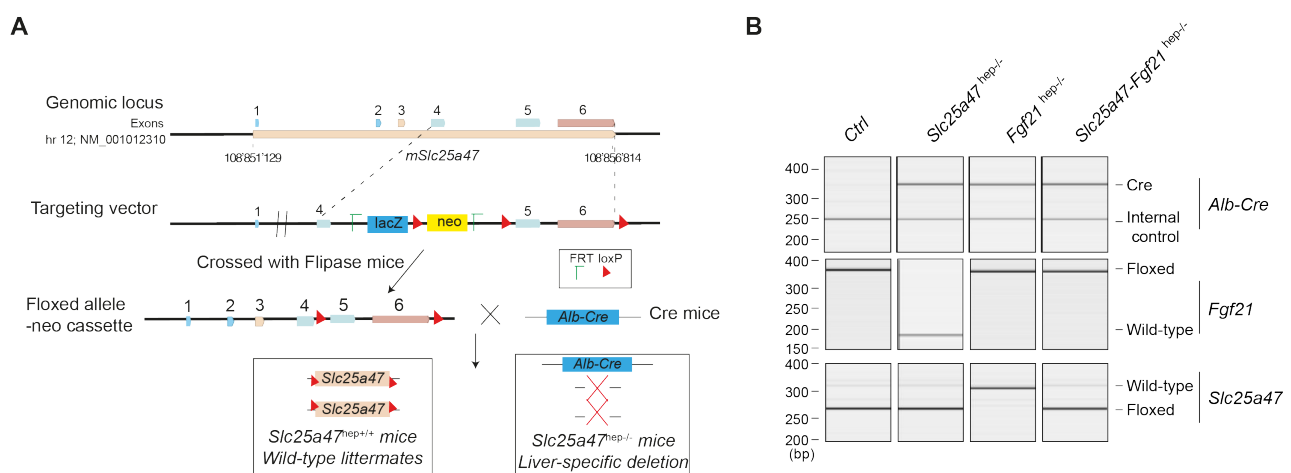


Figure 3.1. Animal models used in the study. (A) Gene targeting and conditional deletion of exons 5 and 6 of the *Slc25a47* gene to generate *Slc25a47*^{hep+/+} and *Slc25a47*^{hep-/-} mice. (B) PCR genotyping results for control (Ctrl), *Slc25a47*^{hep-/-}, *Fgf21*^{hep-/-} and *Slc25a47-Fgf21*^{hep-/-} mice. The PCR bands show the DNA amplification of Cre (320bp, internal control: 250bp), *Slc25a47* (Wild-type: 323bp, Floxed (loxP): 270bp), *Fgf21* (Wild-type: 179bp, loxP: 352bp).

Tolerance Tests

For Pyruvate Tolerance Test (PTT) and Insulin Tolerance Test (ITT), food was removed from 8 am until 2 pm (6-hour mild fasting) and mice were single-caged before oral gavage of 2g/Kg sodium pyruvate or to intraperitoneal injection of 0.5 IU insulin/Kg, respectively. For Oral Glucose Tolerance Test (OGTT), mice were fasted overnight as described above and single-caged before the

experiment; 2g/Kg of glucose were administered by oral gavage. In all the tolerance tests, glucose levels were measured with a glucometer at time: 0 (i.e before injection/gavage) and 15, 30, 45, 60, 90 minutes after injection/gavage. For OGTT, glycemia levels were also measured 120 minutes after gavage and additional blood was collected with a capillary tube at time 0, 15, 30, 60 minutes.

Indirect calorimetry

The indirect calorimetry experiment was performed using the Promethion System (Sable Systems International). Each mouse was individually placed in a cage with normal bedding and free access to food and water during the test, which lasted approximately 48 hours (24 hours of acclimation and 24 hours of measurement in normal feeding conditions). The system was set to have 12/12 hours light/dark cycle. Data were normalized on metabolic body mass (body weight, BW^{0.75}).

Food intake recording

Food intake was recorded at regular intervals (20 minutes) using a TSE PhenoMaster system (TSE Systems GmbH, Germany). Each mouse was placed individually in a cage with normal bedding and free access to food and water during the test, which lasted approximately 48 hours (24 hours of acclimation and 24 hours of measurement in normal feeding conditions). The system was set to have 12/12 hours light/dark cycle.

Study approval

All animal procedures were approved by the Swiss authorities (Canton of Vaud, animal protocols #3221, #3221.1) and performed in accordance with our institutional guidelines.

Cell culture. HeLa cell lines were obtained from American Type Culture Collection (ATCC) and cultured in DMEM with glucose (4.5 g/l), 10% fetal bovine serum (FBS), and penicillin-streptomycin (10 mg/ml) under standard conditions (37°C, 5% CO₂, humidified incubator).

For immunostaining, 30'000 cells/well were plated on a glass coverslip in a 12 well plate. After 24h cells were transfected using JetPEI® DNA transfection reagent (Polyplus transfection) with pCMV6-mSlc25a47mycDDK (Origene, MC212109) or pCMV6-empty-flag plasmids. 24h after, cells were fixed with 1X Formal-Fixx (Thermo Scientific) for 15min. After 15min of permeabilization with 0.5% Triton X-100, cells were blocked in Phosphate-Buffered Saline (PBS) supplemented with 3% FBS for 1h and immunostained overnight at 4 °C with anti-FLAG (Sigma, F7425) and anti-CoxIV (Abcam, ab33985) antibodies (1:250). The secondary antibody was coupled to an Alexa-488 or Alexa-568 fluorochrome (Thermo Scientific) and nuclei were stained with DAPI (Invitrogen, D1306). After washing in PBS, cell slides were mounted with DAKO mounting medium (DAKO, S3023) and analyzed with Zeiss LSM 700 confocal microscope (Carl Zeiss MicroImaging) equipped with a Plan-Apochromat 63x/1.40 oil immersion objective lens using 488nm and 555nm lasers.

Generation of Slc25a47 overexpressing cells

Endogenous overexpression of *Slc25a47* was obtained through CRISPR/dCas9-VP64 activation system¹⁶⁹. *Slc25a47* single-guide (sg)RNA sequence (GCCACACTCACATGCCCCACA) was

cloned into (lenti SAM v2, Addgene #75112) using BsmBI restriction sites and used for lentiviral particles production as follows: HEK293 T cells were grown in DMEM supplemented with 10% FBS and 1% penicillin/streptomycin (in 37°C, 5% CO₂, humidified incubator) and seeded at 50-80% confluency. Cells were then transfected with *Slc25a47* or Empty control (lenti SAM v2) together with psPAX2 (Addgene #12260) and pMD2.G (Addgene #12259) plasmids, using TransIT-X2 transfection reagent (Mirusbio, #MIR6000) following the manufacturer's instructions. The medium was changed 24 hours after transfection and the virus-containing supernatant was collected and filtered (0.45 µm filter, Millipore) 48-hours post-transfection. Target AML12 cells were infected in lentiviral particles-containing medium supplemented with hexadimethrine bromide (10 µg/ml Polybrene, Sigma #H9268). 48 hours post-infection, the medium was replaced and cells were selected by adding 2.5 µg/ml blasticidin (Sigma, #15205) in culture medium (DMEM/F12 Ham mixture with 10% FBS, 400 µl of gentamicin solution (50 mg/ml, Sigma), 100mM dexamethasone and insulin, transferrin and selenium supplement, Roche). Cells were kept in culture for one week and the surviving colonies were expanded and screened by qRT-PCR as described below.

Western Blotting. Liver tissues or mitochondrial pellets were homogenized with RIPA buffer (50mM Tris-HCl pH7.4, 150mM NaCl, 0.1% SDS, 0.5% sodium deoxycholate, 1% NP-40, 2 mM EDTA and 50 mM NaF) supplemented with 1 mM PMSF and protease and phosphatase inhibitor cocktails (Roche). Before running SDS-PAGE, whole liver protein lysates were boiled for 5 min 95°C. The following antibodies were used for immunoblotting: SLC25A47 (custom antibody manufactured by YenZym Antibodies LCC; Novus Biologicals, #NB100-57843), HSP70 (Abcam, #ab2787), VINCULIN (Abcam, #ab129002), HSP90 (BD Biosciences #610418), YME1L1 (Cusabio, #PA026267GA01HU), HSPA9 (Antibodies online, #ABIN361739), LONP1 (Sigma, #HPA002192) and GAPDH (Santa Cruz Biotechnology, #sc-365062).

Chromatin immunoprecipitation (ChIP)-PCR. ChIP analysis was performed as previously described¹⁷⁰. ChIPed DNA was purified using the PCR clean-up extraction kit (Macherey-Nagel), after which qPCR was performed as described below ("mRNA analysis"). ChIP data were normalized to the input (Fold differences = $2^{-(Ct-sample - Ct-input)}$). ChIP primer sequences (from¹⁷¹) were used to amplify the distal (*Fgf21_1*; -1060/-981) and the proximal (*Fgf21_2*; -168/-81) ATF4/5 binding sites within the mouse FGF21 promoter. Primers are listed in the Table 3.1. For ATF4 and ATF5 ChIP assays ATF4 (Cell Signaling #11815S) and ATF5 (Abcam #ab184923) antibodies were used. IgG antibody (Cell Signaling #2729) was used as negative control.

mRNA analysis. RNA was extracted from the tissues of the mice using TRIZOL (Invitrogen) and purified with the RNeasy MinElute cleanup kit (Qiagen) following the manufacturer's instructions. For quantitative reverse transcription (RT) qPCR, cDNA was generated using the QuantiTect® Reverse

Transcription Kit (Qiagen) and analyzed by RT-qPCR (SYBR Green chemistry) using a LightCycler® 480 Real-Time PCR System (Roche) and the primers listed in Table 3.1. qPCR results were presented relative to the mean of *36b4* or *B2m* ($\Delta\Delta C_t$ method).

Mitochondria isolation. Mitochondria were isolated from livers or cells as previously described¹⁷². Pellets of mitochondria were resuspended in RIPA buffer for Western Blot (refer to Western Blot section) or MiR05 for respiration assays (see below).

Mitochondria function assessment. Oxygen consumption rate (OCR) was assessed in freshly isolated intact mitochondria or whole liver homogenate in Respiration Medium (MiR 05-kit, Oroboros Instruments) by High-Resolution Respirometry (Oxygraph 2k, Oroboros Instruments) following manufactures' instructions. Whole liver lysates were normalized on 16S content or citrate synthase (CS) activity, while intact isolated mitochondria were normalized on (outer membrane) mitochondrial protein levels before performing the assay. For the respirometry assay compounds were added into the 2ml-chamber. Compounds used: Pyruvate (5mM, Sigma), Malate (2mM, Sigma), Glutamate (10mM, Sigma), Succinate (10mM, Sigma), Complex I-inhibitor Rotenone (0.1 μ M, Sigma) and ADP+Mg²⁺ (1.25mM, Sigma) for State₃ADP respiration; FCCP (titration of 1 μ l each from 1mM stock, Sigma) for maximal respiration, Oligomycin (2 μ g/ml Millipore) for uncoupled respiration. For fatty acid oxidation (FAO) assay, palmitoyl-carnitine (50 μ M, Sigma) and octanoyl-Carnitine (0.2mM, Tocris bioscience) were used in the presence of ADP. Malate was added to sustain fatty acid degradation avoiding acetyl-CoA accumulation. At the end of the protocol run, 2.5 μ M Antimycin A was used to assess non-mitochondrial respiration. All the represented values were Antimycin A subtracted. For *Slc25a47*-CRISPR/dcas9 cells, OCR was measured in XFe96 Microplates (Seahorse Bioscience). Briefly, cells were seeded at a density of 20 000 cells/well and further transfected for 24 hours with lentiIMPH v2 plasmid (Addgene #89308) using TransIT-X2 transfection reagent (as previously described). On the day of the assay, cells were washed once with complete medium and then incubated with Seahorse XF base medium (Agilent) pH 7.4 supplemented with 4.5g/l glucose and 2mM glutamine in 0% CO₂, 37°C incubator for 1 hour. The compounds used to determine OCR included Oligomycin (1 μ g/ml) and FCCP (5 μ M). The OCR values were normalized on protein concentration at the end of the experiment.

Citrate synthase activity was determined in a 96 well-plate using 50 μ g of liver protein by adding 2mg/ml DTNB (5,5-dithio-bis-2-nitrobenzoic acid, Sigma) and 15mM acetyl-CoA (Sigma). Background absorbance at 412nm was assessed using a spectrophotometer for 5 consecutive reads before addition of 10mM oxaloacetate (Sigma). The reaction was measured by following the absorbance (412nm) at 10s intervals 25 times. For mtDNA content, genomic DNA was extracted from liver tissues using NucleoSpin Tissue (Macherey-Nagel), and RT-qPCR was performed for the expression analysis of *16s* (mitochondrial) normalized to *Hk2* (nuclear gene). ATP levels were

measured using ATP assay kit (Abcam) or Cell Titer Glo (Promega) using ATP standard curve, according to manufacturer's instructions.

Lipid analysis, glycogen quantification and plasma parameters. Hepatic lipids were extracted according to the Bligh & Dyer protocol¹⁷³. Triglyceride and cholesterol contents in hepatic lipid fraction was quantified using enzymatic assays (Roche). For glycogen isolation, 10 mg of liver tissue were homogenized in cold distilled water. The homogenate was divided into two tubes of equal volumes: one tube was boiled for 5min and then centrifuged for 5 min at 13'000g, RT. The supernatant was collected and quantified (diluted 1:50) using the Glycogen assay kit (Merck). The second tube was used for protein quantification (BioRad, #5000116). Total glycogen was normalized on total protein levels. ASAT and ALAT plasma parameters were measured on 2 times diluted samples (1:1 ratio of plasma to diluent) using Dimension®Xpand Plus (Siemens Healthcare Diagnostics AG, Dudingen, Switzerland). The biochemical tests were performed using Transaminase ASAT (Siemens Healthcare, DF41A), transaminase ALAT (Siemens Healthcare, DF143) kits according to manufacturer's instructions. Circulating lactate (1:100 plasma dilution) was measured using Lactate Glo (Promega), following manufacturer's instructions. Plasma FGF21, ADM2 and GDF15 levels were measured, according to manufacturer's instruction, with RAT/MOUSE FGF21 Elisa kit (Millipore), Mouse ADM2 Elisa kit (Cusabio) and Quantikine ELISA Mouse/Rat GDF15 (R&D Systems), respectively.

Immunohistochemistry, electron microscopy analysis and RNAscope. Liver tissue was fixed overnight in phosphate-buffered 10% formalin and embedded in paraffin, sectioned in 4 µm and stained for hematoxylin/eosin (H&E), Masson's trichrome and Sirius red. Liver pieces were frozen while embedded in optimum cutting temperature (OCT) and later cut into 8-µm-thick serial cryosections for oil red O staining to visualize neutral lipids. For immunohistochemistry, detection of leukocytes (rat α-CD45, Thermo Fisher #14045182, diluted 1:200) and macrophages (rat α-F4/80, Thermo Fisher #MA191124, diluted 1:50) was performed using the fully automated Ventana Discovery ULTRA (Roche Diagnostics, Rotkreuz, Switzerland). All steps were performed on the equipment with Ventana solutions. Briefly, dewaxed and rehydrated paraffin sections were not pretreated for F4/80 or pretreated with heat using standard condition (40 minutes) CC1 solution for CD45. The primary antibodies were incubated 1 hour at 37°C. After incubation with rat Immpress HRP (Ready to use, Vector laboratories Laboratories), chromogenic revelation was performed with ChromoMap DAB kit (Roche Diagnostics, Rotkreuz, Switzerland). Sections were counterstained with Harris hematoxylin and permanently mounted. For electron microscopy (EM), adult mice (8-week-old, males) were euthanized with an overdose of inhalation anesthetic (isoflurane) and perfused, via the heart, with a solution of 2.5 % glutaraldehyde and 2.0 % paraformaldehyde in 0.1M phosphate buffer (pH 7.4). One hour after the perfusion, the livers were removed, and sectioned at a thickness

of 80 µm using a vibratome (VT1200, Leica Microsystems). Liver slices were then post-fixed in potassium ferrocyanide (1.5%) and osmium (2%), then stained with thiocarbohydrazide (1%) followed by osmium tetroxide (2%). This was followed by further staining with uranyl acetate (1%) overnight, washing in distilled water at 50°C, and then with lead aspartate (pH 5.0), at the same temperature. The sections were finally dehydrated in increasing concentrations of alcohol and then embedded in Durcupan resin and hardened at 65 °C for 24 h between glass slides. For transmission EM (TEM), regions of interest were cut away from the rest of the slices, and mounted on a blank resin block. Sections were cut, using an ultramicrotome, and imaged in a transmission electron microscope operating at 80 kV (Tecnai Spirit, FEI Company). Serial imaging of entire cells was carried out using block face scanning EM. Regions of interest were trimmed from the rest of the section using a razor blade, glued to an aluminium stub and mounted inside a scanning electron microscope (Zeiss Merlin, Zeiss NTS). Serial sections were cut from the face using an ultramicrotome mounted inside the microscope (Gatan, 3View) and the block face imaged after every cut using a beam voltage of 1.7 kV and pixel size of 6 nm with a dwell time of 1 microsecond. Series of images were aligned in the FIJI imaging software (www.fiji.sc). The analysis of lipid droplets was made on single TEM images. The analysis of density of lipid droplets was carried out using the TrakEM2 plugin operating in the FIJI software.

RNAscope Multiplex Fluorescent V2 assay (Bio-technique, #323100) was performed according to manufacturer's protocol on 4 µm paraffin sections, hybridized with the probes Mm-Slc25a47-C1 (Bio-technique, #558371), Mm-Ppib-C1 (Bio-technique, #313911) as positive control and DapB-C1 (Bio-technique, #310043) as negative control at 40°C for 2 hours and revealed with TSA Opal570 (Akoya Biosciences, # FP1488001KT, 1:1500). Tissues were counterstained with DAPI and mounted with FluoromountG (ThermoFisher).

Bioinformatic analysis. *Mus musculus* Slc25 family of transporters expression profiles were obtained from¹⁷⁴ (ArrayExpress, E-MTAB-6081). All heatmaps were generated using Morpheus (<https://software.broadinstitute.org/morpheus>). G-MAD was performed as described¹⁵⁹. *Sc25a47* expression in different *Mus musculus* tissues was obtained from BioGPS (GEO #GSE10246). For transcriptome analysis, RNA from mouse livers (*Slc25a47*^{hep+/+} n=4, *Slc25a47*^{hep-/-} n=4) was isolated as described in the dedicated section. RNA sequencing (RNA-seq) was performed using single end 126 cycles on a HiSeq 2500, in high output mode, with v4 kits from Illumina. FastQC was used to verify the quality of the mapping¹⁷⁵. No low-quality reads were present and no trimming was needed. Alignment was performed against mouse genome (CRCm38 mm10 primary assembly and Ensembl release 95 annotation) using STAR¹⁷⁶ (version 2.73a). The obtained STAR gene-counts for each alignment were analyzed for differentially expressed genes using the R package edgeR (version 3.24.3) using a generalized-linear model. A threshold of 0.5 or 1 log2 fold change and Benjamini-Hochberg adjusted P value larger than 0.05 were considered when identifying the differentially

expressed genes. Gene set enrichment analysis (GSEA) was performed using the clusterProfiler R package (version 3.10.1). In particular, the gene sets belonging to KEGG database were obtained from msigdb R package (version 7.2.1). Additionally, we included one custom gene set ("Mitochondrial Stress Response"), based on previously published OMICs data⁶³. Genes were ranked based on the fold change between *Slc25a47*^{hep-/-} and *Slc25a47*^{hep+/+}. The gene sets with absolute normalized enrichment score (NES) more than 1 and Qvalue (FDR) less than 0.05 were considered as significantly enriched. For the transcription factor (TF) motifs analysis, the top TFs of *Fgf21* were obtained using the promoter sequence of *Fgf21* ± 2kb region around the transcription starting site (TSS); then, TF motifs were extracted from the MotifDb R package (version 1.36.0). Based on these datasets, we performed the enrichment analysis of TF motifs by R PWMenrich package (version 4.30.0). The TF motifs with a P value lower than 0.05 were selected. For correlation analysis between TFs and *Fgf21*, we calculated the Pearson correlation coefficient (using R) on the gene expression (RNAseq data) of the given genes, in both *Slc25a47*^{hep-/-} and *Slc25a47*^{hep+/+} mice under fed and fasted conditions. The cell type enrichment analysis was calculated by clusterProfiler R package (version 3.10.1)¹¹. The gene makers for 29 types of cell in liver were obtained from two single cell RNA-seq analysis studies^{177,178}. Genes were ranked based on the fold change in each comparison, and then applied to the cell type enrichment analysis.

The RNAseq data discussed in this publication have been deposited in NCBI's Gene Expression Omnibus¹⁷⁹ and are accessible through GEO Series accession number GSE195479 (<https://www.ncbi.nlm.nih.gov/geo/query/acc.cgi?acc=GSE195479>).

All the plots were generated using ggplot2. For scRNA-seq analysis, data were obtained from Tabula Muris¹⁸⁰. The liver droplet dataset was downloaded and analyzed according to the instructions in the Tabula Muris vignettes Github repository (<https://github.com/czbiohub/tabula-muris-vignettes>) and visualized using Seurat package¹⁸¹ (v4.0.4).

Homology modeling. The mitochondrial ADP/ATP carrier (AAC or SLC25A4, PDB ID 1OKC) was the first SLC25 structurally characterized. The HHPred server (doi: 10.1093/nar/gki408) identified this carrier as the best hit for performing homology modeling of the SLC25A47 protein, with E-values of 4.3×10^{-55} . Using the sequence alignment provided by the HHPred server, structural models for the SLC25A47 protein were created with the Modeller program, version 9.13 (doi: 10.1002/0471250953.bi0506s15). 100 models were created for each conformation (template), using the default optimization and refinement protocol, and for each conformation, the model with the lowest DOPE score was selected.

Statistics. Data were represented and analyzed using GraphPad Prism (v9.2.0). Plots are expressed as means ± S.E.M. Comparison of differences between two groups was assessed using unpaired two-tailed Student's *t*-tests. Multiple group comparisons were assessed by one-way or two-

way ANOVA with Bonferroni *posthoc* correction or Tukey's multiple comparison test. Differences below $p < 0.05$ were considered statistically significant (* $p < 0.05$, ** $p < 0.01$, *** $p < 0.001$, **** $p < 0.0001$). The statistical methods used and the corresponding p values for the data shown in each figure panel are included in the figure legends.

Illustrations. As specified in figure legends, some of the illustrations presented in this thesis were created with BioRender ([Biorender.com](https://biorender.com)).

Table 3.1. List of Primers

Gene	Forward (5' to 3' sequence)	Reverse (5' to 3' sequence)
36b4	AGATTCGGGATATGCTGTTGG	AAAGCCTGGAAGAAGGAGGTC
B2m	TTCTGGTGCTTGTCTCACTG	TATGTTCGGCTTCCCATTCT
Slc25a47	GCCACTGCACTGTTTAGTCAC	ACTCGCAGAGCATAGCATAGG
Hspa9	AATGAGAGCGCTCCTTGCTG	CTGTTCCCCAGTGCCAGAAC
Hspd1	TCTTCAGGTTGTGGCAGTCA	CCCCTCTTCTCCAAACACTG
Hspa1a	AGCAGCGTGAGGAGTACCAG	CGGTAGGGCTAGAGAAACAGG
Yme1l1	CGGTAGACCCTGTCCAGATG	TTCAACCACTTCCTGTAACCTTG
Lonp1	ATGACCGTCCCGGATGTGT	CCTCCACGATCTTGATAAAGCG
Ucp1	GGCCCTTGTAACAACAAAATAC	GGCAACAAGAGCTGACAGTAAAT
Cidea	TGCTCTTCTGTATCGCCCAGT	GCCGTGTTAAGGAATCTGCTG
Dio2	CAGTGTGGTGCACGTCTCCAATC	GGAAGGAATCTTAGCTGGGG
Cox7a1	GCTCTGGTCCGGTCTTTTAGC	GTAAGGGAGGTCATTGTCTGG
Ccl2	CAGATGCAGTTAACGCCCA	TGAGCTTGGTGACAAAACTACAG
Ccl3	CCAGCCAGGTGTCATTTTCCTGA	GCTCAAGCCCCTGCTCTAC
Mmp3	ACATGGAGACTTTGTCCCTTTTG	TTGGCTGAGTGGTAGAGTCCC
Mmp13	CTTCTTCTTGTTGAGCTGGACTC	CTGTGGAGGTCACTGTAGACT
Col1a1	TAAGGGTCCCCAATGGTGAGA	GGGTCCCTCGACTCCTACAT
Reln	GCTTGCGCATGCTAGTAACAC	CCAGTCTCATGAAGAACTGCAC
Tnfa	CCAAGGCGCCACATCTCCCT	GCTTTCTGTGCTCATGGTGT
Tgfb1	CCACCTGCAAGACCATCGAC	CTGGCGAGCCTTAGTTTGGAC
F4/80	AGATGGAACCAAACCTCCAGG	TGCTCTTTTCAAACATGTGG
Cd45	ATGGTCCTCTGAATAAAGCCCA	TCAGCACTATTGGTAGGCTCC
Fgf21_1 (Fgf21 - 1060/-981) ChIP	GCTTAGCATTCGGGCCTTG	GCAGGACGCTGTCTGGTG

Fgf21_2 (<i>Fgf21</i> - 168/-81) - ChIP	TTCAGACCCCTGTTGGAAAG	CACACTTGGCAGGAACCTGAAT
16S (gDNA)	CCGCAAGGGAAAGATGAAAGAC	TCGTTTGGTTTCGGGGTTTC
<i>Hk2</i> (gDNA)	GCCAGCCTCTCCTGATTTTAGTGT	GGGAACACAAAAGACCTCTTCTGG
<i>Cre</i> (gDNA)	GAACCTGATGGACATGTTTCAGG	AGTGCGTTCGAACGCTAGAGCCTGT
Fgf21 (gDNA)	GAAACAAAGCTTCAAATAGGG	AGTAGGGGTCAGACGTGGTG
<i>Slc25a47</i> (gDNA)- Wild type	CCGTGAAACCCTGCAGAGCC	CACCACAGATTGTTCTGTGAAGA
<i>Slc25a47</i> (gDNA)- loxP	TACGAAGTTATGGTCTGAGCTCGC	CACCACAGATTGTTCTGTGAAGA

CHAPTER 4 Discussion and perspectives

4.1. Discussion

The work presented in this thesis intended to elucidate the role of SLC25A47 in hepatic metabolism. This thesis demonstrates that SLC25A47 is abundantly and uniquely expressed in hepatocytes, being the second most expressed SLC25 member in the liver. This finding highlights the importance of SLC25A47 in the context of liver physiology and suggests that this carrier could be involved in hepatocyte-specific mitochondrial function. To study how SLC25A47 contributes to hepatic metabolism, we investigated the loss of this carrier by generating novel hepatocyte-specific LOF murine lines (*Slc25a47*^{hep-/-}, *Slc25a47*^{hep+/-} mice). My work significantly helped to characterize the role of SLC25A47 in hepatic physiology and showed that the loss of this orphan carrier is detrimental for mitochondrial homeostasis. *Slc25a47* knockout livers suffered from energy deficiencies, caused by defective oxidative phosphorylation. Indeed, *Slc25a47*-deficient mitochondria showed a global respiration impairment, exemplified by their inability to oxidize both TCA cycle derivatives and fatty-acyl substrates. These OXPHOS impairments led to mitochondrial dysfunction, causing the mitochondria to be metabolically inflexible and unable to further switch from glucose metabolism in fed state to fatty acid oxidation in the fasted state.

The chronic energy deficit also led to impaired gluconeogenesis and faster depletion of the glycogen stores in the fed state. Overall, these phenotypes underlie the observed hypoglycemia, even after mild fasting or HFHS feeding. Moreover, *Slc25a47*^{hep-/-} mice suffered from liver damage preponderantly in the fasted state suggesting that *Slc25a47*-deficient hepatocytes fail to cope with the additional metabolic pressure induced by fasting. While our study used a design based on a liver-specific ablation of *Slc25a47* which maximizes the negative effects on hepatic homeostasis, a milder inhibition of SLC25A47 could prove interesting from a therapeutic perspective, as demonstrated by our preliminary analysis of heterozygous mice (Figure 2.13). Our data show that one of the main consequences of SLC25A47 downregulation is an inhibition of the hepatic ETC, which results in impaired gluconeogenesis. This way of action is reminiscent of the mechanism of metformin, the most frequently prescribed antidiabetic treatment, which reduces hepatic gluconeogenesis through moderate inhibition of complex I¹⁸². Theoretically, a mild inhibition of SLC25A47 could hamper the ETC specifically in hepatocytes and lower glycemia by blunting *de novo* glucose production.

Our data show that SLC25A47 is essential to maintain hepatic mitochondrial homeostasis and proper ETC function, as its loss results in the activation of a profound and persistent MSR. Mitochondrial stress induces mitochondrial quality control mechanisms that are essential to maintain mitochondrial function. Retrograde signals from the mitochondria to the nucleus have been well-documented in multiple species⁵⁴ and involve the induction of TFs including ATF4^{57,183,184}, ATF5⁶⁴, CHOP^{185,186}, and C/EBP β ^{185,186}. Alongside these cell-autonomous effectors, non-cell-autonomous factors are also secreted enabling the MSR to rewire organismal metabolic homeostasis^{111,187–189}.

Accordingly, in this study, we demonstrated that FGF21 is a key hepatic mitokine that modulates systemic energy metabolism in *Slc25a47*^{hep-/-} mice. Persistent activation of the ATF family of transcription factors most likely contributes to the striking induction of plasma FGF21 levels in *Slc25a47*^{hep-/-} mice⁸⁹. We showed that the induction of FGF21 mediates a profound hypermetabolic state in our mouse model driving the systemic, but not the hepatic, phenotypes, such as increased scWAT beiging, energy expenditure, hyperphagia, and blunted growth.

The MSR is normally activated by mitonuclear protein imbalance, such as seen with defects in mitochondrial DNA replication^{190,191}, in the ETC^{57,163}, in mitoribosomal translation^{161,162} or upon mitochondrial biogenesis^{192,193}. Here we linked the activation of the MSR with the loss of a mitochondrial carrier. Involvement of mitochondrial carriers in mitochondrial stress, however, is not unprecedented as an early study attempting to define the MSR in *Arabidopsis thaliana* already reported that the Slc25 family was over-represented amongst stress-responsive genes¹⁹⁴. While this study suggested that mitochondrial stress resolution involves a rewiring of metabolite trafficking across mitochondrial membranes¹⁹⁴, we extend this finding by suggesting that the depletion, or the accumulation, of given metabolites, can be the trigger of mitochondrial stress. In fact, the research carried out in this thesis suggests that SLC25A47 controls the levels of a mitochondrial metabolite, the nature of which is currently unknown and requires further investigation given its potential impact on hepatocyte mitochondrial function, liver fibrosis and organismal health.

Finally, it is important to emphasize that, while SLC25A47 LOF improves the metabolic profile of mice on an obesogenic, diabetogenic diet, this is achieved at the expense of liver health and integrity as exemplified by the fibrotic phenotype induced progressively upon ageing or acutely under the metabolic pressure of an HFHS diet. Fibrosis is a common pathological feature of most end-stage organ diseases and growing evidence indicates that mitochondrial dysfunction contributes to the development and progression of fibrosis in a number of organs (reviewed in¹⁹⁵). In the liver, fibrosis is driven by NASH, and drives the evolution of NASH to cirrhosis and in some cases to HCC. Our observation features SLC25A47 and the putative solute it carries, as potential new therapeutic targets in the fight against advanced stages of metabolic disorders.

4.2. Perspectives

4.2.1 SLC25A47 structure

SLC25A47 is an orphan SLC25 member, whose transported solute is still unknown. Despite the low sequence similarity with its closed homologs, SLC25A47 phylogenetically clusters together with known amino acids carriers (SLC25A15, SLC25A2, SLC25A20, SLC25A29), suggesting that its function could be related to amino acid metabolism.

To address this point, we performed homology modeling between SLC25A47 and SLC25A4¹⁵⁷ and analyzed SLC25A47 structure to predict possible transported molecules. The analysis showed a positively charged core that putatively allows the transport of negatively charged solutes. Nevertheless, this model is biased towards SLC25A4 structure and transport (ATP/ADP), rendering difficult to infer any metabolite specificity for SLC25A47.

To date, the most successful strategy employed to identify substrate specificity of solute carriers with unknown function, consists in reconstitution of recombinant protein into liposomes followed by radioactive transport assays, herein referred to as the “expression–purification-reconstitution-assay” (EPRA) method¹⁹⁶. Unfortunately, the reconstitution of SLC25A47 in liposomes proved to be technically challenging due to the high content of cysteine residues in this transporter (4.5% compared to the ~2.2% of average cysteine content in proteins¹⁹⁷), resulting in disulfide bond formation and compromised native protein folding. In this context, further investigations are currently ongoing to solve the issue and determine the nature of the carried metabolite.

Moreover, additional efforts will be needed to investigate the structure of the carrier and find amino acid sites of possible regulation. Indeed, our preliminary structural data showed that SLC25A47 possess a unique mitochondrial loop, which carries a putative PKA phosphorylation site. Further analysis will focus on demonstrating that this residue is indeed phosphorylated *in vivo*, and will try to discern its physiological role.

Of note, *Slc25a47*^{hep-/-} mice phenotype was strongly exacerbated by fasting condition, probably due to the reliance of hepatocytes to their mitochondria in the fasted state. We could, therefore, speculate that SLC25A47 is regulated by fasting-induced stimuli and hormones. Indeed, fasting increases the secretion of pancreatic glucagon, which in turns promotes a signaling cascade resulting in increased cAMP production. cAMP activates PKA, resulting in the phosphorylation of the TF cAMP response element-binding protein (CREB) and the activation of genes involved in the fasted state metabolism (like peroxisome proliferator-activated receptor γ coactivator-1 (PGC1 α), phosphoenolpyruvate carboxykinase (PEPCK) and glucose-6-phosphatase (G6PC)). In this context, and given the presence of putative PKA sites on SLC25A47, we hypothesize that the fasting response might control the carrier function at the post-translational level, and future efforts will attempt to demonstrate this link.

4.2.2 SLC25A47 function

Inhibition of OXPHOS is proven to be beneficial for glucose homeostasis^{69,198,199}, by boosting glycolysis and reducing hepatic gluconeogenesis²⁰⁰. Accordingly, our preliminary studies in *Slc25a47*^{hep+/-} mice showed that a partial reduction in hepatocyte-specific *Slc25a47* does not cause adverse systemic effects, but reduces hepatic *de novo* glucose production and increases circulating lactate levels. Similar to the well-known action of Metformin, *Slc25a47*^{hep+/-} mice display impaired

OXPHOS respiration accompanied by reduced hepatic ATP content²⁰¹. These observations pose SLC25A47 at the center of hepatic metabolism and could open to possible new therapeutic strategies to treat metabolic diseases.

Interestingly, *Slc25a47*^{hep+/-} mice showed a mild induction of the prototypical UPR^{mt} genes. Boosting mitochondrial quality control mechanisms has already been proven beneficial in a multitude of organs, including liver^{92,193,202,203}. Indeed, eliciting the UPR^{mt} pathways ameliorates NAFLD in Western diet fed mice²⁰⁴ and protects the liver upon acute injury²⁰⁵. Given these preliminary positive results, future research should determine the potential therapeutic benefit of SLC25A47 inhibition, by taking advantage of *in vivo* acute deletion models, for example by transducing *Slc25a47*^{lox/lox} mice with AAV8-Cre particles or using Tamoxifen inducible Cre lines.

However, SLC25A47 downregulation needs to be carefully assessed. SLC25A47 was firstly discovered as the hepatocellular carcinoma downregulated carrier protein HDCMP, but despite this evocative nomenclature, the link between this unique mitochondrial carrier and the progression to hepatic carcinogenesis has never been studied. To date, the loss of very few members of the SLC25 family is reported to be directly linked to cancer development²⁰⁶. Importantly, the reprogramming of cellular metabolism is a key feature of tumorigenesis and mitochondrial carriers play a preponderant role in controlling tumor cells nutrients²⁰⁶. In particular, cancer cells display increased glucose consumption, which is metabolized by aerobic glycolysis rather than OXPHOS. This phenomenon, named Warburg effect²⁰⁷, causes the tumor cells to accumulate lactate, which in turns acidifies the extracellular microenvironment favoring metastasis and immunosuppression. The loss of SLC25A47 leads to similar metabolic rewiring, suggesting that its physiological role is crucial for metabolic pathways that are normally futile in cancer cells. In this frame, future studies are warranted to establish the link between HCC and *Slc25a47* LOF, evaluating spontaneous tumor formation in aged *Slc25a47*^{hep-/-} mice. Accordingly, our data demonstrate that chronic loss of SLC25A7 predisposes to liver fibrosis. Given the importance of fibrosis in the evolution of hepatic diseases (from NAFLD to HCC), our data support SLC25A47 as a potential target for therapeutic intervention, whose application remains to be tested, but is an example of how a better understanding of mitochondrial carriers could be leveraged to treat metabolic disorders¹³⁸.

To conclude, my work on SLC25A47 helped to fill a gap in the current field of SLC25 carriers. Although our knowledge about this novel mitochondrial carrier is still incomplete, I believe that my thesis lays the foundations for exciting new future research.

Curriculum Vitae

Nadia Bresciani

nadia.bresciani.91@gmail.com; +41779179519

Italian

Education

- 2018-2022** **PhD in Molecular Life Sciences**
Ecole polytechnique fédérale de Lausanne (EPFL), Switzerland
- 2013-2015** **Master of Science in Molecular Biology of the Cell**
Università degli Studi di Milano, Italy
- 2010-2013** **Bachelor in Biological Sciences**
Università degli Studi di Milano, Italy

Research Experience

- 2018-2022** Laboratory of Metabolic Signaling, EPFL, Switzerland
PhD Student under the supervision of Prof. Kristina Schoonjans
- 2014-2017** Emerging Bacterial Pathogen Unit, WHO Supranational Reference Laboratory for Tuberculosis, San Raffaele Hospital, Italy
Research fellow under the supervision of Dr. Daniela Cirillo

Publications

Bresciani N*, Demagny H*, Lemos V, Pontanari F, Li X, Sun Y, Li H, Perino A, Auwerx J, Schoonjans K. The *Slc25a47* locus is a novel determinant of hepatic mitochondrial function. *Journal of Hepatology*, 2022 (doi: 10.1016/j.jhep.2022.05.040).

Perino A, Velázquez LA, **Bresciani N**, Sun Y, Huang Q, Fénelon VS, Castellanos A, Zizzari P, Bruschetta G, Jin S, Baleisye A, Gioiello A, Pellicciari R, Ivanisevic J, Schneider BL, Diano S, Cota D&Schoonjans K. Central anorexigenic actions of bile acids are mediated by TGR5. *Nature Metabolism*, 2021 (doi: 10.1038/s42255-021-00398-4). Contribution: Nadia Bresciani performed experiments and analyzed the data.

Sun Y*, Demagny H*, Jalil A, **Bresciani N**, Yildiz E, Korbelius M, Perino A, Schoonjans K. Asparagine protects pericentral hepatocytes during acute liver injury. (in preparation)

*Equal contribution

Scientific meetings

2nd *Metabolism in health and disease conference*, Cancun (ME), 2022 (poster presentation)

LIMNA conferences, Lausanne (CH), 2018-2019

Keystone Symposium, New Developments in our basic understanding of Tuberculosis, Vancouver (CA), 2017 (poster presentation)

EMBO conference Tuberculosis 2016, Paris (FR), 2016 (poster presentation)
37th Annual Congress of the European Society of Mycobacteriology, Catania (IT), 2016 (poster presentation and organizer)

Laboratory Skills

In vivo expertise: Mice handling, metabolic phenotyping, treatment (intraperitoneal injection), blood sampling, necropsy. Completed the Introductory course in Laboratory Animal Science (FELASA).

In vitro expertise: Human and mouse primary cell culture; human, mouse & bacterial cell culture; human PBMC isolation.

Molecular & cellular biology techniques: RT-qPCR; Western Blot; DNA electrophoresis; IP; imaging (confocal microscope); ELISA; immunocytochemistry and immunohistochemistry; cell/bacteria transfection/transformation, CRISPR-dCas9 technique; respiration assays (Oroboros, Seahorse); bacterial CFU counting and growth curves.

Data analysis: Graph Pad, ImageJ, Fiji, R.

IT & Graphic: IT/OT systems, Adobe Illustrator, Word, Excel, Powerpoint.

References

1. Trefts, E., Gannon, M. & Wasserman, D. H. The liver. *Curr. Biol.* **27**, R1147–R1151 (2017).
2. Sasse, D., Spornitz, U. M. & Piotr Maly, I. Liver Architecture. *Enzyme* **46**, 8–32 (1992).
3. Droin, C. *et al.* Space-time logic of liver gene expression at sub-lobular scale. *Nat. Metab.* **3**, 43–58 (2021).
4. Halpern, K. B. *et al.* Single-cell spatial reconstruction reveals global division of labour in the mammalian liver. *Nature* **542**, 352–356 (2017).
5. Jungermann, K. & Keitzmann, T. Zonation of Parenchymal and Nonparenchymal Metabolism in Liver. *Annu. Rev. Nutr.* **16**, 179–203 (1996).
6. Birchmeier, W. Orchestrating Wnt signalling for metabolic liver zonation. *Nat. Cell Biol.* **18**, 463–465 (2016).
7. D'Mello, C. & Swain, M. G. Liver-brain inflammation axis. *AJP Gastrointest. Liver Physiol.* **301**, G749–G761 (2011).
8. Rui, L. Energy Metabolism in the Liver. in *Comprehensive Physiology* **4**, 177–197 (John Wiley & Sons, Inc., 2014).
9. Kanungo, S., Wells, K., Tribett, T. & El-Gharbawy, A. Glycogen metabolism and glycogen storage disorders. *Ann. Transl. Med.* **6**, 474–474 (2018).
10. Petersen, M. C., Vatner, D. F. & Shulman, G. I. Regulation of hepatic glucose metabolism in health and disease. *Nat. Rev. Endocrinol.* **13**, 572–587 (2017).
11. Sanders, F. W. B. & Griffin, J. L. De novo lipogenesis in the liver in health and disease: More than just a shunting yard for glucose. *Biol. Rev.* **91**, 452–468 (2016).
12. Eaton, S. Control of mitochondrial β -oxidation flux. *Prog. Lipid Res.* **41**, 197–239 (2002).
13. Postic, C. & Girard, J. Contribution of de novo fatty acid synthesis to hepatic steatosis and insulin resistance: Lessons from genetically engineered mice. *J. Clin. Invest.* **118**, 829–838 (2008).
14. Demange, M. Sources of fatty acids stored in liver and secreted via lipoproteins in patients with nonalcoholic fatty liver disease. **115**, 1343–1351 (2005).
15. Perino, A., Demagny, H., Velazquez-Villegas, L. & Schoonjans, K. Molecular physiology of bile acid signaling in health, disease, and aging. *Physiol. Rev.* **101**, 683–731 (2021).
16. Houten, S. M., Watanabe, M. & Auwerx, J. Endocrine functions of bile acids. *EMBO J.* **25**, 1419–1425 (2006).
17. Bigot, A., Tchan, M. C., Thoreau, B., Blasco, H. & Maillot, F. Liver involvement in urea cycle disorders: a review of the literature. *J. Inherit. Metab. Dis.* **40**, 757–769 (2017).
18. Blanco, A. & Blanco, G. Amino Acid Metabolism. in *Medical Biochemistry* 367–399 (Elsevier, 2017). doi:10.1016/B978-0-12-803550-4.00016-1
19. Morris, S. M. Regulation of enzymes of the urea cycle and arginine metabolism. *Annu. Rev. Nutr.* **22**, 87–105 (2002).
20. Matsumoto, S. *et al.* Urea cycle disorders—update. *J. Hum. Genet.* **64**, 833–847 (2019).
21. Blanco, A. & Blanco, G. Proteins. in *Medical Biochemistry* 21–71 (Elsevier, 2017). doi:10.1016/B978-0-12-803550-4.00003-3
22. Galgani, J. E., Moro, C. & Ravussin, E. Metabolic flexibility and insulin resistance. *Am. J. Physiol. - Endocrinol. Metab.* **295**, 1009–1017 (2008).
23. Kelley, D. E. & Mandarino, L. J. Fuel selection in human skeletal muscle in insulin resistance: A reexamination. *Diabetes* **49**, 677–683 (2000).
24. Mansouri, A., Gattoliat, C. H. & Asselah, T. Mitochondrial Dysfunction and Signaling in Chronic Liver Diseases. *Gastroenterology* **155**, 629–647 (2018).
25. Middleton, P. & Vergis, N. Mitochondrial dysfunction and liver disease: role, relevance, and potential for therapeutic modulation. *Therap. Adv. Gastroenterol.* **14**, 17562848211031394 (2021).
26. Prasun, P., Ginevic, I. & Oishi, K. Mitochondrial dysfunction in nonalcoholic fatty liver disease and alcohol related liver disease. *Transl. Gastroenterol. Hepatol.* **6**, 4–4 (2021).
27. Zhang, I. W., López-Vicario, C., Duran-Güell, M. & Clària, J. Mitochondrial Dysfunction in Advanced Liver Disease: Emerging Concepts. *Front. Mol. Biosci.* **8**, (2021).
28. Degli Esposti, D. *et al.* Mitochondrial Roles and Cytoprotection in Chronic Liver Injury.

- Biochem. Res. Int.* **2012**, 1–16 (2012).
29. Sunny, N. E., Bril, F. & Cusi, K. Mitochondrial Adaptation in Nonalcoholic Fatty Liver Disease: Novel Mechanisms and Treatment Strategies. *Trends Endocrinol. Metab.* **28**, 250–260 (2017).
 30. Koliaki, C. *et al.* Adaptation of Hepatic Mitochondrial Function in Humans with Non-Alcoholic Fatty Liver Is Lost in Steatohepatitis. *Cell Metab.* **21**, 739–746 (2015).
 31. Patterson, R. E. *et al.* Lipotoxicity in steatohepatitis occurs despite an increase in tricarboxylic acid cycle activity. *Am. J. Physiol. Metab.* **310**, E484–E494 (2016).
 32. Satapati, S. *et al.* Elevated TCA cycle function in the pathology of diet-induced hepatic insulin resistance and fatty liver. *J. Lipid Res.* **53**, 1080–1092 (2012).
 33. Yamashina, S., Sato, N., Kon, K., Ikejima, K. & Watanabe, S. Role of mitochondria in liver pathophysiology. *Drug Discov. Today Dis. Mech.* **6**, e25–e30 (2009).
 34. Dyall, S. D., Brown, M. T. & Johnson, P. J. Ancient Invasions: From Endosymbionts to Organelles. *Science (80-.)*. **304**, 253–257 (2004).
 35. Boguszewska, K., Szewczuk, M., Kaźmierczak-Barańska, J. & Karwowski, B. T. The Similarities between Human Mitochondria and Bacteria in the Context of Structure, Genome, and Base Excision Repair System. *Molecules* **25**, 2857 (2020).
 36. Mae-Wan Ho, P. Cancer a Redox Disease. *ACNEM J.* **32**, (2013).
 37. Yan, Duanmu, Zeng, Liu & Song. Mitochondrial DNA: Distribution, Mutations, and Elimination. *Cells* **8**, 379 (2019).
 38. Friedman, J. R. & Nunnari, J. Mitochondrial form and function. *Nature* **505**, 335–43 (2014).
 39. Sato, M. & Sato, K. Degradation of Paternal Mitochondria by Fertilization-Triggered Autophagy in *C. elegans* Embryos. *Science (80-.)*. **334**, 1141–1144 (2011).
 40. Luo, S. *et al.* Biparental inheritance of mitochondrial DNA in humans. *Proc. Natl. Acad. Sci. U. S. A.* **115**, 13039–13044 (2018).
 41. D'Souza, A. R. & Minczuk, M. Mitochondrial transcription and translation: overview. *Essays Biochem.* **62**, 309–320 (2018).
 42. Christian, B. E. & Spremulli, L. L. Mechanism of protein biosynthesis in mammalian mitochondria. *Biochim. Biophys. Acta - Gene Regul. Mech.* **1819**, 1035–1054 (2012).
 43. Jacobs, H. T. Disorders of mitochondrial protein synthesis. *Hum. Mol. Genet.* **12**, 293–301 (2003).
 44. Taylor, R. W. & Turnbull, D. M. Mitochondrial DNA mutations in human disease. *Nat. Rev. Genet.* **6**, 389–402 (2005).
 45. Chung, C.-Y., Valdebenito, G. E., Chacko, A. R. & Duchon, M. R. Rewiring cell signalling pathways in pathogenic mtDNA mutations. *Trends Cell Biol.* **32**, 391–405 (2022).
 46. Zeharia, A. *et al.* Acute Infantile Liver Failure Due to Mutations in the TRMU Gene. *Am. J. Hum. Genet.* **85**, 401–407 (2009).
 47. Koh, H. *et al.* Mitochondrial Mutations in Cholestatic Liver Disease with Biliary Atresia. *Sci. Rep.* **8**, 905 (2018).
 48. Sumegi, B. & Srere, P. A. Complex I binds several mitochondrial NAD-coupled dehydrogenases. *J. Biol. Chem.* **259**, 15040–5 (1984).
 49. Lim, S. C. *et al.* Loss of the Mitochondrial Fatty Acid β -Oxidation Protein Medium-Chain Acyl-Coenzyme A Dehydrogenase Disrupts Oxidative Phosphorylation Protein Complex Stability and Function. *Sci. Rep.* **8**, 153 (2018).
 50. Saijo, T., Welch, W. J. & Tanaka, K. Intramitochondrial folding and assembly of medium-chain acyl-CoA dehydrogenase (MCAD). Demonstration of impaired transfer of K304E-variant MCAD from its complex with hsp60 to the native tetramer. *J. Biol. Chem.* **269**, 4401–8 (1994).
 51. Nsiah-Sefaa, A. & McKenzie, M. Combined defects in oxidative phosphorylation and fatty acid β -oxidation in mitochondrial disease. *Biosci. Rep.* **36**, (2016).
 52. Murphy, M. P. How mitochondria produce reactive oxygen species. *Biochem. J.* **417**, 1–13 (2009).
 53. Oyewole, A. O. & Birch-Machin, M. A. Mitochondria-targeted antioxidants. *FASEB J.* **29**, 4766–4771 (2015).
 54. Mottis, A., Herzig, S. & Auwerx, J. Mitocellular communication: Shaping health and disease. *Science (80-.)*. **366**, 827–832 (2019).
 55. Barbour, J. A. & Turner, N. Mitochondrial stress signaling promotes cellular adaptations. *Int.*

J. Cell Biol. **2014**, (2014).

56. Schröder, M. The Unfolded Protein Response. *Mol. Biotechnol.* **34**, 279–290 (2006).
57. Quirós, P. M., Mottis, A. & Auwerx, J. Mitonuclear communication in homeostasis and stress. *Nat. Rev. Mol. Cell Biol.* **17**, 213–226 (2016).
58. Jovaisaite, V., Mouchiroud, L. & Auwerx, J. The mitochondrial unfolded protein response, a conserved stress response pathway with implications in health and disease. *J. Exp. Biol.* **217**, 137–143 (2013).
59. Costa-Mattioli, M. & Walter, P. The integrated stress response: From mechanism to disease. *Science* **368**, (2020).
60. Anderson, N. S. & Haynes, C. M. Folding the Mitochondrial UPR into the Integrated Stress Response. *Trends Cell Biol.* **30**, 428–439 (2020).
61. Taniuchi, S., Miyake, M., Tsugawa, K., Oyadomari, M. & Oyadomari, S. Integrated stress response of vertebrates is regulated by four eIF2 α kinases. *Sci. Rep.* **6**, 32886 (2016).
62. Young, S. K. & Wek, R. C. Upstream open reading frames differentially regulate genespecific translation in the integrated stress response. *J. Biol. Chem.* **291**, 16927–16935 (2016).
63. Quirós, P. M. *et al.* Multi-omics analysis identifies ATF4 as a key regulator of the mitochondrial stress response in mammals. *J. Cell Biol.* **216**, 2027–2045 (2017).
64. Fiorese, C. J. *et al.* The Transcription Factor ATF5 Mediates a Mammalian Mitochondrial UPR. *Curr. Biol.* **26**, 2037–2043 (2016).
65. Jiang, D. *et al.* ATF4 Mediates Mitochondrial Unfolded Protein Response in Alveolar Epithelial Cells. *Am. J. Respir. Cell Mol. Biol.* **63**, 478–489 (2020).
66. Kasai, S. *et al.* Role of the ISRATF4 pathway and its cross talk with Nrf2 in mitochondrial quality control. *J. Clin. Biochem. Nutr.* **64**, 1–12 (2019).
67. Cortopassi, G. *et al.* Mitochondrial disease activates transcripts of the unfolded protein response and cell cycle and inhibits vesicular secretion and oligodendrocyte-specific transcripts. *Mitochondrion* **6**, 161–175 (2006).
68. Fujita, Y. *et al.* CHOP (C/EBP homologous protein) and ASNS (asparagine synthetase) induction in cybrid cells harboring MELAS and NARP mitochondrial DNA mutations. *Mitochondrion* **7**, 80–88 (2007).
69. Kim, K. H. *et al.* Metformin-induced inhibition of the mitochondrial respiratory chain increases FGF21 expression via ATF4 activation. *Biochem. Biophys. Res. Commun.* **440**, 76–81 (2013).
70. Magarin, M. *et al.* Embryonic cardiomyocytes can orchestrate various cell protective mechanisms to survive mitochondrial stress. *J. Mol. Cell. Cardiol.* **97**, 1–14 (2016).
71. Khan, N. A. *et al.* mTORC1 Regulates Mitochondrial Integrated Stress Response and Mitochondrial Myopathy Progression. *Cell Metab.* **26**, 419–428.e5 (2017).
72. Sears, T. K. & Angelastro, J. M. The transcription factor ATF5: role in cellular differentiation, stress responses, and cancer. *Oncotarget* **8**, 84595–84609 (2017).
73. Liou, Y.-H. *et al.* Hepatic Fis1 regulates mitochondrial integrated stress response and improves metabolic homeostasis. *JCI Insight* **7**, (2022).
74. Bárcena, C., Mayoral, P. & Quirós, P. M. Mitohormesis, an Antiaging Paradigm. *Int. Rev. Cell Mol. Biol.* **340**, 35–77 (2018).
75. Zhang, Q. *et al.* The Mitochondrial Unfolded Protein Response Is Mediated Cell-Non-autonomously by Retromer-Dependent Wnt Signaling. *Cell* **174**, 870–883.e17 (2018).
76. Yi, H. S., Chang, J. Y. & Shong, M. The mitochondrial unfolded protein response and mitohormesis: A perspective on metabolic diseases. *J. Mol. Endocrinol.* **61**, R91–R105 (2018).
77. Kovaleva, I. E., Garaeva, A. A. & Chumakov, P. M. Intermedin/adrenomedullin 2 is a stress-inducible gene controlled by activating transcription factor 4. *Gene* **590**, 177–185 (2016).
78. Maruyama, R., Shimizu, M., Li, J., Inoue, J. & Sato, R. Fibroblast growth factor 21 induction by activating transcription factor 4 is regulated through three amino acid response elements in its promoter region. *Biosci. Biotechnol. Biochem.* **80**, 929–934 (2016).
79. Li, D., Zhang, H. & Zhong, Y. Hepatic GDF15 is regulated by CHOP of the unfolded protein response and alleviates NAFLD progression in obese mice. *Biochem. Biophys. Res. Commun.* **498**, 388–394 (2018).
80. Chung, H. K. *et al.* Growth differentiation factor 15 is a myomitokine governing systemic energy homeostasis. *J. Cell Biol.* **216**, 149–165 (2017).

81. Wang, D. *et al.* GDF15: emerging biology and therapeutic applications for obesity and cardiometabolic disease. *Nat. Rev. Endocrinol.* **17**, 592–607 (2021).
82. Straub, L. & Wolfrum, C. FGF21, energy expenditure and weight loss - How much brown fat do you need? *Mol. Metab.* **4**, 605–609 (2015).
83. Maratos-Flier, E. Fatty liver and FGF21 physiology. *Exp. Cell Res.* **360**, 2–5 (2017).
84. Luo, Y. *et al.* Rush to the fire: FGF21 extinguishes metabolic stress, metaflammation and tissue damage. *Cytokine Growth Factor Rev.* **38**, 59–65 (2017).
85. Zhang, S.-Y., Xu, M.-J. & Wang, X. Adrenomedullin 2/intermedin: a putative drug candidate for treatment of cardiometabolic diseases. *Br. J. Pharmacol.* **175**, 1230–1240 (2018).
86. Itoh, N. & Ornitz, D. M. Evolution of the Fgf and Fgfr gene families. *Trends Genet.* **20**, 563–569 (2004).
87. Urakawa, I. *et al.* Klotho converts canonical FGF receptor into a specific receptor for FGF23. *Nature* **444**, 770–774 (2006).
88. Kurosu, H. *et al.* Tissue-specific expression of β klotho and Fibroblast Growth Factor (FGF) receptor isoforms determines metabolic activity of FGF19 and FGF21. *J. Biol. Chem.* **282**, 26687–26695 (2007).
89. De Sousa-Coelho, A. L. *et al.* FGF21 mediates the lipid metabolism response to amino acid starvation. *J. Lipid Res.* **54**, 1786–1797 (2013).
90. Dashti, H. M. *et al.* Beneficial effects of ketogenic diet in obese diabetic subjects. *Mol. Cell. Biochem.* **302**, 249–256 (2007).
91. Gälman, C. *et al.* The Circulating Metabolic Regulator FGF21 Is Induced by Prolonged Fasting and PPAR α Activation in Man. *Cell Metab.* **8**, 169–174 (2008).
92. BonDurant, L. D. *et al.* FGF21 Regulates Metabolism Through Adipose-Dependent and -Independent Mechanisms. *Cell Metab.* **25**, 935–944.e4 (2017).
93. Badman, M. K., Kennedy, A. R., Adams, A. C., Pissios, P. & Maratos-Flier, E. A very low carbohydrate ketogenic diet improves glucose tolerance in ob/ob mice independently of weight loss. *Am. J. Physiol. - Endocrinol. Metab.* **297**, 1197–1205 (2009).
94. Potthoff, M. J. *et al.* FGF21 induces PGC-1 α and regulates carbohydrate and fatty acid metabolism during the adaptive starvation response. *Proc. Natl. Acad. Sci. U. S. A.* **106**, 10853–10858 (2009).
95. Liang, Q. *et al.* FGF21 maintains glucose homeostasis by mediating the cross talk between liver and brain during prolonged fasting. *Diabetes* **63**, 4064–4075 (2014).
96. Markan, K. R. *et al.* Circulating FGF21 is liver derived and enhances glucose uptake during refeeding and overfeeding. *Diabetes* **63**, 4057–4063 (2014).
97. Hill, C. M. *et al.* FGF21 and the physiological regulation of macronutrient preference. *Endocrinol. (United States)* **161**, 1–13 (2020).
98. Med, P. *et al.* FGF21 Mediates Endocrine Control of Simple Sugar Intake and Sweet Taste Preference by the Liver Stephanie. *Cell Metab.* **25**, 1–30 (2015).
99. Jensen-Cody, S. O. *et al.* FGF21 Signals to Glutamatergic Neurons in the Ventromedial Hypothalamus to Suppress Carbohydrate Intake. *Cell Metab.* **32**, 273–286.e6 (2020).
100. Keinicke, H. *et al.* Fgf21 regulates hepatic metabolic pathways to improve steatosis and inflammation. *Endocr. Connect.* **9**, 755–768 (2020).
101. Hill, C. M. *et al.* FGF21 Signals Protein Status to the Brain and Adaptively Regulates Food Choice and Metabolism. *Cell Rep.* **27**, 2934–2947.e3 (2019).
102. Forsström, S. *et al.* Fibroblast Growth Factor 21 Drives Dynamics of Local and Systemic Stress Responses in Mitochondrial Myopathy with mtDNA Deletions. *Cell Metab.* **30**, 1040–1054.e7 (2019).
103. Lees, E. K. *et al.* Methionine restriction restores a younger metabolic phenotype in adult mice with alterations in fibroblast growth factor 21. *Aging Cell* **13**, 817–827 (2014).
104. Badman, M. K., Koester, A., Flier, J. S., Kharitonov, A. & Maratos-Flier, E. Fibroblast growth factor 21-deficient mice demonstrate impaired adaptation to ketosis. *Endocrinology* **150**, 4931–4940 (2009).
105. Assadi, A., Zahabi, A. & Hart, R. A. GDF15, an update of the physiological and pathological roles it plays: a review. *Pflugers Arch. Eur. J. Physiol.* **472**, 1535–1546 (2020).
106. Emmerson, P. J. *et al.* The metabolic effects of GDF15 are mediated by the orphan receptor GFRAL. *Nat. Med.* **23**, 1215–1219 (2017).

107. Hsu, J. Y. *et al.* Non-homeostatic body weight regulation through a brainstem-restricted receptor for GDF15. *Nature* **550**, 255–259 (2017).
108. Mullican, S. E. *et al.* GFRAL is the receptor for GDF15 and the ligand promotes weight loss in mice and nonhuman primates. *Nat. Med.* **23**, 1150–1157 (2017).
109. Chrysovergis, K. *et al.* NAG-1/GDF-15 prevents obesity by increasing thermogenesis, lipolysis and oxidative metabolism. *Int. J. Obes.* **38**, 1555–1564 (2014).
110. Jung, S. B. *et al.* Reduced oxidative capacity in macrophages results in systemic insulin resistance. *Nat. Commun.* **9**, (2018).
111. Lee, S. E. *et al.* Growth Differentiation Factor 15 Mediates Systemic Glucose Regulatory Action of T-Helper Type 2 Cytokines. *Diabetes* **66**, 2774–2788 (2017).
112. Garfield, B. E. *et al.* Growth/differentiation factor 15 causes TGF β -activated kinase 1-dependent muscle atrophy in pulmonary arterial hypertension. *Thorax* **74**, 164–176 (2019).
113. Kim, K. H. *et al.* Growth differentiation factor 15 ameliorates nonalcoholic steatohepatitis and related metabolic disorders in mice. *Sci. Rep.* **8**, 6789 (2018).
114. Koo, B. K. *et al.* Growth differentiation factor 15 predicts advanced fibrosis in biopsy-proven non-alcoholic fatty liver disease. *Liver Int.* **38**, 695–705 (2018).
115. Jung, S.-B. *et al.* Reduced oxidative capacity in macrophages results in systemic insulin resistance. *Nat. Commun.* **9**, 1551 (2018).
116. Kim, K. H. & Lee, M.-S. GDF15 as a central mediator for integrated stress response and a promising therapeutic molecule for metabolic disorders and NASH. *Biochim. Biophys. Acta - Gen. Subj.* **1865**, 129834 (2021).
117. Lv, Y. *et al.* Adrenomedullin 2 enhances beiging in white adipose tissue directly in an adipocyte-autonomous manner and indirectly through activation of M2 macrophages. *J. Biol. Chem.* **291**, 23390–23402 (2016).
118. Zhang, S. Y. *et al.* Adrenomedullin 2 improves early obesity-induced adipose insulin resistance by inhibiting the class II MHC in adipocytes. *Diabetes* **65**, 2342–2355 (2016).
119. Merry, T. L. *et al.* Mitochondrial-derived peptides in energy metabolism. *Am. J. Physiol. - Endocrinol. Metab.* **319**, E659–E666 (2020).
120. Lee, C., Yen, K. & Cohen, P. Humanin: A harbinger of mitochondrial-derived peptides? *Trends Endocrinol. Metab.* **24**, 222–228 (2013).
121. Mehta, H. H. *et al.* Metabolomic profile of diet-induced obesity mice in response to humanin and small humanin-like peptide 2 treatment. *Metabolomics* **15**, 1–12 (2019).
122. Reynolds, J. C. *et al.* MOTS-c is an exercise-induced mitochondrial-encoded regulator of age-dependent physical decline and muscle homeostasis. *Nat. Commun.* **12**, 1–11 (2021).
123. Lee, C. *et al.* The Mitochondrial-Derived Peptide MOTS-c Promotes Metabolic Homeostasis and Reduces Obesity and Insulin Resistance. *Cell Metab.* **21**, 443–454 (2015).
124. Hinzpeter, F., Gerland, U. & Tostevin, F. Optimal Compartmentalization Strategies for Metabolic Microcompartments. *Biophys. J.* **112**, 767–779 (2017).
125. Larsen, B. B. Physiological and pathological roles of mitochondrial SLC25 carriers. *Biochem. J.* **454**, 371–386 (2013).
126. Comte, J., Maisterrena, B. & Gautheron, D. C. Lipid composition and protein profiles of outer and inner membranes from pig heart mitochondria. Comparison with microsomes. *Biochim. Biophys. Acta - Biomembr.* **419**, 271–284 (1976).
127. Backes, S. & Herrmann, J. M. Protein Translocation into the Intermembrane Space and Matrix of Mitochondria: Mechanisms and Driving Forces. *Front. Mol. Biosci.* **4**, (2017).
128. Casares, D., Escribá, P. V & Rosselló, C. A. Membrane Lipid Composition: Effect on Membrane and Organelle Structure, Function and Compartmentalization and Therapeutic Avenues. *Int. J. Mol. Sci.* **20**, (2019).
129. Paradies, G., Paradies, V., De Benedictis, V., Ruggiero, F. M. & Petrosillo, G. Functional role of cardiolipin in mitochondrial bioenergetics. *Biochim. Biophys. Acta - Bioenerg.* **1837**, 408–417 (2014).
130. Lemasters, J. J. Modulation of mitochondrial membrane permeability in pathogenesis, autophagy and control of metabolism. *J. Gastroenterol. Hepatol.* **22**, S31–S37 (2007).
131. Bricker, D. K. *et al.* A mitochondrial pyruvate carrier required for pyruvate uptake in yeast, *Drosophila*, and humans. *Science* **337**, 96–100 (2012).
132. Lill, R. & Kispal, G. Mitochondrial ABC transporters. *Res. Microbiol.* **152**, 331–340 (2001).

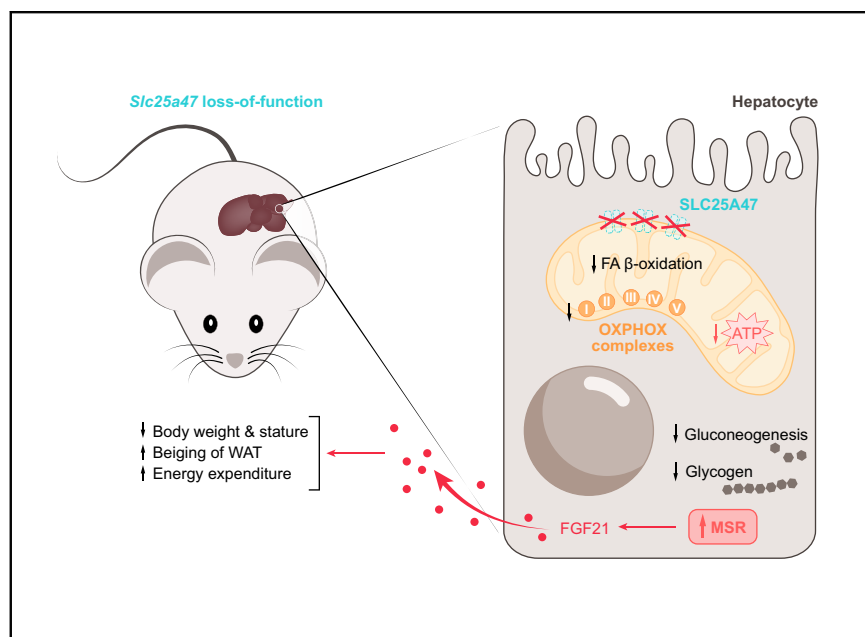
133. Kory, N. *et al.* SFXN1 is a mitochondrial serine transporter required for one-carbon metabolism. *Science* (80-.). **362**, (2018).
134. Palmieri, F. & Monné, M. Discoveries, metabolic roles and diseases of mitochondrial carriers: A review. *Biochim. Biophys. Acta - Mol. Cell Res.* **1863**, 2362–2378 (2016).
135. Palmieri, F., Pierri, C. L., De Grassi, A., Nunes-Nesi, A. & Fernie, A. R. Evolution, structure and function of mitochondrial carriers: a review with new insights. *Plant J.* **66**, 161–81 (2011).
136. Agrimi, G., Russo, A., Scarcia, P. & Palmieri, F. The human gene SLC25A17 encodes a peroxisomal transporter of coenzyme A, FAD and NAD⁺. *Biochem. J.* **443**, 241–247 (2012).
137. Janer, A. *et al.* SLC 25A46 is required for mitochondrial lipid homeostasis and cristae maintenance and is responsible for Leigh syndrome. *EMBO Mol. Med.* **8**, 1019–1038 (2016).
138. Palmieri, F. The mitochondrial transporter family (SLC25): physiological and pathological implications. *Pfluegers Arch. Eur. J. Physiol.* **447**, 689–709 (2004).
139. Palmieri, F. & Pierri, C. L. Mitochondrial metabolite transport. *Essays Biochem.* **47**, 37–52 (2010).
140. Nicholls, D. G. & Locke, R. M. Thermogenic mechanisms in brown fat. *Physiol. Rev.* **64**, 1–64 (1984).
141. Pebay-Peyroula, E. *et al.* Structure of mitochondrial ADP/ATP carrier in complex with carboxyatractyloside. *Nature* **426**, 39–44 (2003).
142. Runswick, M. J., Walker, J. E., Bisaccia, F., Iacobazzi, V. & Palmieri, F. Sequence of the bovine 2-oxoglutarate/malate carrier protein: structural relationship to other mitochondrial transport proteins. *Biochemistry* **29**, 11033–40 (1990).
143. Bisaccia, F., Indiveri, C. & Palmieri, F. Purification of reconstitutively active α -oxoglutarate carrier from pig heart mitochondria. *Biochim. Biophys. Acta - Bioenerg.* **810**, 362–369 (1985).
144. Zhong, Q., Putt, D. A., Xu, F. & Lash, L. H. Hepatic mitochondrial transport of glutathione: studies in isolated rat liver mitochondria and H4IIE rat hepatoma cells. *Arch. Biochem. Biophys.* **474**, 119–27 (2008).
145. Palmieri, F., Scarcia, P. & Monné, M. Diseases caused by mutations in mitochondrial carrier genes SLC25: A review. *Biomolecules* **10**, 1–32 (2020).
146. Okano, Y., Ohura, T., Sakamoto, O. & Inui, A. Current treatment for citrin deficiency during NICCD and adaptation/compensation stages: Strategy to prevent CTLN2. *Mol. Genet. Metab.* **127**, 175–183 (2019).
147. Kobayashi, K. *et al.* The gene mutated in adult-onset type II citrullinaemia encodes a putative mitochondrial carrier protein. *Nat. Genet.* **22**, 159–163 (1999).
148. Cheng, L. *et al.* Analysis of chemotherapy response programs in ovarian cancers by the next-generation sequencing technologies. *Gynecol. Oncol.* **117**, 159–69 (2010).
149. Dalla Pozza, E. *et al.* Role of mitochondrial uncoupling protein 2 in cancer cell resistance to gemcitabine. *Biochim. Biophys. Acta* **1823**, 1856–63 (2012).
150. Floyd, S. *et al.* The insulin-like growth factor-I-mTOR signaling pathway induces the mitochondrial pyrimidine nucleotide carrier to promote cell growth. *Mol. Biol. Cell* **18**, 3545–55 (2007).
151. Kunji, E. R. S., King, M. S., Ruprecht, J. J. & Thangaratnarajah, C. The SLC25 carrier family: Important transport proteins in mitochondrial physiology and pathology. *Physiology* **35**, 302–327 (2020).
152. César-Razquin, A. *et al.* A Call for Systematic Research on Solute Carriers. *Cell* **162**, 478–487 (2015).
153. Tan, M. G. K., Ooi, L. L. P. J., Aw, S. E. & Hui, K. M. Cloning and identification of hepatocellular carcinoma down-regulated mitochondrial carrier protein, a novel liver-specific uncoupling protein. *J. Biol. Chem.* **279**, 45235–45244 (2004).
154. Jin, X. *et al.* HDMCP uncouples yeast mitochondrial respiration and alleviates steatosis in L02 and hepG2 cells by decreasing ATP and H₂O₂ levels: A novel mechanism for NAFLD. *J. Hepatol.* **50**, 1019–1028 (2009).
155. Jin, X. *et al.* Effect of miR-146 targeted HDMCP upregulation in the pathogenesis of nonalcoholic steatohepatitis. *PLoS One* **12**, 1–16 (2017).
156. Fiermonte, G. *et al.* Identification of the Mitochondrial Glutamate Transporter. *J. Biol. Chem.* **277**, 19289–19294 (2002).
157. Gawaz, M., Douglas, M. G. & Klingenberg, M. Structure-function studies of adenine nucleotide

- transport in mitochondria. II. Biochemical analysis of distinct AAC1 and AAC2 proteins in yeast. *J. Biol. Chem.* **265**, 14202–8 (1990).
158. Townsend, R. R., Lipniunas, P. H., Tulk, B. M. & Verkman, A. S. Identification of protein kinase A phosphorylation sites on NBD1 and R domains of CFTR using electrospray mass spectrometry with selective phosphate ion monitoring. *Protein Sci.* **5**, 1865–1873 (1996).
 159. Li, H. *et al.* An Integrated Systems Genetics and Omics Toolkit to Probe Gene Function. *Cell Syst.* **6**, 90–102.e4 (2018).
 160. Jin, X. *et al.* HDMCP uncouples yeast mitochondrial respiration and alleviates steatosis in L02 and hepG2 cells by decreasing ATP and H₂O₂ levels: A novel mechanism for NAFLD. *J. Hepatol.* **50**, 1019–1028 (2009).
 161. Houtkooper, R. H. *et al.* Mitonuclear protein imbalance as a conserved longevity mechanism. *Nature* **497**, 451–457 (2013).
 162. Kang, S. G. *et al.* Differential roles of GDF15 and FGF21 in systemic metabolic adaptation to the mitochondrial integrated stress response. *iScience* **24**, 102181 (2021).
 163. Durieux, J., Wolff, S. & Dillin, A. The cell-non-autonomous nature of electron transport chain-mediated longevity. *Cell* **144**, 79–91 (2011).
 164. Copeland, J. M. *et al.* Extension of Drosophila Life Span by RNAi of the Mitochondrial Respiratory Chain. *Curr. Biol.* **19**, 1591–1598 (2009).
 165. Kim, K. H. *et al.* Autophagy deficiency leads to protection from obesity and insulin resistance by inducing Fgf21 as a mitokine. *Nat. Med.* **19**, 83–92 (2013).
 166. Inagaki, T. *et al.* Inhibition of Growth Hormone Signaling by the Fasting-Induced Hormone FGF21. *Cell Metab.* **8**, 77–83 (2008).
 167. Ye, D. *et al.* Circulating Fibroblast Growth Factor 21 Is A Sensitive Biomarker for Severe Ischemia/reperfusion Injury in Patients with Liver Transplantation. *Sci. Rep.* **6**, 1–9 (2016).
 168. Wen, B. *et al.* FGF21 Acts Centrally to Induce Sympathetic Nerve Activity, Energy Expenditure and Weight Loss. *Cell Metab.* **454**, 42–54 (2007).
 169. Joung, J. *et al.* Genome-scale CRISPR-Cas9 knockout and transcriptional activation screening. *Nat. Protoc.* **12**, 828–863 (2017).
 170. Duggavathi, R. *et al.* Liver receptor homolog 1 is essential for ovulation. *Genes Dev.* **22**, 1871–1876 (2008).
 171. Laeger, T. *et al.* Metabolic Responses to Dietary Protein Restriction Require an Increase in FGF21 that Is Delayed by the Absence of GCN2. *Cell Rep.* **16**, 707–716 (2016).
 172. Frezza, C., Cipolat, S. & Scorrano, L. Organelle isolation: Functional mitochondria from mouse liver, muscle and cultured fibroblasts. *Nat. Protoc.* **2**, 287–295 (2007).
 173. Bligh, E. G. & Dyer, W. J. A rapid method of total lipid extraction and purification. *Can. J. Biochem. Physiol.* **37**, 911–917 (1959).
 174. Söllner, J. F. *et al.* An RNA-Seq atlas of gene expression in mouse and rat normal tissues. *Sci. data* **4**, 170185 (2017).
 175. Leggett, R. M., Ramirez-Gonzalez, R. H., Clavijo, B. J., Waite, D. & Davey, R. P. Sequencing quality assessment tools to enable data-driven informatics for high throughput genomics. *Front. Genet.* **4**, (2013).
 176. Dobin, A. *et al.* STAR: ultrafast universal RNA-seq aligner. *Bioinformatics* **29**, 15–21 (2013).
 177. Han, X. *et al.* Mapping the Mouse Cell Atlas by Microwell-Seq. *Cell* **172**, 1091–1107.e17 (2018).
 178. Xiong, X. *et al.* Landscape of Intercellular Crosstalk in Healthy and NASH Liver Revealed by Single-Cell Secretome Gene Analysis. *Mol. Cell* **75**, 644–660.e5 (2019).
 179. Edgar, R. Gene Expression Omnibus: NCBI gene expression and hybridization array data repository. *Nucleic Acids Res.* **30**, 207–210 (2002).
 180. The Tabula Muris Consortium. Single-cell transcriptomics of 20 mouse organs creates a Tabula Muris. *Nature* **562**, 367–372 (2018).
 181. Hao, Y. *et al.* Integrated analysis of multimodal single-cell data. *Cell* **184**, 3573–3587.e29 (2021).
 182. Pernicova, I. & Korbonits, M. Metformin—mode of action and clinical implications for diabetes and cancer. *Nat. Rev. Endocrinol.* **10**, 143–156 (2014).
 183. Münch, C. & Harper, J. W. Mitochondrial unfolded protein response controls matrix pre-RNA processing and translation. *Nature* **534**, 710–713 (2016).

184. Bao, X. R. *et al.* Mitochondrial dysfunction remodels one-carbon metabolism in human cells. *Elife* **5**, (2016).
185. Zhao, Q. A mitochondrial specific stress response in mammalian cells. *EMBO J.* **21**, 4411–4419 (2002).
186. Aldridge, J. E., Horibe, T. & Hoogenraad, N. J. Discovery of Genes Activated by the Mitochondrial Unfolded Protein Response (mtUPR) and Cognate Promoter Elements. *PLoS One* **2**, e874 (2007).
187. Flippo, K. H. & Potthoff, M. J. Metabolic Messengers: FGF21. *Nat. Metab.* **3**, 309–317 (2021).
188. BonDurant, L. D. & Potthoff, M. J. Fibroblast Growth Factor 21: A Versatile Regulator of Metabolic Homeostasis. *Annu. Rev. Nutr.* **38**, 173–196 (2018).
189. Conte, M., Martucci, M., Chiariello, A., Franceschi, C. & Salvioli, S. Mitochondria, immunosenescence and inflammaging: a role for mitokines? *Semin. Immunopathol.* **42**, 607–617 (2020).
190. Martinus, R. D. *et al.* Selective Induction of Mitochondrial Chaperones in Response to Loss of the Mitochondrial Genome. *Eur. J. Biochem.* **240**, 98–103 (1996).
191. Michel, S., Canonne, M., Arnould, T. & Renard, P. Inhibition of mitochondrial genome expression triggers the activation of CHOP-10 by a cell signaling dependent on the integrated stress response but not the mitochondrial unfolded protein response. *Mitochondrion* **21**, 58–68 (2015).
192. Mouchiroud, L. *et al.* The NAD⁺/Sirtuin Pathway Modulates Longevity through Activation of Mitochondrial UPR and FOXO Signaling. *Cell* **154**, 430–441 (2013).
193. Zhang, H. *et al.* NAD⁺ repletion improves mitochondrial and stem cell function and enhances life span in mice. *Science (80-.)*. **352**, 1436–1443 (2016).
194. Van Aken, O. *et al.* Defining the Mitochondrial Stress Response in *Arabidopsis thaliana*. *Mol. Plant* **2**, 1310–1324 (2009).
195. Li, X. *et al.* Mitochondrial dysfunction in fibrotic diseases. *Cell Death Discov.* **6**, 80 (2020).
196. Palmieri, F. The mitochondrial transporter family SLC25: Identification, properties and physiopathology. *Mol. Aspects Med.* **34**, 465–484 (2013).
197. Go, Y. M., Chandler, J. D. & Jones, D. P. The cysteine proteome. *Free Radic. Biol. Med.* **84**, 227–245 (2015).
198. Hou, W.-L. *et al.* Inhibition of mitochondrial complex I improves glucose metabolism independently of AMPK activation. *J. Cell. Mol. Med.* **22**, 1316–1328 (2018).
199. Yang, M. *et al.* Inhibition of mitochondrial function by metformin increases glucose uptake, glycolysis and GDF-15 release from intestinal cells. *Sci. Rep.* **11**, 2529 (2021).
200. Huang, W., Castelino, R. L. & Peterson, G. M. Lactate Levels with Chronic Metformin Use: A Narrative Review. *Clin. Drug Investig.* **37**, 991–1007 (2017).
201. Hur, K. Y. & Lee, M. New mechanisms of metformin action: Focusing on mitochondria and the gut. *J. Diabetes Investig.* **6**, 600–609 (2015).
202. Sorrentino, V. *et al.* Enhancing mitochondrial proteostasis reduces amyloid- β proteotoxicity. *Nature* **552**, 187–193 (2017).
203. Romani, M. *et al.* NAD⁺ boosting reduces age-associated amyloidosis and restores mitochondrial homeostasis in muscle. *Cell Rep.* **34**, 108660 (2021).
204. Gariani, K. *et al.* Eliciting the mitochondrial unfolded protein response by nicotinamide adenine dinucleotide repletion reverses fatty liver disease in mice. *Hepatology* **63**, 1190–1204 (2016).
205. Katsyuba, E. *et al.* De novo NAD⁺ synthesis enhances mitochondrial function and improves health. *Nature* **563**, 354–359 (2018).
206. Rochette, L. *et al.* Mitochondrial SLC25 Carriers: Novel Targets for Cancer Therapy. *Molecules* **25**, (2020).
207. Potter, M., Newport, E. & Morten, K. J. The Warburg effect: 80 years on. *Biochem. Soc. Trans.* **44**, 1499–1505 (2016).

Slc25a47 locus is a novel determinant of hepatic mitochondrial function implicated in liver fibrosis

Graphical abstract



Highlights

- SLC25A47 is a liver-specific transporter required to maintain mitochondrial homeostasis in hepatocytes.
- *Slc25a47*^{hep-/-} mice display impaired mitochondrial respiration, which leads to energy deficiency and fibrosis in hepatocytes.
- *Slc25a47*^{hep-/-} mice display a robust activation of the mitochondrial stress response (MSR) in hepatocytes associated with the secretion of the mitokine FGF21.
- FGF21 drives a hypermetabolic phenotype in *Slc25a47*^{hep-/-} mice.

Authors

Nadia Bresciani, Hadrien Demagny, Vera Lemos, ..., Alessia Perino, Johan Auwerx, Kristina Schoonjans

Correspondence

kristina.schoonjans@epfl.ch (K. Schoonjans).

Lay summary

Herein, we report the importance of a locus containing a liver-specific gene coding for a mitochondrial transport protein called SLC25A47. Mitochondria are the powerhouses of cells. They are crucial for metabolism and energy generation. We show that mice with genetic disruption of the *Slc25a47* locus cannot maintain mitochondrial homeostasis (balance), leading to wide-ranging problems in the liver that have far-reaching physiological consequences.

Slc25a47 locus is a novel determinant of hepatic mitochondrial function implicated in liver fibrosis

Nadia Bresciani^{1, #}, Hadrien Demagny^{1, #}, Vera Lemos¹, Francesca Pontanari^{1, \$}, Xiaoxu Li^{2, \$}, Yu Sun¹, Hao Li^{1, 2}, Alessia Perino¹, Johan Auwerx², Kristina Schoonjans^{1, *}¹Laboratory of Metabolic Signaling, Institute of Bioengineering, School of Life Sciences, Ecole Polytechnique Fédérale de Lausanne, CH-1015 Lausanne, Switzerland; ²Laboratory of Integrative Systems Physiology, Institute of Bioengineering, School of Life Sciences, Ecole Polytechnique Fédérale de Lausanne, CH-1015 Lausanne, Switzerland

Background & Aims: Transporters of the SLC25 mitochondrial carrier superfamily bridge cytoplasmic and mitochondrial metabolism by channeling metabolites across mitochondrial membranes and are pivotal for metabolic homeostasis. Despite their physiological relevance as gatekeepers of cellular metabolism, most of the SLC25 family members remain uncharacterized. We undertook a comprehensive tissue distribution analysis of all *Slc25* family members across metabolic organs and identified *SLC25A47* as a liver-specific mitochondrial carrier.

Methods: We used a murine loss-of-function model to unravel the role of this transporter in mitochondrial and hepatic homeostasis. We performed extensive metabolic phenotyping and molecular characterization of newly generated *Slc25a47*^{hep-/-} and *Slc25a47-Fgf21*^{hep-/-} mice.

Results: *Slc25a47*^{hep-/-} mice displayed a wide variety of metabolic abnormalities, as a result of sustained energy deficiency in the liver originating from impaired mitochondrial respiration. This mitochondrial phenotype was associated with an activation of the mitochondrial stress response (MSR) in the liver, and the development of fibrosis, which was exacerbated upon feeding a high-fat high-sucrose diet. The MSR induced the secretion of several mitokines, amongst which FGF21 played a preponderant role on systemic physiology. To dissect the FGF21-dependent and -independent physiological changes induced in *Slc25a47*^{hep-/-} mice, we generated a double *Slc25a47-Fgf21*^{hep-/-} mouse model and demonstrated that several aspects of the hypermetabolic state were driven by hepatic secretion of FGF21. On the other hand, the metabolic fuel inflexibility observed in *Slc25a47*^{hep-/-} mice could not be rescued with the genetic removal of *Fgf21*.

Conclusion: Collectively, our data place the *Slc25a47* locus at the center of mitochondrial homeostasis, which upon dysfunction triggers robust liver-specific and systemic adaptive stress responses. The prominent role of the *Slc25a47* locus in hepatic

fibrosis identifies this carrier, or its transported metabolite, as a potential target for therapeutic intervention.

Lay summary: Herein, we report the importance of a locus containing a liver-specific gene coding for a mitochondrial transport protein called SLC25A47. Mitochondria are the powerhouses of cells. They are crucial for metabolism and energy generation. We show that mice with genetic disruption of the *Slc25a47* locus cannot maintain mitochondrial homeostasis (balance), leading to wide-ranging problems in the liver that have far-reaching physiological consequences.

© 2022 The Author(s). Published by Elsevier B.V. on behalf of European Association for the Study of the Liver. This is an open access article under the CC BY license (<http://creativecommons.org/licenses/by/4.0/>).

Introduction

Compartmentalization plays a key role in metabolic regulation, enabling spatial separation of opposing anabolic and catabolic pathways in distinct organelles.¹ The functionality of compartmentalization relies on the expression of specific transporters that fine-tune the channeling of metabolites across subcellular compartments. Together with enzymes, such carriers define the metabolic identity of the cell and establish what a cell can and cannot do in terms of metabolism. Of all organelles, mitochondria are noticeable for their fundamental role in intermediary metabolism. All major types of nutrients pass through mitochondria as part of intermediary metabolism, including the degradation products of fats, sugars, proteins, as well as nucleotides, vitamins, and inorganic ions. Mitochondria are enveloped by a double membrane, of which the outer is relatively permeable to solutes due the presence of voltage-dependent anion channels. The inner mitochondrial membrane, however, is comparatively impermeable to maintain efficient oxidative phosphorylation.² To overcome this physical barrier, members of the mitochondrial inner membrane SLC25 (solute carrier family 25) family facilitate the transport of molecules involved in a variety of processes including metabolic cycles, oxidative phosphorylation, DNA maintenance, and iron metabolism.³

Metabolic flexibility encompasses the ability to rapidly modify the oxidation of nutrients according to their availability. The liver in general, and hepatic mitochondria in particular, play a central role in this process, allowing the organism to switch from fatty acid oxidation during the fasted state to enhanced glucose metabolism during the fed state.⁴ Consequently,

Keywords: Liver; Metabolism; Mitochondrial Solute Carriers; Mitochondrial Stress Response; FGF21; Fibrosis.

Received 26 November 2021; received in revised form 27 April 2022; accepted 17 May 2022; available online xxx

* Corresponding author. Address: Laboratory of Metabolic Signaling, Institute of Bioengineering, School of Life Sciences, Ecole Polytechnique Fédérale de Lausanne, CH-1015 Lausanne, Switzerland. Tel.: +41 21 693 18 91.

E-mail address: kristina.schoonjans@epfl.ch (K. Schoonjans).

[#] These authors contributed equally to this work.

^{\$} These authors contributed equally to this work.

<https://doi.org/10.1016/j.jhep.2022.05.040>



ELSEVIER

impaired mitochondrial activity in the liver characterizes metabolic inflexibility, *i.e.* the inability to adapt to nutritional transitions frequently observed in obesity and type 2 diabetes.⁴ Thus, hepatic mitochondrial fitness is an important hallmark of metabolic flexibility and a better understanding of liver mitochondrial metabolism may reveal new approaches to manage metabolic disorders. While the role of mitochondrial enzymes in supporting hepatic metabolism has been well characterized,⁵ the regulatory function of mitochondrial carriers has been largely understudied. To fill this gap, we sought to determine the expression, distribution, and function of mitochondrial transporters in the liver. In this study, we report the critical role of the *Slc25a47* locus, containing a poorly characterized liver-specific mitochondrial carrier, in hepatic and whole-body metabolic homeostasis.

Materials and methods

Animal studies

C57BL/6 *Slc25a47*^{tm1a(EUCOMM)Hmgu} mice were obtained from the European Mouse Mutant Cell Repository (EuMMCR); in this model, a LoxP- and FRT-flanked LacZ/neomycin resistance cassette was inserted upstream of exon 5 of *Slc25a47*. LoxP sites were inserted upstream of exon 5 and downstream of exon 6, thus flanking exons 5 and 6. *Slc25a47*^{tm1a(EUCOMM)Hmgu} mice were initially crossed with CMV-Flp mice (The Jackson Laboratories, JAX#012930) to remove the LacZ/neomycin cassette leaving exons 5 and 6 floxed (*Slc25a47*^{tm1c(EUCOMM)Hmgu}, also referred to as *Slc25a47*^{flox/flox} mice). These 2 exons encode most of the protein (209/310 amino acids). *Slc25a47*^{tm1c(EUCOMM)Hmgu} mice were then crossed with an Alb-Cre recombinase mouse line (The Jackson Laboratories, JAX stock #003574) to generate *Slc25a47*^{hep-/-} mice harboring a hepatocyte-specific deletion of *Slc25a47*. *Slc25a47*-*Fgf21*^{hep-/-} animals were obtained by crossing *Slc25a47*^{hep-/-} with *Fgf21*^{flox/flox} mice (The Jackson Laboratories, JAX stock #022361). Mice were housed with ad libitum access to water and food (normal chow, Safe 150 or high-fat high-sucrose [HFHS] diet, Envigo TD.08811) and kept under a 12-hour dark/12-hour light cycle (7pm/7am) with a temperature of 22°C±1°C and a humidity of 60%±20%. Only male mice were used in this study. For fasting protocols, mice were fasted overnight before euthanizing (from 6pm to 9am). For fed experiments, food was removed at 7am (beginning of the light phase) and mice were euthanized 2 hours later (9am). For fed electron microscopy (EM) analysis, food was not removed. For the HFHS diet study, 8-week-old mice were fed a HFHS diet for 14 weeks.

Tolerance tests

For the pyruvate tolerance test (PTT) and the insulin tolerance test (ITT), food was removed from 8am until 2pm (6-hour mild fasting) and mice were single-caged before oral gavage of 2 g/kg sodium pyruvate or intraperitoneal injection of 0.5 IU insulin/kg, respectively. For the oral glucose tolerance test (OGTT), mice were fasted (following fasting protocol) and single-caged before the experiment; 2 g/kg of glucose was administered by oral gavage. In all the tolerance tests, glucose levels were measured with a glucometer at time: 0 (*i.e.* before injection/gavage) and 15, 30, 45, 60, 90 minutes after injection/gavage. For OGTT, glycemia levels were also measured 120 minutes after gavage and additional blood was collected with a capillary tube at time 0, 15, 30, 60 minutes.

Indirect calorimetry

The indirect calorimetry experiment was performed using the Promethion System (Sable Systems International). Each mouse was individually placed in a cage with normal bedding and free access to food and water during the test, which lasted approximately 48 hours (24 hours of acclimation and 24 hours of measurement in normal feeding conditions). The system was set to a 12/12-hour light/dark cycle. Data were normalized on metabolic body mass (body weight, BW^{0.75}).

Food intake recording

Food intake was recorded at regular intervals (20 minutes) using a TSE PhenoMaster system (TSE Systems GmbH, Germany). Each mouse was placed individually in a cage with normal bedding and free access to food and water during the test, which lasted approximately 48 hours (24 hours of acclimation and 24 hours of measurement in normal feeding conditions). The system was set to a 12/12-hour light/dark cycle.

Study approval

All animal procedures were approved by the Swiss authorities (Canton of Vaud, animal protocols #3221, #3221.1) and performed in accordance with our institutional guidelines.

Western blotting

Liver tissues or mitochondrial pellets were homogenized with RIPA buffer (50 mM Tris-HCl pH 7.4, 150 mM NaCl, 0.1% SDS, 0.5% sodium deoxycholate, 1% NP-40, 2 mM EDTA and 50 mM NaF) supplemented with 1 mM PMSF and protease and phosphatase inhibitor cocktails (Roche). Before running SDS-PAGE, whole liver protein lysates were boiled for 5 min at 95°C. For mitochondrial protein immunoblot, lysates were not boiled. The following antibodies were used for immunoblotting: SLC25A47 (custom antibody manufactured by YenZym Antibodies LCC; Novus Biologicals, #NB100-57843), HSP70 (Abcam, #ab2787), VINCULIN (Abcam, #ab129002), HSP90 (BD Biosciences #610418), YME1L1 (Cusabio, #PA026267GA01HU), HSPA9 (Antibodies online, #ABIN361739), LONP1 (Sigma, #HPA002192) and GAPDH (Santa Cruz Biotechnology, #sc-365062). VINCULIN (Fig. 1B, S4D) and GAPDH (Fig. 4E) served as protein loading control; HSP90 (Fig. 2B) as mitochondrial protein loading control. All antibodies are listed in Table S2 and in the supplementary CTAT table.

mRNA analysis

RNA was extracted from the tissues of the mice using TRIZOL (Invitrogen) and purified with the RNeasy MinElute cleanup kit (Qiagen) following the manufacturer's instructions. For quantitative reverse transcription PCR (RT-qPCR), cDNA was generated using the QuantiTect® Reverse Transcription Kit (Qiagen) and analyzed by RT-qPCR (SYBR Green chemistry) using a Light-Cycler® 480 Real-Time PCR System (Roche) and the primers listed in Table S1 and the supplementary CTAT table. Results were normalized to the mean of 36b4 or B2m ($\Delta\Delta C_t$ method).

Mitochondria isolation

Mitochondria were isolated from livers or cells as previously described.⁶ Pellets of mitochondria were resuspended with RIPA buffer for Western Blot (refer to Western Blotting section) or MiRO5 for respiration assays (see below).

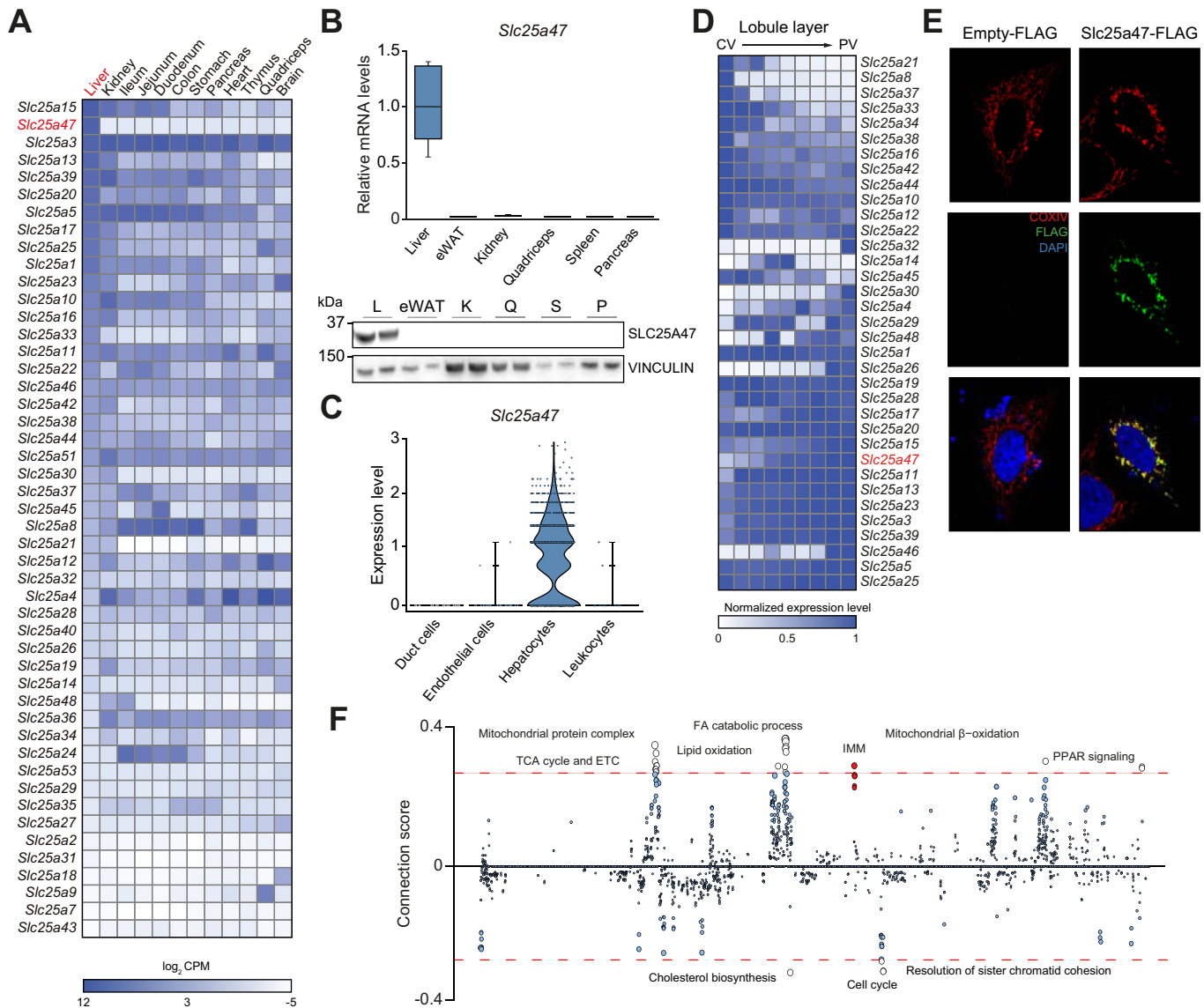


Fig. 1. SLC25A47 is a hepatocyte-specific mitochondrial carrier. (A) Heatmap representing mRNA levels (\log_2 CPM) of murine SLC25 carriers in different tissues. Average of 3 male mice (C57BL/6 J, 7/8-week-old). ENA: #ERP104395. SLC25s are ranked (top to bottom) according to their relative abundance in the liver. (B) *Slc25a47* gene expression ($n = 3$) and protein levels ($n = 2$) in different tissues from 14-week-old C57BL/6 mice (L, liver; eWAT, epididymal white adipose tissue; K, kidney; Q, quadriceps; S, spleen; P, pancreas). (C) Single-cell RNA sequencing data of murine liver cell populations (3 female and 4 male C57BL/6 mice, 10-15-week-old) from *Tabula Muris* (GEO #109774, microfluidic droplet counting). (D) Heatmap representing the mRNA levels of murine SLC25 carriers across different hepatic layers. Data from GSE84498 (CV, central vein; PV, portal vein). (E) FLAG (green) and COXIV (red) immunofluorescence staining of HeLa cells overexpressing Empty-FLAG or FLAG-tagged SLC25A47. DAPI (blue) was used to stain nuclei. Scale bar: 50 μ m. (F) Gene module association determination analysis of *Slc25a47* in mouse liver datasets. The dashed lines indicate the applied threshold (0.26). Known modules connected to *Slc25a47* are in red, and other modules over the threshold are in black. CPM, counts per million; FA, fatty acid; TCA, tricarboxylic acid; ETC, electron transport chain; IMM, inner mitochondrial membrane.

Mitochondria functional assessment

Oxygen consumption rate (OCR) was assessed in freshly isolated intact mitochondria or whole liver homogenate in respiration medium (MiR 05-kit, Oroboros Instruments) by high-resolution respirometry (Oxygraph 2k, Oroboros Instruments) following manufacturers' instructions. Whole liver lysates were normalized on 16 S content or citrate synthase activity, while intact isolated mitochondria were normalized on (outer membrane) mitochondrial protein levels before performing the assay. For the respirometry assay compounds were added into the 2 ml-chamber. Compounds used: pyruvate (5 mM, Sigma), malate (2 mM, Sigma), glutamate (10 mM, Sigma), succinate (10 mM,

Sigma), complex I-inhibitor rotenone (0.1 μ M, Sigma) and ADP+Mg²⁺ (1.25 mM, Sigma) for complex II respiration, FCCP (titration of 1 μ l each from 1 mM stock, Sigma) for maximal respiration, and oligomycin (2 μ g/ml Millipore) for uncoupled respiration. For fatty acid oxidation assay, palmitoyl-carnitine (50 μ M, Sigma) and octanoyl-carnitine (0.2 mM, Tocris bioscience) were used in the presence of ADP. Malate was added to sustain fatty acid degradation and avoid acetyl-CoA accumulation. At the end of the protocol run, 2.5 μ M Antimycin A was used to assess non-mitochondrial respiration. All the represented values were Antimycin A subtracted. To determine mitochondrial DNA content, genomic DNA was extracted from liver tissues

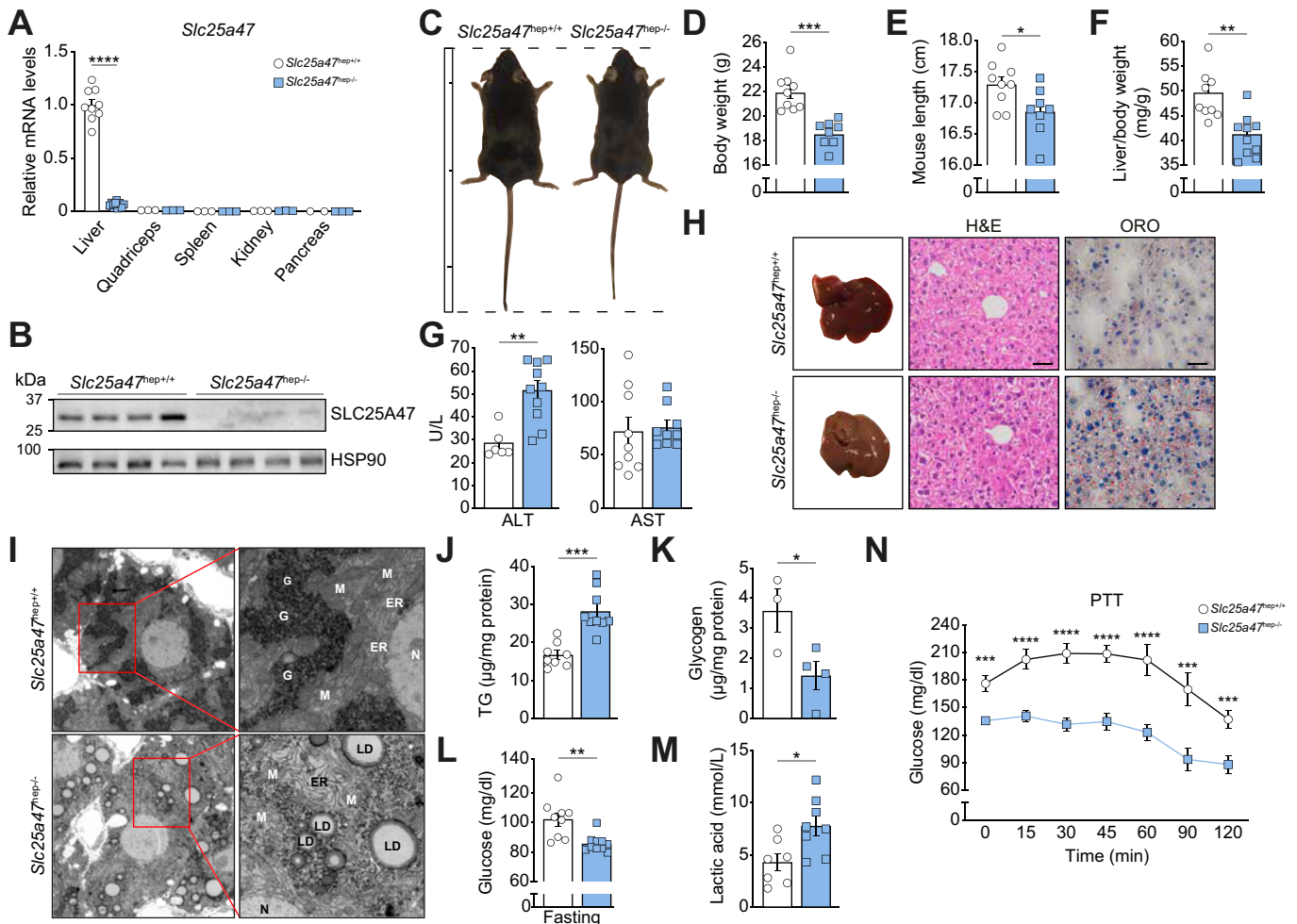


Fig. 2. *Slc25a47*-deficient mice display hepatic metabolic dysregulation. (A) *Slc25a47* transcript profiling in tissues from *Slc25a47* floxed (*Slc25a47*^{hep+/+}) and hepatocyte-specific *Slc25a47* mutant (*Slc25a47*^{hep-/-}) mice (9-week-old, n = 8 liver, n = 3 other tissues). (B) SLC25A47 immunoblot of liver mitochondrial extracts (n = 4) from mice described in panel A. (C) Representative pictures of *Slc25a47*^{hep+/+} and *Slc25a47*^{hep-/-} mice. Ruler: 5 cm marks. (D-F) Body weight (D), length (E) and liver weight over body weight (F) of 8-week-old fed mice (n = 8-9). (G) Plasma levels of ALT and AST in fed mice (n = 7). (H) Representative images of livers and their staining with H&E and ORO from fed mice. Scale bars: 20 μ m. (I) Representative EM images of livers from fed *Slc25a47*^{hep+/+} and *Slc25a47*^{hep-/-} mice. Magnified images (right panels) show glycogen (G), mitochondria (M), endoplasmic reticulum (ER), lipid droplets (LD) and nucleus (N). Scale bar: 5 μ m. (J) Hepatic TG content in fed 8-week-old mice (n = 8-9). (K) Glycogen content in hepatic extracts from 8-week-old mice (n = 3-4). (L) Blood glucose levels in fasted 12-week-old mice (n = 8). (M) Plasma lactate in fed 8-week-old mice (n = 7). (N) Blood glucose levels during intraperitoneal PTT in 10-week-old mice (n = 8). Error bars represent mean \pm SEM. **p* < 0.05, ***p* < 0.01, ****p* < 0.001 and *****p* < 0.0001 relative to *Slc25a47*^{hep+/+} mice, as determined by unpaired Student's *t* test (A, D-G, J-M) or two-way ANOVA and Bonferroni *post hoc* correction (N). EM, electron microscopy; ORO, oil red O; PTT, pyruvate tolerance test; TG, triglyceride.

using NucleoSpin Tissue (Macherey-Nagel), and RT-qPCR was performed for the expression analysis of 16 *s* (mitochondrial) normalized to *Hk2* (nuclear gene). Citrate synthase activity was determined in a 96 well-plate using 50 μ g of liver protein by adding 2 mg/ml DTNB (5,5-dithio-bis-2-nitrobenzoic acid, Sigma) and 15 mM acetyl-CoA (Sigma). Background absorbance at 412 nm was assessed using a spectrophotometer for 5 consecutive reads before addition of 10 mM oxaloacetate (Sigma). The reaction was measured by following the absorbance (412 nm) at 10 s intervals 25 times. ATP levels were measured using ATP assay kit (Abcam, for Fig. 3A) or Cell Titer Glo (Promega, for Fig. 6F, S1F) using ATP standard curve, according to the manufacturer's instructions.

Statistical analysis

Data were represented and analyzed using GraphPad Prism (v9.2.0). Plots are expressed as means \pm SEM. Comparison of differences between 2 groups was assessed using unpaired 2-tailed Student's *t* tests. Multiple group comparisons were assessed by one-way or two-way ANOVA with Bonferroni *post hoc* correction or Tukey's multiple comparison test. Differences below *p* < 0.05 were considered statistically significant (**p* < 0.05, ***p* < 0.01, ****p* < 0.001, *****p* < 0.0001). Statistical methods and corresponding *p* values for the data shown in each figure are described in their respective legends.

Detailed methods, bioinformatic analysis and additional assays are described in the [supplementary methods section](#).

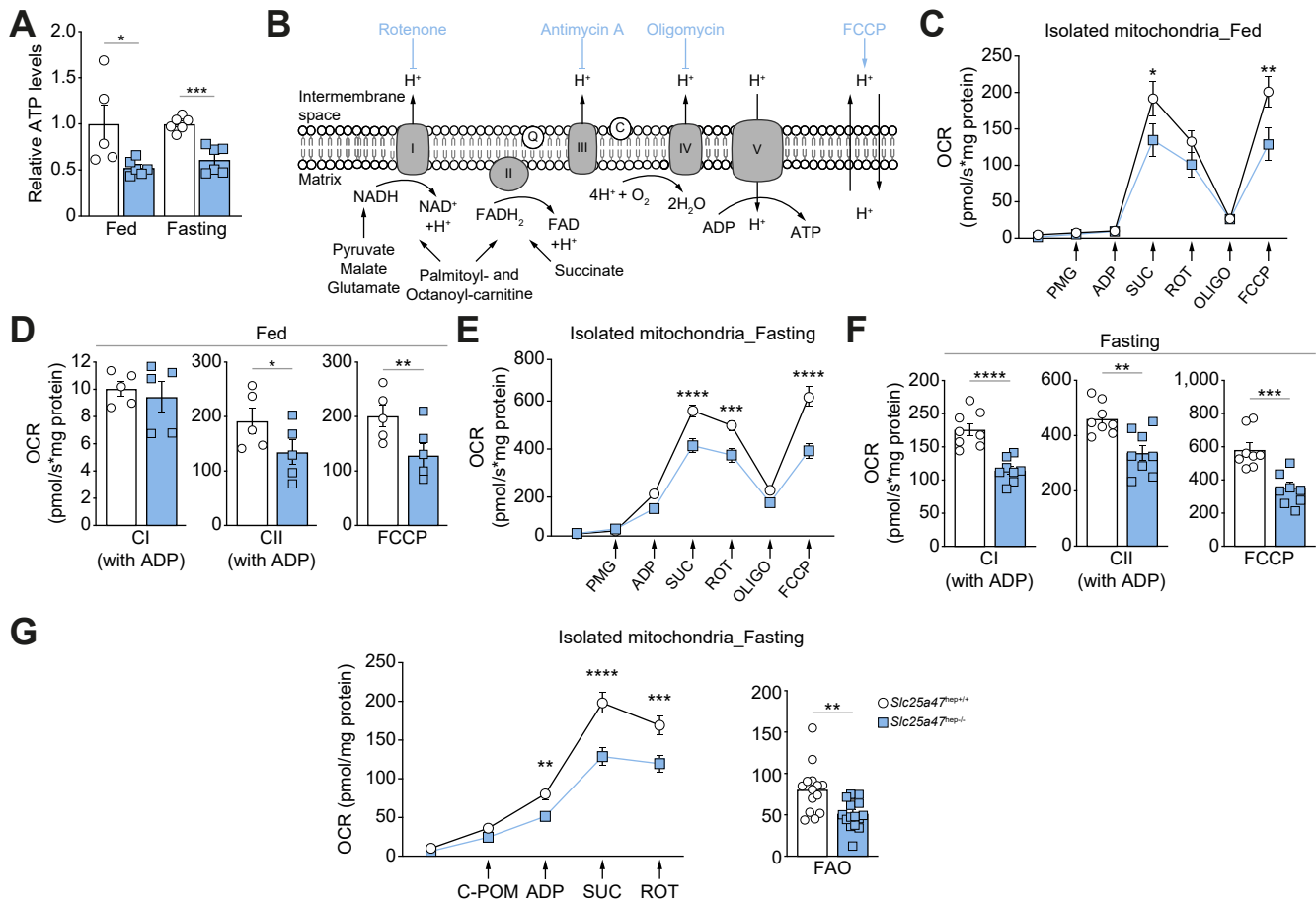


Fig. 3. Genetic disruption of the *Slc25a47* locus causes hepatic mitochondrial dysfunction. (A) Relative hepatic ATP levels from fed and fasted 8-week-old *Slc25a47*^{hep+/+} and *Slc25a47*^{hep-/-} mice (n = 5-6). (B) Scheme representing the procedure to assess OCR. (C-F) Time course (C, E) and bar graph (D, F) representing OCR of freshly isolated mitochondria from fed (C, D) and fasted (E, F) 8-week-old *Slc25a47*^{hep+/+} and *Slc25a47*^{hep-/-} mice (n = 5-8). CI-CII (with ADP): Complex I (pyruvate, malate, glutamate) and Complex II (pyruvate, malate, glutamate, succinate, rotenone) substrates in the presence of ADP. (G) OCR of freshly isolated liver mitochondria from mice described in panel E (n = 8). FAO: fatty acid oxidation substrates (C-POM) in the presence of ADP. Error bars represent mean ± SEM. *p < 0.05, **p < 0.01, ***p < 0.001 and ****p < 0.0001 relative to *Slc25a47*^{hep+/+} mice, as determined by unpaired Student's *t* test (A, D, F, AUC in G) or two-way ANOVA and Bonferroni *post hoc* correction (C, E, G). C-POM, palmitoyl- and octanoyl-carnitine with malate; OCR, oxygen consumption rate.

Results

SLC25A47 is a hepatocyte-specific mitochondrial carrier

Despite their roles as gatekeepers of metabolic fluxes, mitochondrial carriers have been understudied.⁷ To better characterize this family of transporters, we analyzed published RNA sequencing (RNA-seq) data⁸ and undertook a comprehensive tissue distribution analysis of all SLC25 family members across 12 metabolic organs (Fig. 1A). This analysis revealed that members of the SLC25 family vary greatly in their tissue distribution with some members widely expressed across tissues such as the phosphate carrier, *Slc25a3* (Fig. 1A), while others displayed a highly restricted pattern of expression such as *Slc25a18*, a glutamate transporter⁹ solely expressed in the brain (Fig. 1A). Only one carrier, *Slc25a47*, was strictly confined to the liver, where its expression levels were as high as some major mitochondrial carriers such as the ornithine transporter (*Slc25a15*, Fig. 1A). The liver-specific expression of *Slc25a47* was further confirmed when we interrogated over 29 murine tissues available on published datasets¹⁰ (Fig. S1A). RT-qPCR and immunoblotting on different mouse tissues corroborated the restricted hepatic expression of SLC25A47 (Fig. 1B).

To gain further insight into the expression of this carrier at the cellular level, we analyzed published single-cell RNA-seq (scRNA-seq) data.^{11,12} These analyses revealed that *Slc25a47* is uniquely expressed in hepatocytes (Fig. 1C) with the highest expression in periportal hepatocytes (Fig. 1D), a result confirmed by *in situ* hybridization (Fig. S1B). At the subcellular level, ectopic overexpression of SLC25A47-FLAG in HeLa cells revealed colocalization with the inner mitochondrial membrane protein, cytochrome c oxidase subunit 4 (Fig. 1E), confirming the putative mitochondrial localization of SLC25A47. To identify the metabolic pathways associated with *Slc25a47*, we performed gene module association determination (G-MAD) analysis using mouse liver data and gene/pathways annotations.¹³ This analysis showed positive correlations between *Slc25a47* and the mitochondrial compartment, such as mitochondrial protein complexes, tricarboxylic acid cycle, electron transport chain (ETC), inner mitochondrial membrane, peroxisome proliferator-activated receptor (PPAR) signaling, lipid catabolism, and fatty acid oxidation (Fig. 1F). Conversely, *Slc25a47* negatively correlated with genes involved in cellular proliferation and cholesterol biosynthesis (Fig. 1F). SLC25A47 has been reported to act as an uncoupler.^{14,15}

To address this point, we used a Crispr/Cas9 system to boost the endogenous expression of *Slc25a47* in AML12 cells (Fig. S1C). A moderate, but significant, increase in respiration was observed upon induction of *Slc25a47* transcript levels (Fig. S1D-E). In contrast to previous reports, induction of *Slc25a47* stimulated coupled, but not uncoupled respiration (Fig. S1E), and increased ATP levels (Fig. S1F), suggesting that, in this experimental setup, SLC25A47 did not act as an uncoupler. Collectively, our data reveal that SLC25A47 is an inner mitochondrial membrane transporter highly and exclusively expressed in hepatocytes, suggesting an important role in hepatic metabolism.

***Slc25a47*-deficient mice display hepatic metabolic dysregulation**

To understand the role of SLC25A47 in hepatic metabolism, we generated a mouse line carrying an hepatocyte-specific somatic deletion in the *Slc25a47* locus (*Slc25a47*^{hep-/-}) (Fig. S2A, B). RT-qPCR (Fig. 2A), immunoblotting (Fig. 2B), and RNAscope (Fig. S2C) analyses confirmed deletion of the carrier in *Slc25a47*^{hep-/-} livers. *Slc25a47*^{hep-/-} mice were distinctively shorter and lighter than their wild-type littermates (Fig. 2C-E), suggesting a broad impact on physiology. We noticed that 8-week-old *Slc25a47*^{hep-/-} male mice displayed a reduced liver to body weight ratio both in the fed (Fig. 2F) and fasted state (Fig. S2D). Furthermore, plasma levels of aspartate aminotransferase and alanine aminotransferase were elevated, indicative of hepatic damage, which was more pronounced in the fasted state (Fig. S2E-F) than when animals were fed *ad libitum* (Fig. 2G). The livers of these *Slc25a47*^{hep-/-} mice were also paler, which is suggestive of lipid accumulation (Fig. 2H). Accordingly, light microscopy (Fig. 2H; S2G), EM (Fig. 2I; S2H-I), and biochemical analyses (Fig. 2J; S2J-K) revealed abnormal lipid and cholesterol accumulation in the liver of fed and fasted *Slc25a47*^{hep-/-} mice, consistent with G-MAD analysis (Fig. 1F). In the fed state, EM subcellular imaging and enzymatic assessment revealed substantial depletion of glycogen stores (Fig. 2I, K) in *Slc25a47*^{hep-/-} livers suggestive of dysregulated glucose management in hepatocytes. This observation prompted us to further assess the role of the *Slc25a47* locus in glucose homeostasis. We found that fasted *Slc25a47*^{hep-/-} mice were markedly hypoglycemic (Fig. 2L) and had increased plasma lactate levels (Fig. S2L; 2M). To investigate whether this phenotype could arise from an impairment in *de novo* glucose production, we subjected the mice to a PTT. Glycemic excursion in response to pyruvate during PTT was significantly compromised in the *Slc25a47*^{hep-/-} mice (Fig. 2N). In sum, *Slc25a47*^{hep-/-} mice display a wide range of metabolic alterations ranging from altered gluconeogenesis and liver lipid metabolism to decreased glycogen storage.

Hepatic *Slc25a47* deficiency leads to impaired respiration

We next interrogated if a chronic energy deficiency in *Slc25a47*^{hep-/-} hepatocytes due to mitochondrial dysfunction could underlie the broad and diverse metabolic phenotypes observed. In line with this assumption, ATP levels were strongly diminished in the livers of fed and fasted 8-week-old *Slc25a47*^{hep-/-} male mice (Fig. 3A) suggesting impaired oxidative phosphorylation. To assess the role of the *Slc25a47* locus in mitochondrial function, we performed high-resolution respirometry assays on liver lysates and isolated mitochondria from fed and fasted *Slc25a47*^{hep-/-} males. We used a combination of drugs and substrates to assess different respiration states

(Fig. 3B). Compared to fed or fasted *Slc25a47*^{hep+/+} livers, mitochondria isolated from *Slc25a47*^{hep-/-} livers respired significantly less, even in the presence of the complex I inhibitor, rotenone (Fig. 3C-F; S3A). The defect in respiration did not appear to be restricted to any given complex or limited to coupled or uncoupled respiration. In line with our cellular data (Fig. S1C-F), addition of the chemical uncoupling agent FCCP failed to rescue the respiratory phenotype observed in mitochondria isolated from *Slc25a47*^{hep-/-} livers. We then extended these results by assessing the fatty acid oxidation potential of *Slc25a47*^{hep-/-} mitochondria and found that palmitoyl- and octanoyl-carnitine-driven respiration was also severely impaired in mitochondria extracted from *Slc25a47*^{hep-/-} livers (Fig. 3G). Taken together, our results demonstrate that *Slc25a47*^{hep-/-} livers suffer from a shortage of cellular ATP as a consequence of impaired respiration most likely arising from a global mitochondrial defect.

***Slc25a47* deficiency leads to a strong induction of the mitochondrial stress response**

We then performed RNA-seq analysis on livers from fasted 9-week-old male *Slc25a47*^{hep-/-} and *Slc25a47*^{hep+/+} mice. Principal component analysis revealed a strong separation between the 2 genotypes suggesting robust transcriptional changes induced by loss of *Slc25a47* (Fig. 4A). Gene set enrichment analysis indicated that the mitochondrial stress response (MSR) was the most significantly enriched signature (Fig. 4B). The MSR is a highly conserved pathway triggered by various mitochondrial stressors that activate a wide range of factors to restore normal mitochondrial function.¹⁶ Accordingly, the transcriptome of *Slc25a47*^{hep-/-} livers was characterized by a strong upregulation of mitochondrial stress markers (Fig. 4C). The MSR encompasses and overlaps with the mitochondrial unfolded protein response (UPR_{mt}), activated to restore protein homeostasis upon mitochondrial protein misfolding.¹⁶⁻¹⁸ RNA and protein levels of the prototypical UPR_{mt}¹⁹ mediators, such as mitochondrial heat shock proteins (*Hspa9*, *Hspd1*, *Hspa1a*) and proteases (*Yme1l1*, *Lonp1*) were robustly induced in *Slc25a47*^{hep-/-} livers (Fig. 4D-E). RNA-seq (Fig. S4A-B), qRT-PCR (Fig. S4C), and immunoblotting (Fig. S4D) analyses confirmed that activation of the MSR was also observed in fed animals. Mitochondrial stress does not only involve cell-autonomous communication from mitochondria to the nucleus, but is also typified by the expression, and secretion, of non-cell-autonomous factors that mediate inter-tissue communication to integrate the cellular mitochondrial stress response within a global metabolic reprogramming of the organism.^{16,20,21} These factors are referred to as mitokines and were first described in invertebrates.^{22,23} In mammals, fibroblast growth factor 21 (FGF21),²⁴⁻²⁷ growth differentiation factor 15²⁸ and adrenomedullin 2^{29,30} are the best characterized. All 3 mitokines were strongly induced in the livers of *Slc25a47*^{hep-/-} mice (Fig. 4C; S4B) but FGF21 seemed to be the main secreted factor, as demonstrated by its plasma levels in both fasted (Fig. 4F) and fed (Fig. S4E) conditions.

FGF21-dependent systemic phenotypes upon loss of *Slc25a47*

Because FGF21 levels were high in *Slc25a47*^{hep-/-} plasma, we examined the molecular link between its induction and the genetic disruption of the *Slc25a47* locus. An *in silico* analysis of the murine *Fgf21* promoter region found putative binding sites for over 30 transcription factors (Fig. S5A). Correlation analyses between their mRNA expression levels and *Fgf21* indicated that the

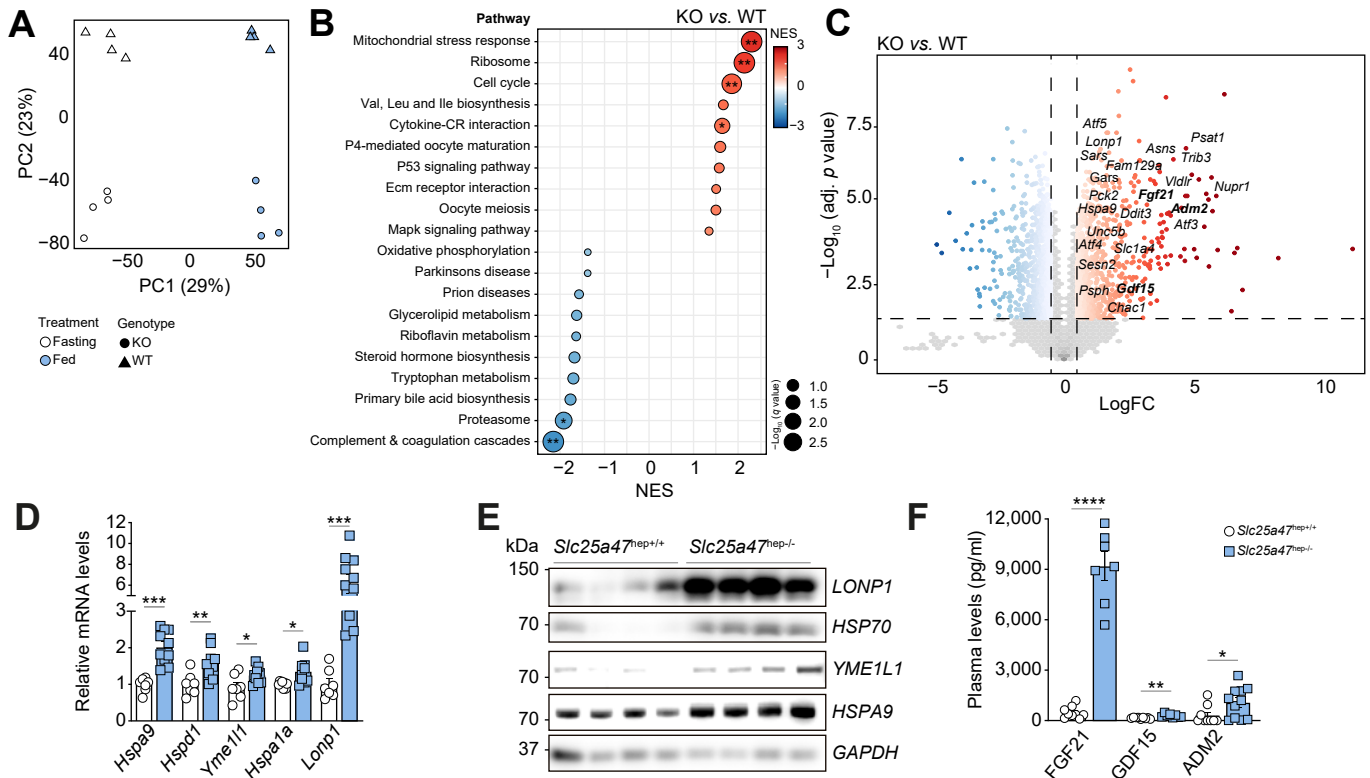


Fig. 4. *Slc25a47* deficiency leads to a strong induction of the mitochondrial stress response. (A) PCA from RNA-seq of livers from fed and fasted 9-week-old *Slc25a47*^{hep+/+} and *Slc25a47*^{hep-/-} mice (n = 4). (B) GSEA from RNA-seq data of fasted *Slc25a47*^{hep-/-} (KO) and *Slc25a47*^{hep+/+} (WT) livers. *q value <0.05, **q value <0.01. (C) Volcano plot of significantly downregulated (blue) and upregulated (red) genes in liver from mice described in panel B. The names represent mitochondrial stress genes. Mitokine genes are in bold. (D, E) Relative gene expression (D, n = 10) and immunoblot (E, n = 4) from livers of fasted 8-week-old KO vs. WT. (F) Plasma quantification of FGF21, GDF15 and ADM2 in fasted 8-week-old mice (n = 7–8). Error bars represent mean \pm SEM. *p <0.05, **p <0.01, ***p <0.001 and ****p <0.0001 relative to *Slc25a47*^{hep+/+} mice, as determined by unpaired Student's *t* test. FC, fold change; GSEA, gene set-enrichment analysis; KO, knockout; NES, normalized enrichment score; PCA, principal component analysis; RNA-seq, RNA-sequencing; WT, wild-type.

stress-induced proteins activating transcription factor (ATF)4 and ATF5 are strongly correlated with *Fgf21*, suggesting a causative link between these transcription factors and the induction of this mitokine (Fig. 5A). This was confirmed by chromatin immunoprecipitation assays, which showed robust recruitment of both ATF4 and ATF5 to the *Fgf21* promoter specifically in *Slc25a47*^{hep-/-} livers (Fig. 5B). Genetic recombination within the *Slc25a47* locus thus leads to an induction of the ATF-FGF21 stress pathway.

FGF21 mediates a multitude of metabolic actions,^{31,32} and its chronic upregulation is known to induce a profound and persistent hypermetabolic state.^{33,34} We hence generated a new mouse line in which both *Slc25a47* and *Fgf21* were genetically ablated in hepatocytes (*Slc25a47-Fgf21*^{hep-/-}); we then phenotyped these mice (Fig. S5B–D). Most of the morphological and systemic phenotypes of *Slc25a47*^{hep-/-} mice were fully rescued in double-mutant mice. In particular, body weight (Fig. 5C) and body length (Fig. 5D; S5E) were normal in 8-week-old male control and *Slc25a47-Fgf21*^{hep-/-} animals but were abnormally reduced in *Slc25a47*^{hep-/-} mice. Food intake (Fig. 5E) on the other hand was markedly increased in *Slc25a47*^{hep-/-} animals but normalized upon double ablation of *Slc25a47* and *Fgf21*. *Slc25a47*^{hep-/-} mice showed marked beiging of subcutaneous white adipose tissue (scWAT, Fig. 5F–G) associated with a strong increase in energy expenditure both during the day and night (Fig. 5H) which was not linked to increased movement activity

(Fig. S5F). In contrast, scWAT beiging and energy expenditure were normal in *Slc25a47-Fgf21*^{hep-/-} animals (Fig. 5F–H). Altogether, these results support a model in which the hepatic mitochondrial stress induced in *Slc25a47*^{hep-/-} livers triggers an FGF21-driven hypermetabolic phenotype in *Slc25a47*^{hep-/-} mice.

FGF21-independent hepatic phenotypes upon loss of *Slc25a47*

Contrary to what we observed at the systemic level, the liver-specific phenotypes of *Slc25a47*^{hep-/-} animals remained after the genetic deletion of *Fgf21*. In particular, 8-week-old male single *Slc25a47*^{hep-/-} and double *Slc25a47-Fgf21*^{hep-/-} mice were similarly affected by a decrease in the liver to body weight ratio (Fig. 6A) and displayed comparable changes in liver triglycerides (Fig. 6B; S6A) and alanine aminotransferase/aspartate aminotransferase (Fig. 6C) levels upon fasting. All phenotypes associated with glucose homeostasis were also independent of FGF21 expression and its induction of scWAT beiging. Indeed, single *Slc25a47*^{hep-/-} and double *Slc25a47-Fgf21*^{hep-/-} mice displayed similarly improved glucose clearance rates during OGTT (Fig. 6D). ITT after mild (6-hour) fasting of the experimental cohorts indicated that, prior to insulin injection, single *Slc25a47*^{hep-/-} and double *Slc25a47-Fgf21*^{hep-/-} mice were already hypoglycemic (Fig. 6E; S6D) but responded similarly to the actions of insulin (Fig. S6B), suggesting normal insulin signaling in *Slc25a47*-deficient animals. We then explored whether the impaired mitochondrial activity in

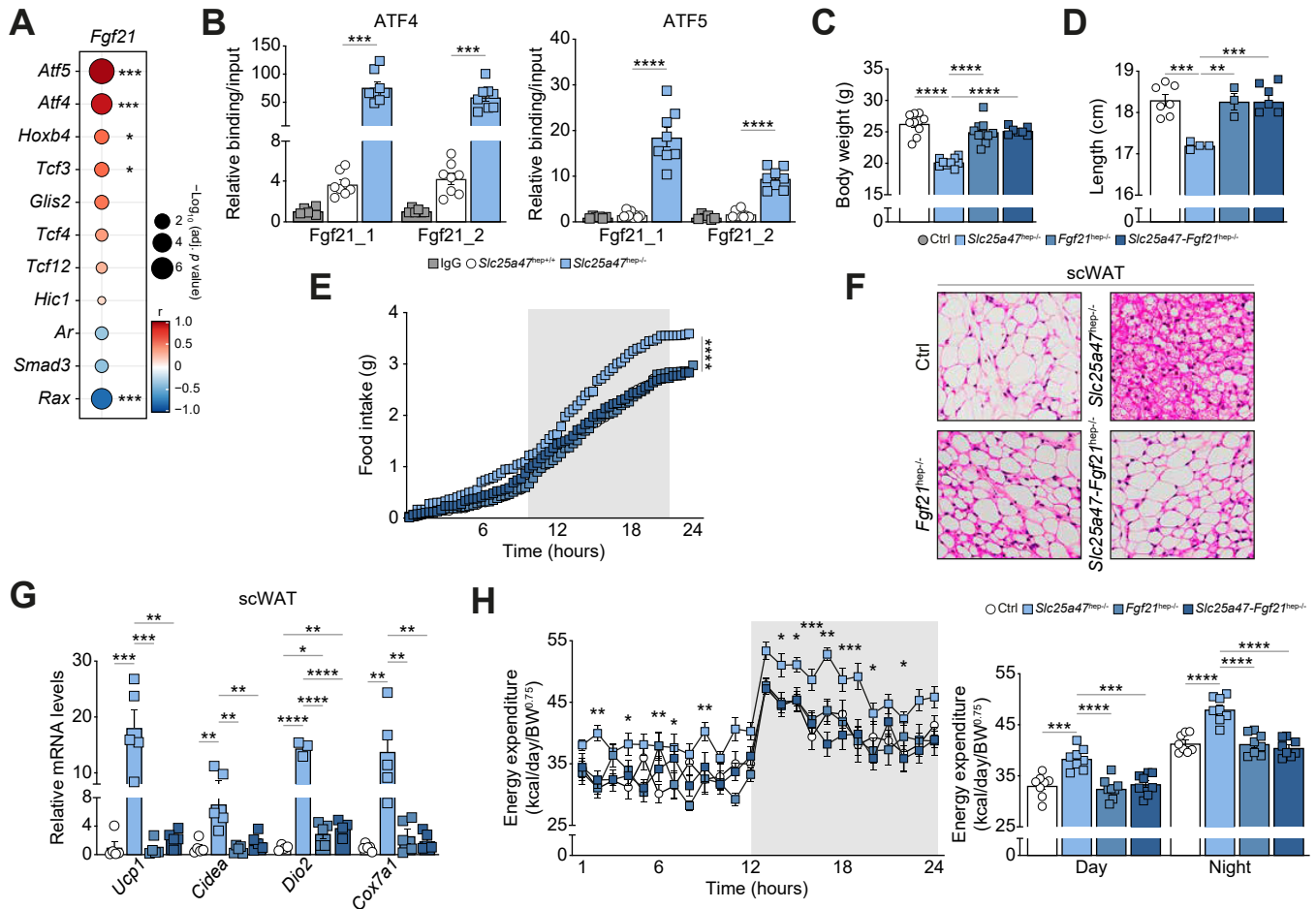


Fig. 5. FGF21-dependent systemic phenotypes upon genetic recombination within the *Slc25a47* locus. (A) Pearson correlation between transcription factors and *Fgf21* obtained using RNA-seq data from livers of fed and fasted *Slc25a47*^{hep+/+} and *Slc25a47*^{hep-/-} mice (n = 8). (B) ChIP assays for ATF4 and ATF5, followed by qPCR on 2 binding sites (*Fgf21_1* and *Fgf21_2*) within the *Fgf21* promoter, in livers of *Slc25a47*^{hep+/+} and *Slc25a47*^{hep-/-} mice (n = 8). (C, D) Body weight (C, n = 7-10) and length (D, n = 3-7) of 8-week-old fasted control (Ctrl), *Slc25a47*^{hep-/-}, *Fgf21*^{hep-/-} and *Slc25a47*^{hep-/-}; *Fgf21*^{hep-/-} mice. (E) Cumulative food intake (24 h) of 17-week-old Ctrl, *Slc25a47*^{hep-/-}, *Fgf21*^{hep-/-} and *Slc25a47*^{hep-/-}; *Fgf21*^{hep-/-} mice (n = 8). The rectangle represents the dark phase. (F, G) H&E staining (F) and relative transcript levels of beiging markers (G, n = 5) in scWAT from mice described in panel C. Scale bar: 20 μ m. (H) Energy expenditure in 13-week-old Ctrl, *Slc25a47*^{hep-/-}, *Fgf21*^{hep-/-} and *Slc25a47*^{hep-/-}; *Fgf21*^{hep-/-} mice (n = 8). The rectangle represents the dark phase. Error bars represent mean \pm SEM. **p* < 0.05, ***p* < 0.01, ****p* < 0.001 and *****p* < 0.0001, as determined by one-way ANOVA and Tukey's multiple comparison test (B-D, G) or two-way ANOVA and Bonferroni *post hoc* correction (E, H). Asterisks in (E, H) represent *Slc25a47*^{hep-/-} vs. Ctrl. scWAT, subcutaneous white adipose tissue.

SLC25A47-depleted livers forces hepatocytes to rely more on glycolytic metabolism. In line with this hypothesis, ATP levels were robustly reduced in both single *Slc25a47*^{hep-/-} and double *Slc25a47*^{hep-/-}; *Fgf21*^{hep-/-} livers (Fig. 6F). Moreover, ablation of *Fgf21* in *Slc25a47*^{hep-/-} mice failed to rescue the defects in respiration (Fig. 6G-H). Both mouse lines also displayed elevated plasma lactate levels during OGTT (Fig. S6C). Additionally, the glycemic excursion after oral pyruvate administration (PTT, Fig. 6I) was no longer observed in single *Slc25a47*^{hep-/-} and double *Slc25a47*^{hep-/-}; *Fgf21*^{hep-/-} mice, suggesting that ATP depletion in the liver of *Slc25a47*^{hep-/-} mice impairs normal gluconeogenesis, a hypothesis in line with the fasting-induced hypoglycemia observed in both *Slc25a47*^{hep-/-} and *Slc25a47*^{hep-/-}; *Fgf21*^{hep-/-} mice (Fig. S6D). Collectively, these data demonstrate that deletion of *Slc25a47* has a broad metabolic impact not only in the liver, but also on the whole organism. While several of the hypermetabolic phenotypes could be attributed to chronic FGF21 signaling, those involved in glycemic control remain defective, even after removal of FGF21.

Slc25a47^{hep-/-} mice develop liver fibrosis

To gain insights into the mechanism leading to liver injury in *Slc25a47*^{hep-/-} mice (Fig. 2G; S2E-F), we performed *in silico* cell type enrichment analysis with our RNA-seq data (Fig. 7A). More inflammatory cells were present in *Slc25a47*^{hep-/-} livers along with an upregulation of stellate cells (Fig. 7A) suggesting a pre-disposition to fibrosis. We hence performed Sirius Red staining on livers of young (8 weeks), mid-aged (32 weeks), and old (80 weeks) *Slc25a47*^{hep-/-} mice and control littermates. Collagen deposition was significantly increased upon aging in *Slc25a47*^{hep-/-} livers, as shown by Sirius Red staining (Fig. S7A). We then challenged *Slc25a47*^{hep-/-} animals with a HFHS diet to further exacerbate the metabolic pressure in the liver. While *Slc25a47*^{hep-/-} mice were significantly protected against HFHS-induced obesity (Fig. S7B) and diabetes (Fig. 7D-F, S7C) as a result of their increased energy expenditure (Fig. 5H) and improved glycemic profile (Fig. 6), their livers were much more inflamed than control littermates and displayed fibrosis (Fig. 7B-C; S7D). These molecular and histological markers indicate that *Slc25a47*^{hep-/-}

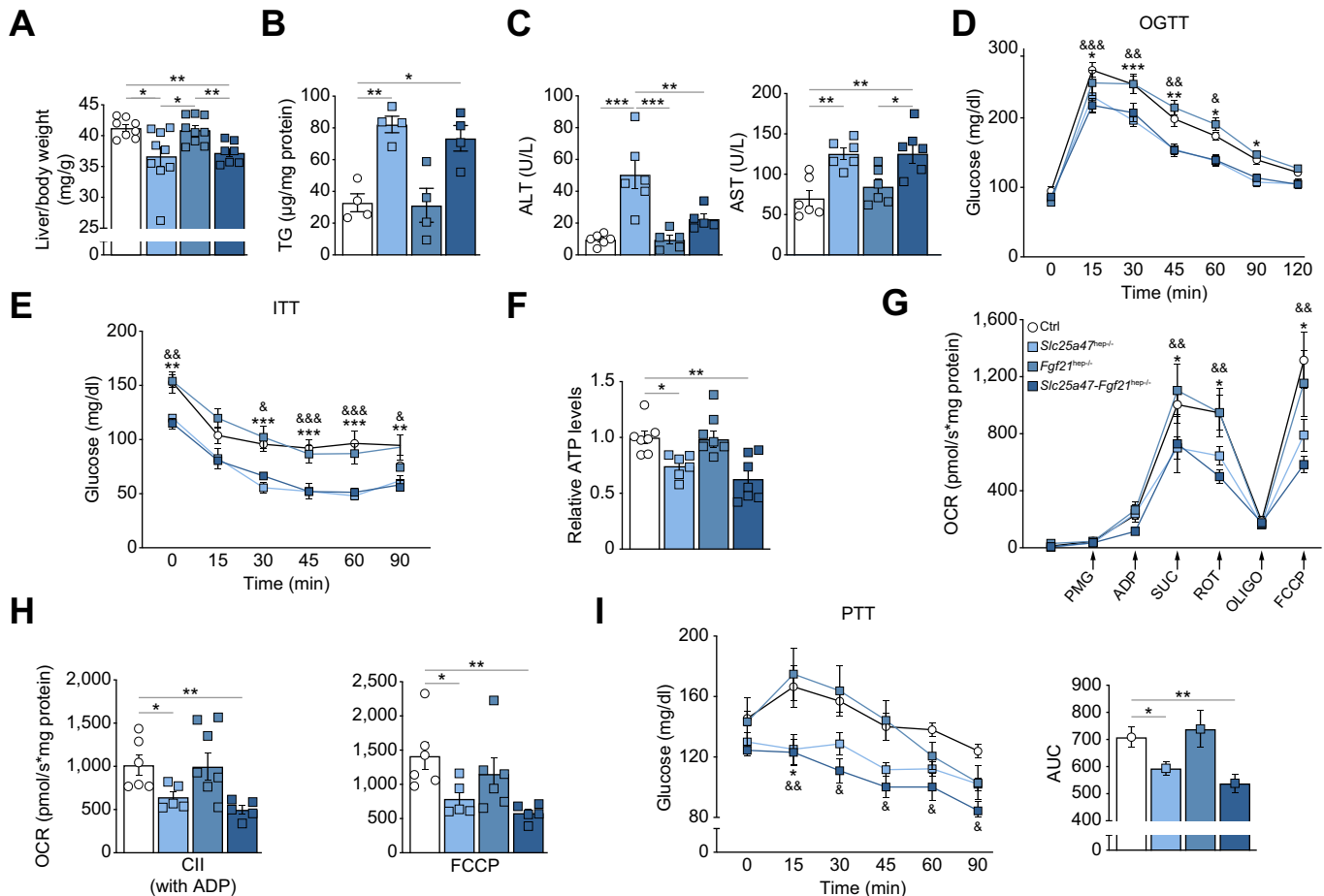


Fig. 6. *Slc25a47-Fgf21*^{hep-/-} mice present FGF21-independent phenotypes. (A) Liver weight over body weight in fasted 8-week-old Ctrl, *Slc25a47*^{hep-/-}, *Fgf21*^{hep-/-} and *Slc25a47-Fgf21*^{hep-/-} mice (n = 7-9). (B) Hepatic TG content in mice described in panel A (n = 4). (C) Plasma levels of ALT and AST in 22-week-old fasted mice (n = 6). (D-E) Blood glucose levels during OGTT (D) and IIT (E) in 12- and 15-week-old mice (n = 8). (F) Relative ATP levels from fasted livers described in panel A (n = 6-7). (G, H) Time course (G) and bar graphs (H) representing OCR of freshly isolated mitochondria from fasted livers described in panel A (n = 5-6). (I) Blood glucose levels during intraperitoneal PTT in 20-week-old mice (n = 8). Error bars represent mean ± SEM. A-C, F, H: *p < 0.05, **p < 0.01 and ***p < 0.001 as determined by one-way ANOVA and Tukey's multiple comparison test. D, E, G, I: *p < 0.05, **p < 0.01 and ***p < 0.001 for *Slc25a47*^{hep-/-} vs. Ctrl; &p < 0.05, &&p < 0.01 and &&&p < 0.001 for *Slc25a47-Fgf21*^{hep-/-} vs. Ctrl as determined by two-way ANOVA and Bonferroni *post hoc* correction. IIT, insulin tolerance test; OCR, oxygen consumption rate; OGTT, oral glucose tolerance test; PTT, pyruvate tolerance test; TG, triglyceride.

mice are predisposed to develop non-alcoholic steatohepatitis and liver fibrosis.

Discussion

The liver is one of the first organs to respond to dietary factors³⁵ and its mitochondria demonstrate high metabolic flexibility to coordinate the changes in bioenergetic demand.³⁶ We observed that loss-of-function of the *Slc25a47* locus impaired hepatocyte mitochondrial function and, in turn, rendered *Slc25a47*^{hep-/-} mice metabolically inflexible as demonstrated by their blunted ability to switch to lipid oxidation in the fasted state. The chronic energy deficit also led to impaired gluconeogenesis and faster depletion of the glycogen stores in the fed state. Overall, these phenotypes underlie the observed hypoglycemia, even after mild fasting. Moreover, *Slc25a47*^{hep-/-} mice suffered from liver damage preponderantly in the fasted state suggesting that *Slc25a47*-deficient hepatocytes fail to cope with the additional metabolic pressure induced by fasting or HFHS feeding. While our study used a design based on a genetic and liver-specific recombination of the *Slc25a47* locus which, surely, maximizes the negative

effects on hepatic homeostasis, a milder inhibition of SLC25A47 could prove interesting from a therapeutic perspective. Our data show that one of the main consequences of SLC25A47 down-regulation is an inhibition of the hepatic ETC, which results in impaired gluconeogenesis. This mechanism of action is reminiscent of that of metformin, the most frequently prescribed antidiabetic treatment,³⁷ which reduces hepatic gluconeogenesis through moderate inhibition of complex I.³⁷ Theoretically, a mild inhibition of SLC25A47 could hamper the ETC specifically in hepatocytes and lower glycemia by blunting *de novo* glucose production. In line with this hypothesis, we observed that heterozygous *Slc25a47*^{hep+/-} mice did not show signs of liver damage or metabolic stress but secreted less glucose in response to pyruvate (Fig. S2M). This putative therapeutic application remains to be tested under several conditions of metabolic pressure, but is an example of how a better understanding of mitochondrial carriers, and of their specific tissue distribution, could be leveraged to treat metabolic disorders.³ It should be noted, however, that SLC25A47 was first identified as a gene downregulated during hepatocellular carcinoma development.¹⁵ This finding

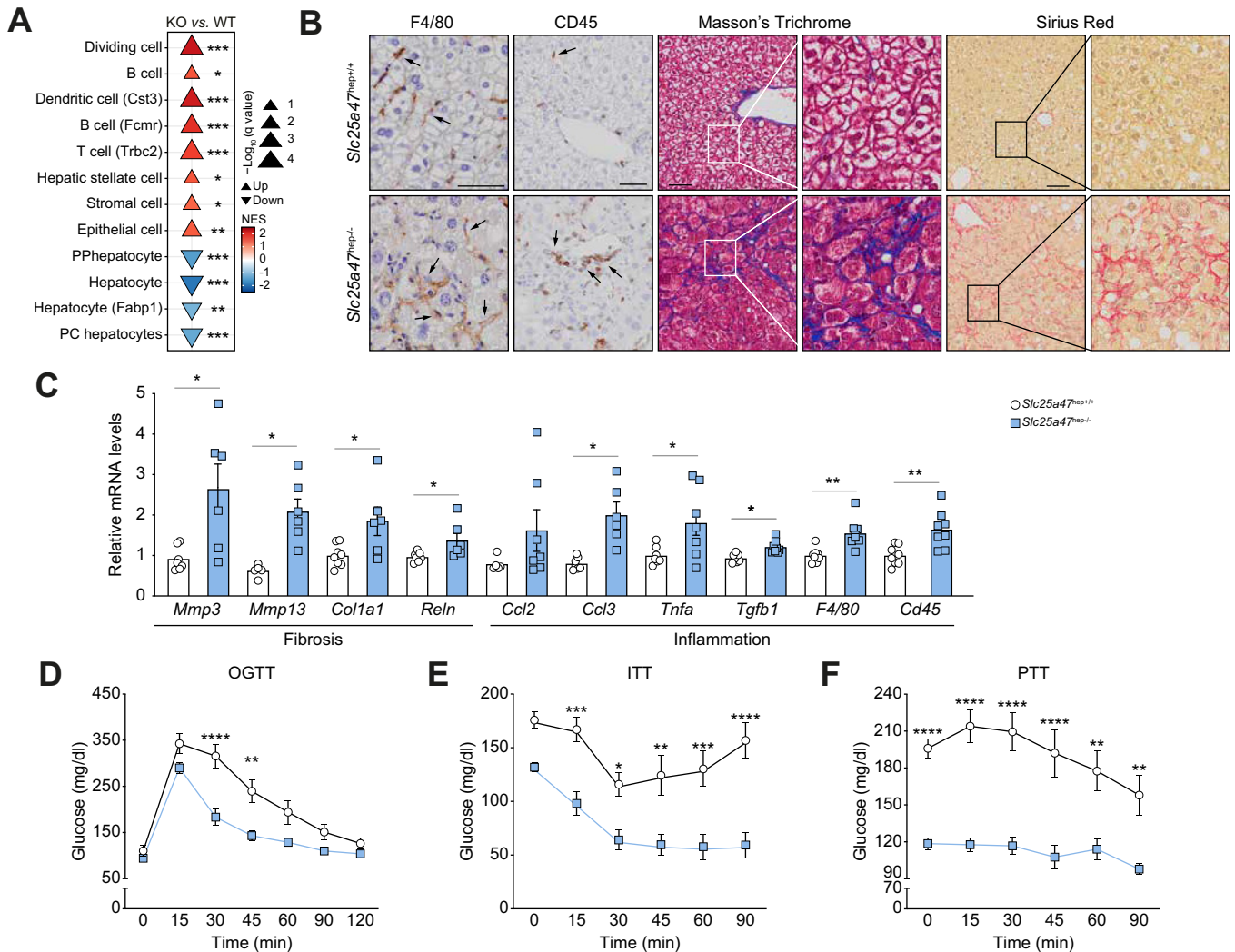


Fig. 7. *Slc25a47*^{hep-/-} mice develop liver fibrosis. (A) Cell type enrichment analysis from fed and fasted 8-week-old *Slc25a47*^{hep-/-} (KO) and *Slc25a47*^{hep+/+} (WT) livers. (B) Representative images of hepatic tissue stained for F4/80 and CD45 positive cells, Masson's trichrome, and Sirius red in HFHS diet fed *Slc25a47*^{hep+/+} and *Slc25a47*^{hep-/-} mice (22-week-old). Mice were fed HFHS diet for 14 weeks. Scale bars: 50 μ m. Arrows indicate F4/80 and CD45 positive cells. (C) Relative transcript levels of fibrosis and inflammation markers in 22-week-old HFHS diet fed *Slc25a47*^{hep+/+} and *Slc25a47*^{hep-/-} livers (n = 6-8). (D-F) Blood glucose levels during OGTT (D), ITT (E) and PTT (F) in 12-, 15-, 20-week-old *Slc25a47*^{hep+/+} and *Slc25a47*^{hep-/-} mice (n = 8). Error bars represent mean \pm SEM. *p/q<0.05, **p/q<0.01, ***p/q<0.001 and ****p/q<0.0001, as determined by unpaired Student's t test (C) or two-way ANOVA and Bonferroni post hoc correction (D-F). HFHS, high-fat high-sucrose; ITT, insulin tolerance test; KO, knockout; OGTT, oral glucose tolerance test; PTT, pyruvate tolerance test; WT, wild-type.

calls for a cautious monitoring of SLC25A47 inhibition with regard to cancer progression.

Our data show that the *Slc25a47* locus is essential to maintain hepatic mitochondrial homeostasis as its disruption results in the activation of a profound and persistent MSR. Mitochondrial stress induces mitochondrial quality control mechanisms that are essential to maintain mitochondrial function.¹⁶ Retrograde signals from the mitochondria to the nucleus have been well-documented in multiple species^{38,39} and involve the induction of transcription factors, including ATF4,³⁹⁻⁴¹ ATF5⁴² CHOP (C/EBP homologous protein^{43,44}), and C/EBP β .^{43,44} Alongside these cell-autonomous effectors, non-cell-autonomous factors are also secreted, enabling the MSR to rewire organismal metabolic homeostasis.^{16,20-22,24,45} In this study, we demonstrated that FGF21 is a key hepatic mitokine that modulates systemic energy metabolism in *Slc25a47*^{hep-/-} mice. Persistent activation of the

ATF family most likely contributes to the marked increase of plasma FGF21 levels in *Slc25a47*^{hep-/-} mice.⁴⁶ We demonstrated that this induction mediates a profound hypermetabolic state, driving increased scWAT beiging, energy expenditure, hyperphagia, and blunted growth, the latter most likely resulting from the chronic hypermetabolism observed in *Slc25a47*^{hep-/-} mice.

The MSR is normally activated by defects in mitonuclear protein imbalance, such as seen with defects in mtDNA replication,^{45,47,48} in the ETC,^{22,39} in mito-ribosomal translation^{18,21} or upon mitochondrial biogenesis.^{17,49} Here we linked the activation of the MSR with the loss of a mitochondrial carrier. Involvement of mitochondrial carriers in mitochondrial stress, however, is not unprecedented, as an early study attempting to define the MSR in *Arabidopsis thaliana* already reported that the SLC25 family was over-represented amongst stress-responsive genes.⁵⁰ While this study suggests that mitochondrial stress

resolution involves a rewiring of metabolite trafficking across mitochondrial membranes,⁵⁰ it will be interesting to determine to what extent depletion or accumulation of given metabolites can trigger mitochondrial stress. Our work suggests that SLC25A47 controls the levels of a mitochondrial metabolite, the nature of which is currently unknown and requires further investigation given its potential impact on hepatocyte mitochondrial function, liver fibrosis, and organismal health.

While genetic disruption of the *Slc25a47* locus improves the metabolic profile of mice on an obesogenic, diabetogenic diet, this is achieved at the expense of liver health and integrity, as exemplified by the pronounced fibrotic phenotype induced progressively upon aging or acutely under the metabolic pressure of an HFHS diet. Fibrosis is a common pathological feature of most end-stage organ diseases and growing evidence indicates that mitochondrial dysfunction contributes to the development and progression of fibrosis in a number of organs (reviewed in⁵¹). Our observations indicate that SLC25A47 could be a promising target to mitigate this process in the liver. Further studies will be needed to further explore in-depth its role in liver fibrogenesis.

Abbreviations

ATF, activating transcription factor; EM, electron microscopy; ETC, electron transport chain; FC, fold change; FGF21, fibroblast growth factor 21; HFHS, high-fat high-sucrose, ITT, insulin tolerance test; MSR, mitochondrial stress response; OCR, oxygen consumption rate; OGTT, oral glucose tolerance test; PTT, pyruvate tolerance test; RT-qPCR, reverse-transcription quantitative PCR; scWAT: subcutaneous white adipose tissue; UPRmt, mitochondrial unfolded protein response.

Financial support

This work was supported by the Ecole Polytechnique Fédérale de Lausanne (EPFL to K.S. & J.A.), and grants from the Swiss National Science Foundation, Switzerland (SNSF 31003 A_166695 to K.S., SNSF 31003A-179435 to J.A.), the European Research Council (ERC-AdG-787702 to J.A.), the Swiss Cancer League (KFS-4226-08-2017 to K.S.), and the Global Research Laboratory (GRL) National Research Foundation of Korea (NRF 2017K1A1A2013124 to J.A.). H.D. received funding from the European Union's Horizon 2020 research and innovation program under the Marie Skłodowska-Curie grant agreement No 846001.

Conflict of interest

The authors declare no conflicts of interest that pertain to this work.

Please refer to the accompanying ICMJE disclosure forms for further details.

Authors' contributions

K.S. conceived, designed, and supervised the project. N.B., H.D., V.L., F.P. and A.P. performed animal experiments. N.B. performed *in vitro* experiments. X.L. analyzed the RNA-seq data. H.L. analyzed the scRNA-seq data. Y.S. performed ChIP experiments. J.A. provided expertise and funding. N.B., H.D., and K.S. wrote the manuscript.

Data availability statement

The data associated with this paper are available upon request to the corresponding author. Reagents, antibodies and resources are

listed in the material and methods section, supplementary materials and methods and in the CTAT table.

Acknowledgments

We thank the Schoonjans and Auwerx lab members, in particular Sabrina Bichet, Thibaud Clerc, Jérôme Imbach, Kim Borany, Fabiana Fraga, Marie Janod, Carla Mendes Ferreira, Penelope Stefanelli, as well as the EPFL-SV animal facility (UDP), the histology facility (HCF) and the electron microscopy facility (BioEM) for technical assistance. We thank Maroun Bou Sleiman for his assistance with the graphical abstract.

Supplementary data

Supplementary data to this article can be found online at <https://doi.org/10.1016/j.jhep.2022.05.040>.

References

Author names in bold designate shared co-first authorship

- [1] Hinzpeter F, Gerland U, Tostevin F. Optimal compartmentalization strategies for metabolic microcompartments. *Biophys J* 2017;112:767–779.
- [2] Pfaff E, Klingenberg M, Ritt E, Vogell W. Correlation of the unspecific permeable mitochondrial space with the "intermembrane space". *Eur J Biochem* 1968;5:222–232.
- [3] Palmieri F. The mitochondrial transporter family SLC25: identification, properties and physiopathology. *Mol Aspects Med* 2013;34:465–484.
- [4] Galgani JE, Moro C, Ravussin E. Metabolic flexibility and insulin resistance. *Am J Physiol Endocrinol Metab* 2008;295:E1009–E1017.
- [5] Schimke RT, Doyle D. Control of enzyme levels in animal tissues. *Annu Rev Biochem* 1970;39:929–976.
- [6] Frezza C, Cipolat S, Scorrano L. Organelle isolation: functional mitochondria from mouse liver, muscle and cultured fibroblasts. *Nat Protoc* 2007;2:287–295.
- [7] Gutierrez-Aguilar M, Baines CP. Physiological and pathological roles of mitochondrial SLC25 carriers. *Biochem J* 2013;454:371–386.
- [8] Sollner JF, Leparc G, Hildebrandt T, Klein H, Thomas L, Stupka E, et al. An RNA-Seq atlas of gene expression in mouse and rat normal tissues. *Sci Data* 2017;4:170185.
- [9] Fiermonte G, Palmieri L, Todisco S, Agrimi G, Palmieri F, Walker JE. Identification of the mitochondrial glutamate transporter. Bacterial expression, reconstitution, functional characterization, and tissue distribution of two human isoforms. *J Biol Chem* 2002;277:19289–19294.
- [10] Su AI, Cooke MP, Ching KA, Hakak Y, Walker JR, Wiltshire T, Orth AP, et al. Large-scale analysis of the human and mouse transcriptomes. *Proc Natl Acad Sci U S A* 2002;99:4465–4470.
- [11] Tabula Muris C, Overall c, Logistical c, Organ c, processing Library p, sequencing, et al. Single-cell transcriptomics of 20 mouse organs creates a Tabula Muris. *Nature* 2018;562:367–372.
- [12] Halpern KB, Shenhav R, Matcovitch-Natan O, Toth B, Lemze D, Golan M, et al. Single-cell spatial reconstruction reveals global division of labour in the mammalian liver. *Nature* 2017;542:352–356.
- [13] Li H, Rukina D, David FPA, Li TY, Oh CM, Gao AW, et al. Identifying gene function and module connections by the integration of multispecies expression compendia. *Genome Res* 2019;29:2034–2045.
- [14] Jin X, Yang YD, Chen K, Lv ZY, Zheng L, Liu YP, et al. HDMCP uncouples yeast mitochondrial respiration and alleviates steatosis in L02 and hepG2 cells by decreasing ATP and H2O2 levels: a novel mechanism for NAFLD. *J Hepatol* 2009;50:1019–1028.
- [15] Tan MG, Ooi LL, Aw SE, Hui KM. Cloning and identification of hepatocellular carcinoma down-regulated mitochondrial carrier protein, a novel liver-specific uncoupling protein. *J Biol Chem* 2004;279:45235–45244.
- [16] Mottis A, Herzig S, Auwerx J. Mitochondrial communication: shaping health and disease. *Science* 2019;366:827–832.
- [17] Mouchiroud L, Houtkooper RH, Moullan N, Katsyuba E, Ryu D, Canto C, et al. The NAD(+)/Sirtuin pathway modulates longevity through activation of mitochondrial UPR and FOXO signaling. *Cell* 2013;154:430–441.
- [18] Houtkooper RH, Mouchiroud L, Ryu D, Moullan N, Katsyuba E, Knott G, et al. Mitonuclear protein imbalance as a conserved longevity mechanism. *Nature* 2013;497:451–457.

- [19] Jovaisaite V, Mouchiroud L, Auwerx J. The mitochondrial unfolded protein response, a conserved stress response pathway with implications in health and disease. *J Exp Biol* 2014;217:137–143.
- [20] Quiros PM, Mottis A, Auwerx J. Mitonuclear communication in homeostasis and stress. *Nat Rev Mol Cell Biol* 2016;17:213–226.
- [21] Kang SG, Choi MJ, Jung SB, Chung HK, Chang JY, Kim JT, et al. Differential roles of GDF15 and FGF21 in systemic metabolic adaptation to the mitochondrial integrated stress response. *iScience* 2021;24:102181.
- [22] Durieux J, Wolff S, Dillin A. The cell-non-autonomous nature of electron transport chain-mediated longevity. *Cell* 2011;144:79–91.
- [23] Copeland JM, Cho J, Lo Jr T, Hur JH, Bahadorani S, Arabyan T, et al. Extension of *Drosophila* life span by RNAi of the mitochondrial respiratory chain. *Curr Biol* 2009;19:1591–1598.
- [24] Kim KH, Jeong YT, Oh H, Kim SH, Cho JM, Kim YN, et al. Autophagy deficiency leads to protection from obesity and insulin resistance by inducing Fgf21 as a mitokine. *Nat Med* 2013;19:83–92.
- [25] Chau MD, Gao J, Yang Q, Wu Z, Gromada J. Fibroblast growth factor 21 regulates energy metabolism by activating the AMPK-SIRT1-PGC-1 α pathway. *Proc Natl Acad Sci U S A* 2010;107:12553–12558.
- [26] Tyynismaa H, Carroll CJ, Raimundo N, Ahola-Erkkila S, Wenz T, Ruhanen H, et al. Mitochondrial myopathy induces a starvation-like response. *Hum Mol Genet* 2010;19:3948–3958.
- [27] Klier SA, Mangelsdorf DJ. A dozen years of discovery: insights into the Physiology and pharmacology of FGF21. *Cell Metab* 2019;29:246–253.
- [28] Chung HK, Ryu D, Kim KS, Chang JY, Kim YK, Yi HS, et al. Growth differentiation factor 15 is a myomitokine governing systemic energy homeostasis. *J Cell Biol* 2017;216:149–165.
- [29] Lv Y, Zhang SY, Liang X, Zhang H, Xu Z, Liu B, et al. Adrenomedullin 2 enhances beige in white adipose tissue directly in an adipocyte-autonomous manner and indirectly through activation of M2 macrophages. *J Biol Chem* 2016;291:23390–23402.
- [30] Zhang SY, Lv Y, Zhang H, Gao S, Wang T, Feng J, et al. Adrenomedullin 2 improves early obesity-induced adipose insulin resistance by inhibiting the class II MHC in adipocytes. *Diabetes* 2016;65:2342–2355.
- [31] Kharitonov A, Shiyanova TL, Koester A, Ford AM, Micanovic R, Galbreath EJ, et al. FGF-21 as a novel metabolic regulator. *J Clin Invest* 2005;115:1627–1635.
- [32] Xu J, Lloyd DJ, Hale C, Stanislaus S, Chen M, Sivits G, et al. Fibroblast growth factor 21 reverses hepatic steatosis, increases energy expenditure, and improves insulin sensitivity in diet-induced obese mice. *Diabetes* 2009;58:250–259.
- [33] Inagaki T, Lin VY, Goetz R, Mohammadi M, Mangelsdorf DJ, Klier SA. Inhibition of growth hormone signaling by the fasting-induced hormone FGF21. *Cell Metab* 2008;8:77–83.
- [34] Owen BM, Ding X, Morgan DA, Coate KC, Bookout AL, Rahmouni K, et al. FGF21 acts centrally to induce sympathetic nerve activity, energy expenditure, and weight loss. *Cell Metab* 2014;20:670–677.
- [35] Kraegen EW, Clark PW, Jenkins AB, Daley EA, Chisholm DJ, Storlien LH. Development of muscle insulin resistance after liver insulin resistance in high-fat-fed rats. *Diabetes* 1991;40:1397–1403.
- [36] Koliaki C, Roden M. Alterations of mitochondrial function and insulin sensitivity in human obesity and diabetes mellitus. *Annu Rev Nutr* 2016;36:337–367.
- [37] Pernicova I, Korbonits M. Metformin—mode of action and clinical implications for diabetes and cancer. *Nat Rev Endocrinol* 2014;10:143–156.
- [38] Cagin U, Enriquez JA. The complex crosstalk between mitochondria and the nucleus: what goes in between? *Int J Biochem Cell Biol* 2015;63:10–15.
- [39] Quiros PM, Prado MA, Zamboni N, D'Amico D, Williams RW, Finley D, et al. Multi-omics analysis identifies ATF4 as a key regulator of the mitochondrial stress response in mammals. *J Cell Biol* 2017;216:2027–2045.
- [40] Bao XR, Ong S-E, Goldberger O, Peng J, Sharma R, Thompson DA, et al. Mitochondrial dysfunction remodels one-carbon metabolism in human cells. *elife* 2016;5:e10575.
- [41] Münch C, Harper JW. Mitochondrial unfolded protein response controls matrix pre-RNA processing and translation. *Nature* 2016;534:710–713.
- [42] Fiorese CJ, Schulz AM, Lin Y-F, Rosin N, Pellegrino MW, Haynes CM. The transcription factor ATF5 mediates a mammalian mitochondrial UPR. *Curr Biol* 2016;26:2037–2043.
- [43] Aldridge JE, Horibe T, Hoogenraad NJ. Discovery of genes activated by the mitochondrial unfolded protein response (mtUPR) and cognate promoter elements. *PLoS one* 2007;2:e874.
- [44] Zhao Q, Wang J, Levichkin IV, Stasinopoulos S, Ryan MT, Hoogenraad NJ. A mitochondrial specific stress response in mammalian cells. *EMBO J* 2002;21:4411–4419.
- [45] Forsstrom S, Jackson CB, Carroll CJ, Kuronen M, Pirinen E, Pradhan S, et al. Fibroblast growth factor 21 drives dynamics of local and systemic stress responses in mitochondrial myopathy with mtDNA deletions. *Cell Metab* 2019;30:1040–1054 e1047.
- [46] De Sousa-Coelho AL, Marrero PF, Haro D. Activating transcription factor 4-dependent induction of FGF21 during amino acid deprivation. *Biochem J* 2012;443:165–171.
- [47] Martinus RD, Garth GP, Webster TL, Cartwright P, Naylor DJ, Hoj PB, et al. Selective induction of mitochondrial chaperones in response to loss of the mitochondrial genome. *Eur J Biochem* 1996;240:98–103.
- [48] Khan NA, Nikkanen J, Yatsuga S, Jackson C, Wang L, Pradhan S, et al. mTORC1 regulates mitochondrial integrated stress response and mitochondrial myopathy progression. *Cell Metab* 2017;26:419–428 e415.
- [49] Zhang H, Ryu D, Wu Y, Gariani K, Wang X, Luan P, et al. NAD(+) repletion improves mitochondrial and stem cell function and enhances life span in mice. *Science* 2016;352:1436–1443.
- [50] Van Aken O, Zhang B, Carrie C, Uggalla V, Paynter E, Giraud E, et al. Defining the mitochondrial stress response in *Arabidopsis thaliana*. *Mol Plant* 2009;2:1310–1324.
- [51] Li X, Zhang W, Cao Q, Wang Z, Zhao M, Xu L, et al. Mitochondrial dysfunction in fibrotic diseases. *Cell Death Discov* 2020;6:80.



Central anorexigenic actions of bile acids are mediated by TGR5

Alessia Perino¹, Laura. A. Velázquez-Villegas^{1,10}, Nadia Bresciani¹, Yu Sun¹, Qingyao Huang¹, Valérie S. Fénelon², Ashley Castellanos-Jankiewicz², Philippe Zizzari², Giuseppe Bruschetta³, Sungho Jin⁴, Aiste Baleisyte⁵, Antimo Gioiello⁶, Roberto Pellicciari⁷, Julijana Ivanisevic⁸, Bernard L. Schneider⁹, Sabrina Diano^{3,4}, Daniela Cota² and Kristina Schoonjans¹✉

Bile acids (BAs) are signalling molecules that mediate various cellular responses in both physiological and pathological processes. Several studies report that BAs can be detected in the brain¹, yet their physiological role in the central nervous system is still largely unknown. Here we show that postprandial BAs can reach the brain and activate a negative-feedback loop controlling satiety in response to physiological feeding via TGR5, a G-protein-coupled receptor activated by multiple conjugated and unconjugated BAs² and an established regulator of peripheral metabolism^{3–8}. Notably, peripheral or central administration of a BA mix or a TGR5-specific BA mimetic (INT-777) exerted an anorexigenic effect in wild-type mice, while whole-body, neuron-specific or agouti-related peptide neuronal TGR5 deletion caused a significant increase in food intake. Accordingly, orexigenic peptide expression and secretion were reduced after short-term TGR5 activation. In vitro studies demonstrated that activation of the Rho-ROCK-actin-remodelling pathway decreases orexigenic agouti-related peptide/neuropeptide Y (AgRP/NPY) release in a TGR5-dependent manner. Taken together, these data identify a signalling cascade by which BAs exert acute effects at the transition between fasting and feeding and prime the switch towards satiety, unveiling a previously unrecognized role of physiological feedback mediated by BAs in the central nervous system.

Primary BAs are synthesized in the liver from cholesterol and chemically transformed into secondary BAs by the gut microbiota⁸. After feeding, circulating BA levels can reach micromolar concentrations through enterohepatic recirculation and spillover in the systemic circulation⁹. The presence of BAs in the brain has been reported under both physiological and pathological conditions in rodents and humans^{1,10–12}. Although some of the cholesterol and BA biosynthetic enzymes are expressed in different regions of the brain¹³, these proteins seem to be involved in cholesterol clearance rather than in BA production¹⁴. Brain BAs strongly correlate with circulating levels and are believed to reach the central nervous system (CNS) through passive diffusion¹⁰. Despite this evidence, a physiological role of BAs in the CNS has not been reported.

The recent finding that the main non-genomic BA signalling mediator TGR5 (*Gpbar1*) is expressed in the CNS^{15,16} led us to hypothesize that BAs may exert dedicated CNS functions.

Interestingly, we observed that BAs can reach the hypothalamus, the main central regulator of energy homeostasis, after physiological feeding. The hypothalamic concentration of several endogenous BAs, mainly the tauro-conjugated species, was transiently increased following food intake at the beginning of the dark phase (Fig. 1a). Oral administration of a BA mix effectively reduced 24-h food intake (Fig. 1b) suggesting that the feeding-mediated increase in BAs in the CNS may trigger satiety during the fasting–feeding transition through the activation of a BA receptor. Time-course and dose-response studies confirmed that orally administered BAs can rapidly reach the hypothalamus (Extended Data Fig. 1a) and suppress food intake in wild-type mice (Extended Data Fig. 1b). Based on these rapid responses, we reasoned that the anorexigenic phenotype could be mediated by TGR5. Brain expression profiling with RNAscope imaging revealed that endogenous *Gpbar1* mRNA is expressed in different brain regions, including the arcuate nucleus (ARC; Fig. 1c). ARC-enriched hypothalamic punches coupled with quantitative PCR with reverse transcription (RT-qPCR) analysis confirmed that *Gpbar1* is expressed in this brain region, which is critical for the control of food consumption (Extended Data Fig. 1c).

We next gavaged the TGR5-specific semi-synthetic BA INT-777 (refs. 4,17) to investigate whether the BA-mediated anorexigenic effect is TGR5 dependent. Time-course and dose-response experiments confirmed that, like endogenous BAs, INT-777 rapidly accumulated in the hypothalamus (Fig. 1d) and reduced food intake at doses ranging from 10 to 100 mg kg^{−1} (Fig. 1e). At the highest dose, INT-777 reached the hypothalamus at concentrations comparable to those of the endogenous postprandial BAs (Fig. 1a), recapitulating the central physiological concentrations required for BA-mediated feedback regulation of feeding behaviour. Of note, intracerebroventricular (i.c.v.) administration of INT-777 to wild-type mice also caused a rapid and significant anorexigenic response after the first injection (Extended Data Fig. 1d,e) but receded over time, and only a trend towards reduced food intake remained (Extended Data

¹Institute of Bioengineering, Faculty of Life Sciences, Ecole Polytechnique Fédérale de Lausanne, Lausanne, Switzerland. ²University of Bordeaux, INSERM, Neurocentre Magendie, U1215, F-3300, Bordeaux, France. ³Department of Cellular and Molecular Physiology, Yale University School of Medicine, New Haven, CT, USA. ⁴Department of Molecular Pharmacology and Therapeutics, Columbia University Irving Medical Center, New York, NY, USA. ⁵Brain Mind Institute, Ecole Polytechnique Fédérale de Lausanne, Lausanne, Switzerland. ⁶Department of Pharmaceutical Sciences, University of Perugia, Perugia, Italy. ⁷TES Pharma S.r.l., Perugia, Italy. ⁸Metabolomics Platform, Faculty of Biology and Medicine, University of Lausanne, Lausanne, Switzerland. ⁹Bertarelli Platform for Gene Therapy, Ecole Polytechnique Fédérale de Lausanne, Geneva, Switzerland. ¹⁰Present address: Departamento de Fisiología de la Nutrición, Instituto Nacional de Ciencias Médicas y Nutrición Salvador Zubirán, México D.F., México. ✉e-mail: kristina.schoonjans@epfl.ch

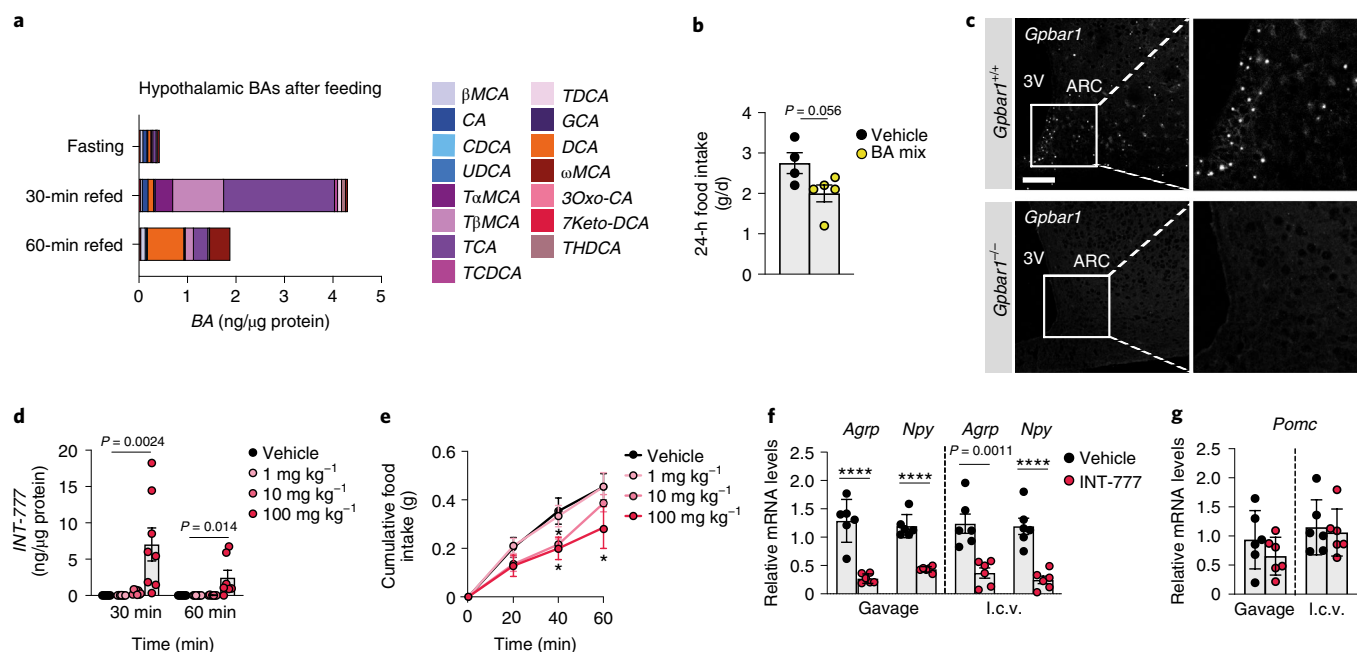


Fig. 1 | BAs reach the hypothalamus during physiological feeding and suppress food intake through TGR5. **a**, Conjugated and unconjugated BA species measured in the hypothalamus after 30 min and 60 min of refeeding in wild-type mice. Bars represent the mean from eight replicates. $n = 8$ animals. **b**, Bar graph showing the 24-h food intake after oral administration of BA mix ($n = 5$ animals) or vehicle ($n = 4$ animals). **c**, Representative images showing *Gpbar1* mRNA (white) using the RNAscope technique in the hypothalamus of TGR5 wild-type (*Gpbar1*^{+/+}) and germline TGR5 knockout (*Gpbar1*^{-/-}) mice. 3V, third ventricle. Scale bar, 50 μ m; digital zoom. $n = 4$ animals. **d**, INT-777 measurement in the hypothalamus after 30 and 60 min of oral administration of the TGR5-specific BA agonist INT-777 at three different doses or vehicle in 8-week-old wild-type mice. $n = 8$ (INT-777, 10 and 100 mg kg⁻¹ for 30 min) and $n = 7$ (all the other groups) animals. **e**, One-hour cumulative food intake of wild-type mice after oral administration of the TGR5-specific BA agonist INT-777 at three different doses or vehicle. $n = 6$ (INT-777, 100 mg kg⁻¹) and $n = 8$ (all other treatments) animals. **f**, mRNA levels of orexigenic genes *AgRP* and *Npy* 1 h after oral (gavage) and i.c.v. administration of INT-777 or vehicle in ARC-enriched hypothalamic punches of wild-type mice. $n = 6$ animals. **g**, *Pomc* mRNA levels in ARC-enriched hypothalamic punches of mice described in **f**. $n = 6$ animals. Results represent mean (**a**) or mean \pm s.e.m. (**b** and **d–g**) values. n represents biologically independent replicates. Two-tailed Student's *t*-test (**b** and **f**), one-way analysis of variance (ANOVA; **d**) or two-way ANOVA followed by Bonferroni post hoc correction (**e**) versus vehicle group were used for statistical analysis. *P* values (exact value, * $P \leq 0.05$ or **** $P \leq 0.0001$) are indicated.

Fig. 1f). These data indicate that an acute preprandial stimulation of TGR5 is sufficient to reduce food consumption during the physiological feeding state but that repetitive TGR5 activation in mice fed a chow diet only marginally affects food intake, without impacting body weight (Extended Data Fig. 1g).

Among the different neuronal populations involved in the regulation of feeding, the orexigenic AgRP/NPY neurons, promoting hunger signalling, and the anorexigenic proopiomelanocortin (POMC)/cocaine-regulated and amphetamine-regulated transcript-expressing neurons, coordinating satiety, are known to play a key role¹⁸. These neurons are located in the ARC in proximity to a fenestrated blood–brain barrier that allows a facilitated exchange with the blood. Analysis of the neuropeptide expression in the ARC showed that *AgRP* and *Npy* mRNA levels were reduced in wild-type mice after 1 h of either oral or i.c.v. administration of the TGR5 agonist (Fig. 1f), while *Pomc* levels remained unaffected (Fig. 1g).

Phenotyping of 8-week-old TGR5 wild-type (*Gpbar1*^{+/+}) and knockout (*Gpbar1*^{-/-}) mice revealed that whole-body TGR5 deletion triggered a significant increase in cumulative food intake (Fig. 2a), with an increment in food consumption starting during the night period (Fig. 2b), which coincides with the active and physiological feeding cycle. While wild-type mice showed blunted *AgRP* and *Npy* mRNA levels in response to feeding, *Gpbar1*^{-/-} mice failed to suppress the expression of these orexigenic neuropeptides (Fig. 2c). On the contrary, the expression of the anorexigenic

peptide *Pomc* was unaffected (Fig. 2d). These data suggest that TGR5 may coordinate satiety in the fed state through the inhibition of AgRP/NPY rather than stimulation of POMC neurons, without affecting the number of AgRP/NPY neurons (Extended Data Fig. 2a). Of note, the increase in food intake did not alter body weight nor fat and lean mass in *Gpbar1*^{-/-} mice compared to their controls (Extended Data Fig. 2b,c).

To analyse the distribution of TGR5 in different cell types in the brain, we used a reporter mouse model (TGR5:GFP), that co-expresses TGR5 and green fluorescent protein (GFP) under the control of the mouse *Gpbar1* regulatory gene locus (Fig. 2e and Extended Data Fig. 2d). Immunofluorescence analysis using antibodies against GFP and the neuronal marker NeuN confirmed that TGR5 is present in hypothalamic neurons (Fig. 2e), as well as in other brain cells, as previously reported¹⁶, including glia and astrocytes. To verify the importance of neuronal TGR5 in controlling food intake, we generated mice with a targeted deletion of *Gpbar1* in neurons (*Syn*^{Cre};*Gpbar1*^{fl/fl}). In line with the expression of *Gpbar1* in multiple cell types of the ARC, a substantial, but not complete, reduction in *Gpbar1* mRNA levels was observed in the ARC of *Syn*^{Cre};*Gpbar1*^{fl/fl} mice (Extended Data Fig. 2e). Consistently with the findings observed in the whole-body *Gpbar1*^{-/-} mice, *Syn*^{Cre};*Gpbar1*^{fl/fl} mice displayed no apparent changes in body weight and composition (Extended Data Fig. 2f,g); however, a marked increase in cumulative food intake (Fig. 2f and Extended Data Fig. 2h) and in the expression of orexigenic (Fig. 2g) but not

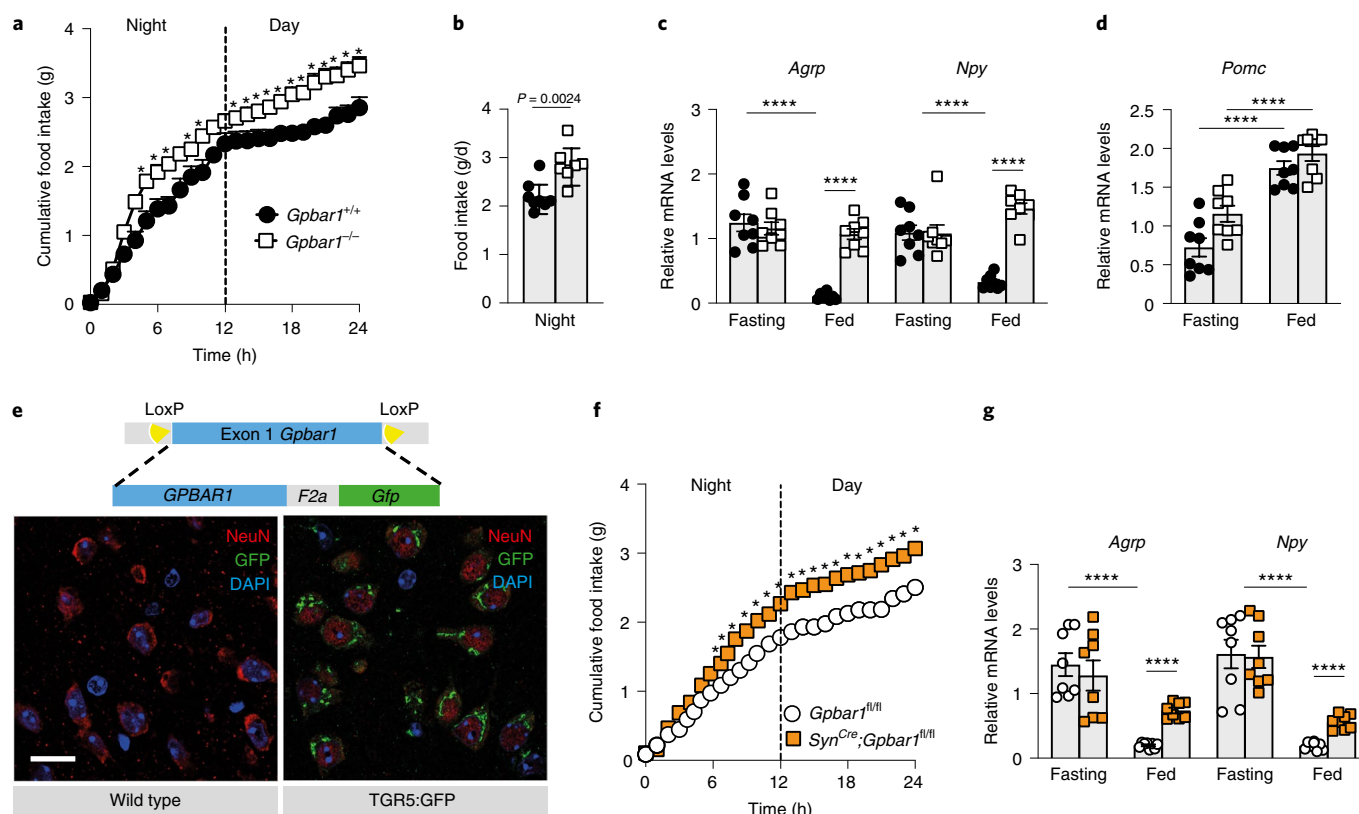


Fig. 2 | TGR5 is expressed in neurons and its deletion increases food intake. **a**, Cumulative food intake (24 h) of 8-week-old TGR5 wild-type ($Gpbar1^{+/+}$; $n = 6$) and germline TGR5 knockout ($Gpbar1^{-/-}$; $n = 7$) mice. **b**, Twelve-hour food intake of $Gpbar1^{+/+}$ ($n = 8$) and $Gpbar1^{-/-}$ ($n = 7$) mice. **c**, mRNA levels of orexigenic genes *AgRP* and *Npy* after overnight fasting and fed conditions in ARC-enriched hypothalamic punches of $Gpbar1^{+/+}$ and $Gpbar1^{-/-}$ mice. $n = 8$ animals. **d**, *Pomc* mRNA levels in ARC-enriched hypothalamic punches of mice described in **c**. $n = 8$ animals. **e**, Generation of transgenic mice expressing TGR5 and GFP under the control of the mouse *Gpbar1* promoter (TGR5:GFP) and hypothalamic immunodetection of the neuronal marker NeuN (red), TGR5 (GFP; green) and nuclei staining (DAPI; blue) in TGR5 wild-type and TGR5:GFP mice. Scale bar, 20 μ m. $n = 4$ animals. **f**, Cumulative food intake (24 h) of $Gpbar1^{fl/fl}$ and *Syn*^{Cre};*Gpbar1*^{fl/fl} mice. $n = 8$ animals. **g**, mRNA levels of orexigenic genes *AgRP* and *Npy* after overnight fasting and normal fed conditions in ARC-enriched hypothalamic punches of $Gpbar1^{fl/fl}$ and *Syn*^{Cre};*Gpbar1*^{fl/fl} mice. $n = 8$ animals. Results represent the mean \pm s.e.m. n represents biologically independent replicates. Two-tailed Student's *t*-test (**b–d** and **g**) or two-way ANOVA followed by Bonferroni post hoc correction (**a** and **f**) versus $Gpbar1^{+/+}$ (**a–c**), fasting (**d**) or $Gpbar1^{fl/fl}$ (**f** and **g**) groups was used for statistical analysis. *P* values (exact value, * $P \leq 0.05$ or **** $P \leq 0.0001$) are indicated.

anorexigenic (Extended Data Fig. 2i) genes was observed. Moreover, preprandial oral administration of INT-777 decreased cumulative food intake in $Gpbar1^{fl/fl}$ and $Gpbar1^{+/+}$ mice (Extended Data Fig. 2j–m), but not in whole-body $Gpbar1^{-/-}$ (Extended Data Fig. 2l,m) and neuron-restricted *Syn*^{Cre};*Gpbar1*^{fl/fl} mice (Extended Data Fig. 2j,k), confirming that the modulation of AgRP/NPY expression involved in controlling eating behaviour is driven by neuron-specific TGR5.

To determine which neuronal population in the ARC is responsible for conferring the food intake phenotype, we generated AgRP (*AgRP*^{Cre};*Gpbar1*^{fl/fl}) and POMC (*Pomc*^{Cre};*Gpbar1*^{fl/fl}) neuron-specific *Gpbar1* mutant mouse models and confirmed that *Gpbar1* expression was reduced by half in the ARC of both strains (Fig. 3a and Extended Data Fig. 3a). *AgRP*^{Cre};*Gpbar1*^{fl/fl} but not *Pomc*^{Cre};*Gpbar1*^{fl/fl} mice displayed a significant increase in food intake during the night phase compared to their controls ($Gpbar1^{fl/fl}$ mice; Fig. 3b and Extended Data Fig. 3b). Moreover, oral administration of INT-777 exerted an anorexigenic action in the *Pomc*^{Cre};*Gpbar1*^{fl/fl} mice (Fig. 3c), as well as in $Gpbar1^{fl/fl}$ controls (Fig. 3c,d), while this effect was significantly blunted in *AgRP*^{Cre};*Gpbar1*^{fl/fl} mice (Fig. 3d), indicating that TGR5 signalling in AgRP/NPY neurons, but not in POMC neurons, is important for the control of food intake. Similarly to our previous findings, deletion of TGR5 in both AgRP/NPY and POMC neurons did not affect body weight and composition (Extended Data Fig. 3c–f). Co-staining experiments using *AgRP* RNAscope

probes and GFP immunofluorescence in TGR5:GFP mice confirmed that *Gpbar1* is expressed in AgRP/NPY neurons (Fig. 3e). Immunofluorescence experiments showed that INT-777-mediated TGR5 activation in fasted animals significantly decreased the percentage of Fos-positive AgRP/NPY neurons (Fig. 3f,g), mimicking the fed state (Extended Data Fig. 3g,h). Altogether, these data suggest that TGR5 suppresses food intake through inhibition of hypothalamic AgRP/NPY neurons.

Because TGR5 mediates acute signalling responses, we reasoned that, in addition to its effect on orexigenic gene expression, this receptor could also be involved in blocking neuropeptide secretion. To test this hypothesis, we conducted ex vivo experiments on hypothalamic explants. After fasting, TGR5 activation with INT-777 acutely blunted the release of the orexigenic neuropeptides AgRP and NPY in $Gpbar1^{+/+}$, but not in $Gpbar1^{-/-}$, explants (Fig. 4a,b). Importantly, TGR5 stimulation did not affect the secretion of gamma-aminobutyric acid (GABA), a fast-acting small-molecule transmitter that is also released from AgRP/NPY neurons¹⁸ (Extended Data Fig. 4a,b). In contrast to AgRP and NPY neuropeptides, which are stored in large dense-core vesicles (DCVs), GABA is quickly released from small clear synaptic vesicles, which are docked closely to the plasma membrane in axon terminals¹⁹. The distinct processing and secretion mode could account for the observed difference in neuropeptide release. In addition, TGR5 stimulation did

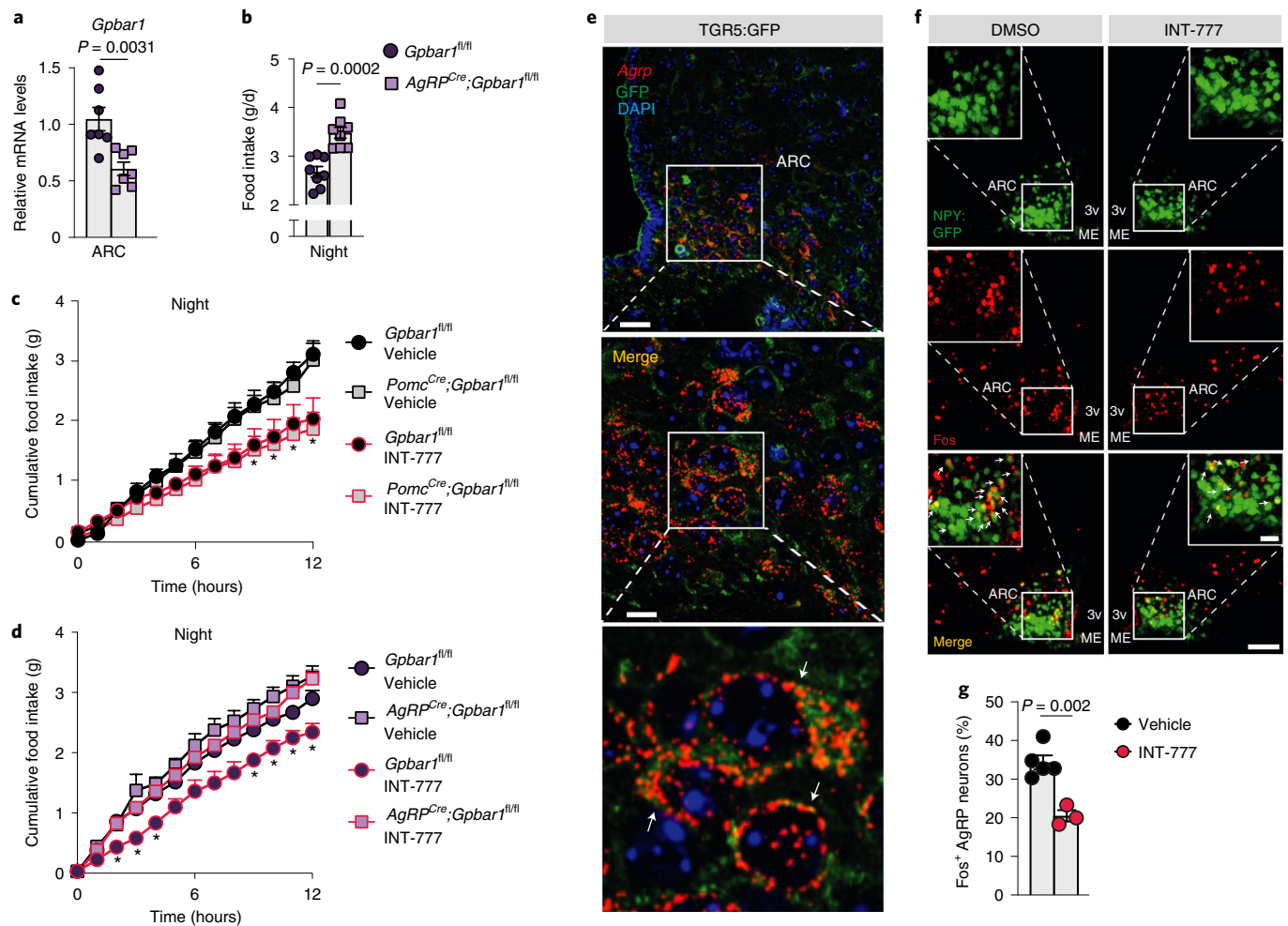


Fig. 3 | Selective deletion of TGR5 in AgRP/NPY but not in POMC neurons abrogates satiety induced by BA derivatives. **a**, *Gpbar1* mRNA levels in ARC-enriched hypothalamic punches of control mice (*Gpbar1^{fl/fl}*) and AgRP neuron-specific TGR5 knockout (*AgRP^{Cre};Gpbar1^{fl/fl}*) mice. $n = 7$ animals. **b**, Twelve-hour food intake of *Gpbar1^{fl/fl}* and *AgRP^{Cre};Gpbar1^{fl/fl}* mice. $n = 8$ animals. **c**, Twelve-hour cumulative food intake of control (*Gpbar1^{fl/fl}*) and POMC neuron-specific TGR5 knockout (*Pomc^{Cre};Gpbar1^{fl/fl}*) mice after oral administration of TGR5 agonist INT-777 or vehicle. $n = 6$ (*Gpbar1^{fl/fl}* INT-777), $n = 7$ (vehicle groups) and $n = 8$ (*Pomc^{Cre};Gpbar1^{fl/fl}* INT-777) animals. **d**, Twelve-hour cumulative food intake of control (*Gpbar1^{fl/fl}*) and AgRP neuron-specific TGR5 knockout (*AgRP^{Cre};Gpbar1^{fl/fl}*) mice after oral administration of TGR5 agonist INT-777 or vehicle. $n = 7$ (*Gpbar1^{fl/fl}* INT-777) and $n = 8$ (all other groups) animals. **e**, Representative images showing *AgRP* mRNA (red) using the RNAscope technique together with TGR5 immunodetection (GFP; green) and nuclei staining (DAPI; blue) in the ARC of TGR5:GFP mice ($n = 4$ animals). Arrows in the digital zoom image (lower) indicate cells that co-express *AgRP* mRNA (red) and GFP (green). Colocalization between *AgRP* and GFP is shown in orange (merge). Scale bars, 50 μ m and 10 μ m; digital zoom in the image below. **f**, Representative images (f) and quantification (g) of Fos immunoreactivity (red) in AgRP/NPY neurons (green) and merge (orange) in the hypothalamus of AgRP/NPY:GFP-expressing mice after oral administration of INT-777 ($n = 3$ animals) or vehicle ($n = 5$ animals). Arrows in images indicate colocalization of Fos and GFP. Scale bar, 100 μ m. Results represent the mean \pm s.e.m. n represents biologically independent replicates. Two-tailed Student's *t*-test (**a**, **b** and **g**) or two-way ANOVA followed by Bonferroni post hoc correction (**c** and **d**) versus *Gpbar1^{fl/fl}* (**a** and **b**), *Gpbar1^{fl/fl}* vehicle for *Pomc^{Cre};Gpbar1^{fl/fl}* (**c**), *Gpbar1^{fl/fl}* vehicle for *AgRP^{Cre};Gpbar1^{fl/fl}* (**d**) or vehicle (**g**) groups was used for statistical analysis. P values (exact value or $*P \leq 0.05$) are indicated.

not affect POMC-derived alpha-melanocyte-stimulating hormone (α MSH) secretion (Extended Data Fig. 4c). These results confirm that the physiological anorexigenic effect of BA–TGR5 signalling during the postprandial state is achieved through the selective reduction of AgRP/NPY secretion.

To further explore the molecular mechanism of the observed phenotype, we conducted a series of experiments in the mouse embryonic hypothalamic cell line N41 (mHypoE-N41), an AgRP/NPY-positive cell line that also expresses *Gpbar1* (Extended Data Fig. 4d). In line with the results obtained in vivo and ex vivo, INT-777 treatment rapidly decreased *AgRP* and *Npy* expression in mHypoE-N41 cells (Extended Data Fig. 4e) and transiently blocked AgRP release (Extended Data Fig. 4f). This effect was TGR5-dependent because it was lost after silencing of the receptor

(Extended Data Fig. 4g). Previous evidence has shown that, in the early stages of DCV mobilization, the cortical actin filaments represent a primary physical barrier between the secretory vesicles and the plasma membrane and that rearrangements of the actin network are established mechanisms to restrict peptide secretion in different cell types, including neurons²⁰. Actin depolymerization and stabilization can be modulated by the Rho–ROCK signalling pathway^{21,22}. Specifically, activation of ROCK promotes actin fibre stabilization and thus blocks DCV exocytosis^{23,24}. To test the hypothesis that TGR5 could transiently modulate neuropeptide secretion through the Rho–ROCK–actin axis, we evaluated AgRP and NPY secretion after INT-777 treatment and concomitant ROCK inhibition with thiazovivin. Inhibition of ROCK abrogated the TGR5-dependent block of AgRP and NPY secretion (Fig. 4c,d). Moreover, short-term

TGR5 stimulation with INT-777 or BA mix, modulated the cell cytoskeleton, favouring the stabilization and polymerization of cortical actin fibres (Fig. 4e). In line with these findings, TGR5 activation triggered transient phosphorylation of the two canonical ROCK targets, myosin light chain (MLC) and COFILIN, while concomitant thiazovivin treatment counteracted this process (Fig. 4f and Extended Data Fig. 4h,i). In addition to INT-777, short stimulation with BA mix induced COFILIN phosphorylation in vitro (Extended Data Fig. 4j), indicating that BAs can also induce ROCK signalling. In line with our previous observations, the release of NPY-containing granules in mHypoE-N41 cells was markedly reduced after acute TGR5 activation with INT-777 or BA mix (Fig. 4g), as reflected by the increase in intracellular accumulation of fluorescent NPY-mCherry vesicles (Fig. 4h). Altogether, these results show that TGR5 activation decreases the mRNA abundance and transiently blocks the release of orexigenic neuropeptides in AgRP/NPY-expressing neurons, contributing to the inhibition of food intake after physiological feeding.

BAs have been established as versatile signalling molecules mediating the communication between the enterohepatic and peripheral metabolic organs, wherein circulating BAs coordinate adaptation to nutritional and physiological cues⁸. While growing evidence supports the presence of BAs and their transporters in the brain, little is known about their central actions. Our current studies reveal that a multitude of BA species can reach the hypothalamus shortly after feeding and trigger a molecular response in the hypothalamic AgRP/NPY neurons, leading to a TGR5-mediated repression of food intake during the physiological fasting–feeding transition. The anorexigenic action of BAs is furthermore supported by oral or i.c.v. administration of INT-777, a BA derivative with selective TGR5 agonistic properties, indicating that neuronal TGR5 activation is essential in this process. In line with the rapid non-genomic actions of G-protein-coupled-receptor signalling, our findings support a model in which TGR5 activation by BAs represses appetite via a dual mechanism, involving an acute inhibition of AgRP/NPY vesicle release, followed by a repression of *Agrp/Npy* transcript levels within the first hour after BA exposure. While the latter mechanism likely engages similar signalling transduction pathways as those by which leptin and insulin inhibit the expression of these neuropeptides²⁵, the early repressive actions of BAs on Rho–ROCK–actin-dependent AgRP/NPY exocytosis represent an unanticipated pathway by which BAs initiate repression of appetite.

While our findings demonstrate that BAs transiently accumulate in the hypothalamus to coordinate satiety during the homeostatic fasting–feeding transition, they also consolidate that the BA–TGR5 pathway is not essentially required to maintain energy balance during normal chow feeding, as reported earlier⁴. This is not surprising, as homeostasis pertains to a self-regulating process in which systems tend to maintain stability. Homeostatic circuits, however, can be compromised or damaged by disease or chronic high-fat-diet

feeding, and it is possible that distinct TGR5-triggered circuits may prevail in these pathophysiological settings. Further studies are needed to explore this possibility.

Unlike its function in the CNS, the role of TGR5 in peripheral metabolism has been widely studied. Activation of this receptor exerts beneficial metabolic effects such as the induction of the thermogenic programme in brown³ and white⁷ adipose tissue to confer protection against diet-induced obesity^{3,4,7} and drives anti-inflammatory processes preventing the development of atherosclerosis⁵ and insulin resistance⁶. In addition, TGR5 signalling regulates glucose homeostasis^{4,26} by controlling the secretion of gut hormones, including glucagon-like peptide-1. Besides its incretin effect, glucagon-like peptide-1 also signals to neurons via the systemic circulation^{27,28} or through activation of vagal nerve afferents to the intestine and reduces food intake²⁹. While our findings support a role for the CNS in mediating BA-induced satiety, we cannot exclude the possibility that TGR5 expressed in peripheral neurons could also contribute to the anorexigenic actions of BAs. Indeed, we observed that synapsin-directed recombination of the *Gpbar1* locus in both peripheral and central neurons leads to a significant rise in spontaneous feeding. Consistently, a recent study showed that BAs synergistically act with the gut peptide cholecystokinin to reduce appetite through activation of TGR5 and cholecystokinin-A receptors in the nodose ganglia neurons, an effect abolished by vagotomy³⁰. These data, together with ours, indicate that TGR5 signalling primes the satiety signal after feeding via both direct and indirect actions in the gut–brain axis of mice. Whether these findings will translate to humans remains to be investigated.

Methods

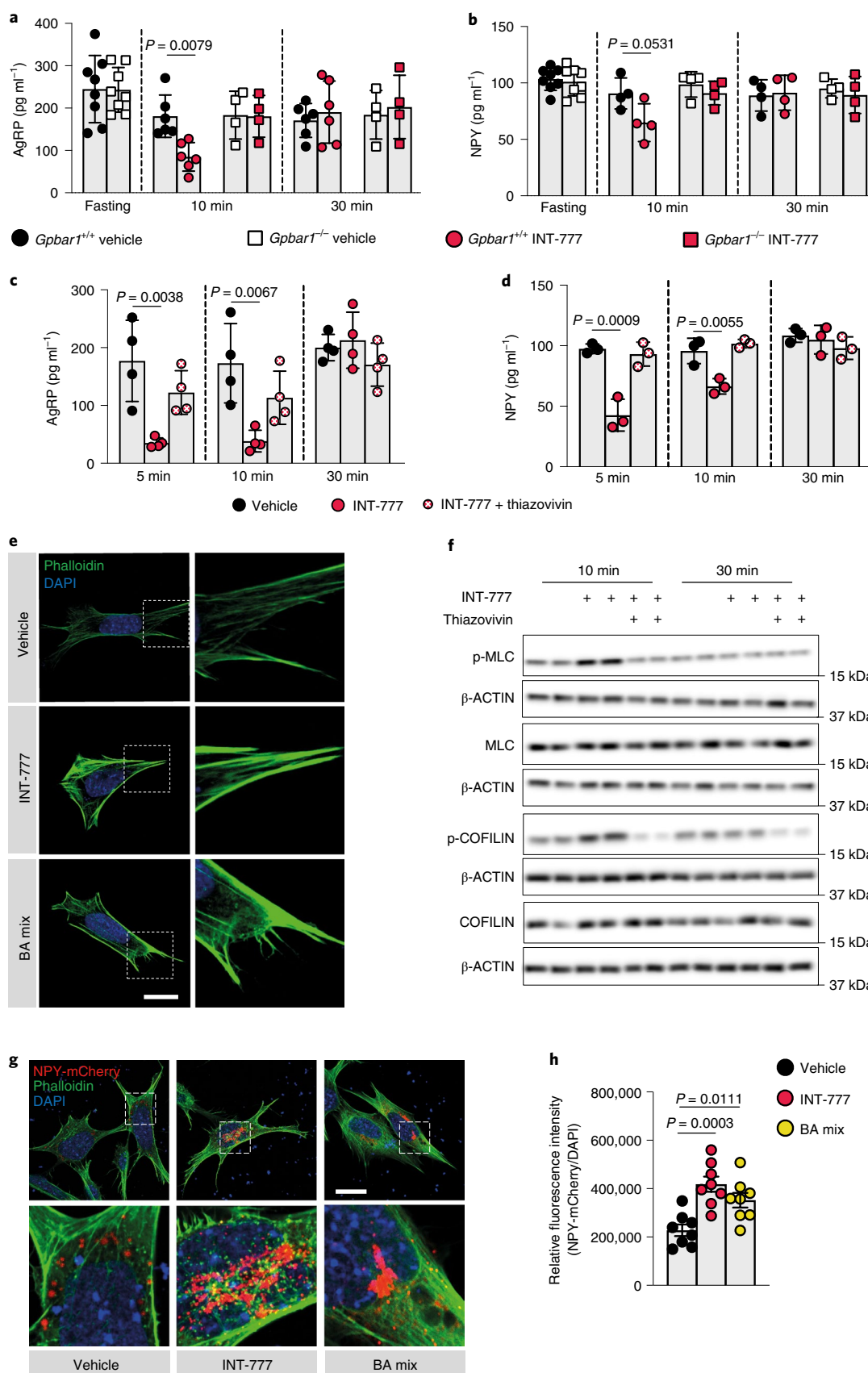
Animal studies. Generation of mouse models and tissue collection. The whole-body *Gpbar1*^{−/−} and the NPY:GFP mouse models have been described previously^{4,31}. Mice carrying floxed alleles for the *Gpbar1* gene were crossed with different Cre lines (purchased from Jackson Laboratory) to achieve selective deletion of *Gpbar1* in all neurons (Synapsin1-Cre, Tg(Syn1-cre)671Jxm; JAX stock no. 003966)³², in AgRP neurons (*Agrp*-IRES-Cre (*Agrp*^{tm1(cre)Lowl/J}); JAX stock no. 012899)³³ or in POMC neurons (*Pomc1*-Cre (*Tg(Pomc1-cre)16Lowl/J; JAX stock no. 005965)³⁴. Male mice 8- to 15-weeks old were used in the study, and the different lines were validated by analysis of *Gpbar1* mRNA expression in the brain regions of interest. Mice were housed with ad libitum access to water and food (chow diet DS-SAFE150) and kept under a 12-h dark/12-h light cycle with a temperature of 22 °C ± 1 °C and a humidity of 60% ± 20%. Body weight was monitored weekly over an 8-week period. Body composition was analysed by non-invasive monitoring of fat and lean mass using EchoMRI (Echo Medical Systems), as previously described³⁵. Mice were euthanized in the morning after an overnight fast (12–16 h), in the fed state (09:00–10:00) or after physiological feeding at the onset of the dark phase for the indicated time points after a 12-h light-phase fasting. For biochemical analysis, tissues were collected and flash frozen in isopentane and dry ice and stored at −80 °C. For histological analysis, mice were anaesthetized and transcardially perfused with 0.9% saline with heparin (10 mg l^{−1}; Sigma-Aldrich, H3393), followed by fixative solution (4% paraformaldehyde in 0.1 M phosphate buffer). Brains were collected, post-fixed overnight, then cryo-protected with a 30% sucrose solution in PBS at 4 °C and frozen.*

To evaluate the expression and localization of *Gpbar1* in the brain, we used a transgenic mouse reporter model (TGR5:GFP), that co-expresses human *GPBAR1*

Fig. 4 | TGR5 regulates orexigenic neuropeptide secretion through transient activation of the Rho–ROCK signalling pathway. a,b, AgRP (**a**) or NPY (**b**) release in hypothalamic explants from TGR5 wild-type (*Gpbar1*^{+/+}) and germline TGR5 knockout (*Gpbar1*^{−/−}) mice after starvation or 10- and 30-min stimulation with TGR5 agonist INT-777 or vehicle. *n* = 4 (*Gpbar1*^{−/−}, 10 and 30 min), *n* = 6 (*Gpbar1*^{+/+}, 10 and 30 min) and *n* = 8 (fasting; **a**) animals; *n* = 4 (*Gpbar1*^{+/+} and *Gpbar1*^{−/−}, 10 and 30 min) and *n* = 8 (fasting; **b**) animals. **c,d**, AgRP (**c**) or NPY (**d**) release after starvation followed by short-term (5, 10 and 30 min) stimulation with TGR5 agonist INT-777, vehicle or preincubation (30 min) with specific ROCK inhibitor (10 μM thiazovivin) followed by INT-777 stimulation in mouse embryonic hypothalamic N41 cell line (mHypoE-N41). *n* = 4 (**c**) and *n* = 3 (**d**) samples. **e**, Representative images of phalloidin staining to detect actin fibres (green) and DAPI staining to detect nuclei (blue) after 10 min of stimulation with INT-777, BA mix or vehicle in mHypoE-N41 cells. Scale bar, 10 μm; digital zoom. *n* = 4 samples. **f**, Representative western blot of phosphorylated or total ROCK signalling targets (MLC and COFILIN) from the cells described in **c**, β-ACTIN was used as loading control. *n* = 4 samples. **g,h**, Representative images (**g**) or quantification of fluorescence intensity (**h**) of NPY vesicles (red), phalloidin staining to detect actin fibres (green) and DAPI staining to detect nuclei (blue) after 10 min of stimulation with INT-777, BA mix or vehicle in mHypoE-N41-transfected cells. Scale bars, 10 μm; digital zoom. *n* = 8 samples. Results represent the mean ± s.e.m. *n* represents biologically independent replicates. One-way ANOVA followed by Bonferroni post hoc correction versus *Gpbar1*^{+/+} vehicle (**a** and **b**) or vehicle (**c**, **d** and **h**) groups was used for statistical analysis. Exact *P* values are indicated.

and the enhanced green fluorescent protein (*Gfp*) linked by the foot-and-mouth disease virus (*F2a*) cleaving peptide sequence under the control of the endogenous *Gpbar1* mouse promoter.

Food intake recording and oral administration of *TGR5* agonist. Food intake was recorded at regular intervals by means of a TSE PhenoMaster system (TSE Systems). Each mouse was placed individually in a cage with normal bedding and



free access to food and water during the acclimatization (48 h) and the test (30 min, 1 h or 24 h) periods. The system was set to have a 12-h/12-h light–dark cycle. The oral administration of INT-777 (TES Pharma; 1 mg kg⁻¹, 10 mg kg⁻¹ or 100 mg kg⁻¹ in 2% CMC solution), BA mix (a crude bile extract containing the sodium salt of taurocholic, glycocholic, deoxycholic and cholic acids; Sigma, S9875; 1 mg kg⁻¹, 10 mg kg⁻¹ or 100 mg kg⁻¹ in 2% CMC) or vehicle (CMC 2% final solution) was performed through gavage 30 min before the start of the dark phase.

Oral administration of TGR5 agonists. Mice of the indicated genotypes were fasted overnight (12–15 h) and gavaged with vehicle, the selective TGR5 agonist INT-777 (TES Pharma; 100 mg kg⁻¹ in 2% CMC) or BA mix (Sigma, S9875, 10 µg ml⁻¹ in DMSO).

Stereotaxic administration. TGR5 agonist INT-777 (30 µM) or vehicle (DMSO) was administered by i.c.v. injection in the third ventricle. For the stereotaxic injections, mice were anaesthetized by intraperitoneal injection of xylazine (5–10 mg kg⁻¹) plus ketamine (80–100 mg kg⁻¹) followed by the placement on stereotaxic frame on a heating pad and with eye gel cover (Viscotears). Before intracerebral injection, the region was disinfected with Betadine. After scalp shaving, a local anaesthesia was performed with 20 µl of a lidocaine (6 mg kg⁻¹) and bupivacaine (2.5 mg kg⁻¹) mixture. A 1-cm skin incision was performed, by piercing the skull with a suitable drilling machine (Dremel), mounted on the arm of the stereotaxic frame. Stereotaxic coordinates were determined using Paxinos and Franklin's mouse brain atlas³⁶, according to bregma: anteroposterior (AP) –1.46 mm; dorsoventral (DV) –5.6 mm; lateral (ML) 0 mm. The speed of injection was 0.2 µl min⁻¹ via an automatic injector and the injected volume was 2 µl. After injection, a suture of the skin was performed with 6–0 bioresorbable thread, and the skin was disinfected. The mice were euthanized 1 h after i.c.v. injection and the brains were collected and flash frozen in isopentane and dry ice for further analysis.

Chronic intracerebroventricular administration of TGR5 agonists. Male C57BL/6J mice (Janvier, France) were anaesthetized using isoflurane. Subcutaneous buprenorphine (0.1 mg kg⁻¹) and lidocaine at the level of the skull (0.1 ml at 0.5%) were injected before surgery to reduce discomfort. Unconscious mice were placed on a stereotaxic frame (David Kopf Instruments), and an incision was made in the skin to expose the skull after fur removal and asepsis with an iodine solution (Betadine). A burr hole for the stainless-steel guide cannula (C313GS-5/SPC, G22; Plastics One) was drilled on the skull (AP: –0.5; ML: –1.2; DV: –2.1). Following surgery, all mice received saline solution subcutaneously and meloxicam (5 mg kg⁻¹) for 2 d. Animals were housed individually, and body weight was monitored daily for 1 week to assess recovery. All i.c.v. treatments were performed with a 28-gauge cannula, which was fitted into the guide cannula and connected by a polyethylene tube to a micro syringe. Correct cannula placement was assessed in vivo by i.c.v. infusion of NPY (Phoenix Pharmaceuticals) in free-fed mice, as described previously³⁷. Mice that consumed >0.5 g of food after 2 h of injection were included in the study. All infusions were carried out in free-fed mice, and compounds were administered just before the dark phase. INT-777 (5 µg in 1 µl 60% DMSO–40% aCSF) injections were performed daily for 1 week. Body weight was measured before and 24 h after the i.c.v. administrations; food intake was measured daily after 1, 2, 4 and 24 h from the i.c.v. administrations.

Ethical approval. These experiments were authorized by the Veterinary Office of the Canton of Vaud, Switzerland (authorization nos. 3143 and 3143.1), the French Ministry of Agriculture and Fisheries and the Ethical Committee of the University of Bordeaux for Animal Experimentation (authorization no. 13394) and by the Yale University Institutional Animal Care and Use Committee (authorization no. 10670).

RNAscope. RNAscope Multiplex Fluorescent V2 assay (Bio-Techne, 323110) was performed according to manufacturer's instruction on 4-µm paraffin sections, hybridized with the probes Mm-*Gpbar1*-C1 (Bio-Techne, 318451), Mm-*Agrp*-C2 (Bio-Techne, 400711-C2) and Mm-*Ppib*-C1 (Bio-Techne, 313911) as positive control and DapB-C1 (Bio-Techne, 310043) as negative control at 40°C for 2 h and revealed with TSA Plus Cy3 (Perkin Elmer, NEL744E001KT). Tissues were counterstained with DAPI and mounted with Fluoromount-G (Bioconcept, 100.01). When indicated, sections were incubated overnight at 4°C with a goat anti-GFP primary antibody (Abcam, ab6673; 1:200 dilution). After incubation with a donkey anti-goat Alexa Fluor 488 secondary antibody (Thermo Fisher, A11055; 1:1,000 dilution), tissues were counterstained with DAPI and mounted with Fluoromount-G (BioConcept, 100.01). The imaging was performed with an LSM 700 confocal microscope (Carl Zeiss).

Fluorescence in situ hybridization. Brain coronal sections (30 µm) were cut with a CM1950 cryostat (Leica), collected, and stored in an antifreeze solution (30% ethylene glycol and 30% glycerol in KPBS) at –20°C until analysis. Fluorescence in situ hybridization with digoxigenin-labelled riboprobe against mouse *AgRP* (AgRP-DIG; Allen Brain Atlas, RP_051027_01_B05) was performed as previously described³⁸. Briefly, free-floating sections were treated with 0.2 M HCl and then acetylated with 0.25% acetic anhydride in 0.1 M triethanolamine

at pH 8.0 for 10 min. Between all steps, sections were rinsed in PBS with 0.01% diethylpyrocarbonate. After hybridization with AgRP-DIG (1:1,000 dilution) overnight at 70°C, sections were washed at 65°C with increased stringency buffers and incubated for 30 min in 3% H₂O₂ PBS, for 1 h in blocking buffer (Akoya Biosciences, FP1012), for 2 h in anti-digoxigenin-POD (Sigma, 11207733910; 1:1,000 dilution) and for 30 min in TSA plus Cy3 system (Akoya Biosciences, TS-000202; 1:100 dilution). Between all steps, sections were rinsed in TNT (100 mM Tris-HCl, 150 mM NaCl and 0.05% Tween20). Slices were counterstained with DAPI and mounted on gelatinized slides and cover-slipped with Prolong. Images were acquired on a Leica DM6000 CFS TCS SP8 confocal microscope using a ×20/0.75 objective (Leica HC HPL Apo CS2). An engineer of the Bordeaux Imaging Center designed a toolset within ImageJ to automatize the quantification of AgRP-positive cells within the volume of the ARC. Analyses were performed by an experimenter who was blinded to the experimental group on 3–4 ARC (*Gpbar1*^{+/+} *n* = 4 and *Gpbar1*^{–/–} *n* = 3) from 2–4 sections per animal. The number of AgRP-positive cells per mm³ of ARC tissue was then calculated.

Immunofluorescence. Brains from NPY:GFP mice³¹ were collected, post-fixed overnight and sectioned (50 µm) using a vibratome. Brain sections were processed for immunofluorescence staining using anti-GFP antibody (Abcam, ab13970; 1:5,000 dilution) and/or anti-Fos antibody (Santa Cruz, sc-52; 1:2,000 dilution). After overnight incubation and washes, sections were incubated with a secondary antibody (Alexa Fluor 488-coupled goat anti-chicken, 1:500 dilution; Life Technologies; A11039) or with biotinylated goat anti-rabbit immunoglobulin G (Vector Laboratories, BA-1000; 1:200 dilution) and then further incubated with streptavidin-conjugated Alexa Fluor 594 (Life technologies, S32356; 1:2,000 dilution) for 2 h at room temperature (RT). Sections were then cover-slipped with VectaShield antifade mounting medium (Vector Laboratories, H-1000), and fluorescence images were captured with a fluorescence microscope (KEYENCE, BZ-X710).

Hypothalamic explants. Whole brain from overnight fasted (fasting condition) or fed (fed condition) mice was dissected in the morning and placed into a cutting solution (2.5 mM KCl, 6 mM MgCl₂, 1 mM CaCl₂, 1.25 mM NaH₂PO₄, 26 mM NaHCO₃, 10 mM glucose and 250 mM sucrose). A 2-mm thick slice (at bregma levels from approximately –0.4 mm to –2.65 mm) of mediobasal forebrain including the paraventricular nucleus and ARC was prepared using a vibratome (Leica Microsystems, VT100S), and the hypothalamus was cut from the rest of the brain in the cooled cutting solution and immediately transferred to RT in a 96-well plate. For fed conditions, hypothalami were incubated for 1 h at 37°C with 95% O₂ and 5% CO₂ in aCSF (124 mM NaCl, 3 mM KCl, 2 mM CaCl₂, 2 mM MgCl₂, 1.23 mM NaH₂PO₄, 26 mM NaHCO₃ and 10 mM glucose). After equilibration, hypothalami were incubated for 45 min in aCSF (15 mM glucose, basal) and then for 10 and 30 min in a high-glucose (15 mM glucose) aCSF with either INT-777 (30 µM) or vehicle (DMSO). For the fasting conditions, hypothalami were incubated at 37°C with low-glucose (6 mM glucose) aCSF. After 1 h of equilibration with 95% O₂ and 5% CO₂, hypothalami were incubated for 45 min in low-glucose aCSF (basal) and then for 10 and 30 min in low-glucose aCSF with either INT-777 (30 µM) or vehicle. Tissue viability was verified by exposure to 56 mM KCl for 45 min. At the end of each stimulation, supernatants were collected and frozen immediately in liquid nitrogen.

Cell culture, transfection and stimulation. The mouse embryonic hypothalamic mHypoE-N41 (Tebu-bio, CLU121-A) cells were cultured in complete medium (DMEM containing glucose (4.5 g l⁻¹), 10% FBS and penicillin–streptomycin (10 mg ml⁻¹). Cells were tested for mycoplasma using MycoProbe (R&D Systems, CUL001B), following the manufacturer's instructions.

Transfection of the cells was performed with the jetPEI reagent (Polyplus transfection, 101-10N), according to the manufacturer's instructions. For the silencing of TGR5, cells were transfected with 2.5 µg of DNA (sh-*Gpbar1* or control (sh-*Ctr1*)) plasmids. For the vesicle tracking experiment, cells were transfected with 2.5 µg DNA of a NPY-mCherry plasmid (Addgene, 67156).

For acute stimulation of the TGR5 signalling pathway, mHypoE-N41 cells were starved for 4 h with low-glucose DMEM (1 g l⁻¹) FBS-free medium with 0.1% free fatty acid-free BSA, followed by treatment with INT-777 (30 µM), BA mix (10 µg ml⁻¹) or vehicle (DMSO or ethanol) for 5, 10, 15, 30 or 60 min.

Neuropeptide release measurements. Detection of AgRP, NPY and GABA neuropeptides from mHypoE-N41 cell or hypothalamic explant supernatants was performed using ready-to-use ELISA kits (LSBio; LS-F32623-1, LS-F5409 and LS-F4121-1, respectively), according to the manufacturer's instructions. Alpha-melanocyte-stimulating hormone detection was performed by radioimmunoassay (Phoenix Pharmaceuticals, RK-043-01), according to the manufacturer's instructions.

Immunocytochemistry. mHypoE-N41 cells were rinsed with 1× ice-cold PBS and fixed with 4% paraformaldehyde for 15 min at RT. After three washes, the cells were permeabilized with 0.1% Triton X-100 for 15 min at RT. Blocking and antibody incubation were performed in 3% BSA. Blocking was performed for 1 h

at RT, and phospho-Cofilin Ser3 (Cell Signaling, 3311; 1:200 dilution) primary antibody was incubated overnight at 4 °C. Three washes were performed before incubation with secondary anti-rabbit Alexa Fluor 647 (Jackson ImmunoResearch, 711-605-152; 1:1,000 dilution) antibody and phalloidin-conjugated Alexa Fluor 488 Phalloidin (Thermo Fisher Scientific, A12379; 1:200 dilution) for 1 h at RT. Cells were washed, incubated with DAPI for 10 min and mounted. The imaging was performed with an LSM 700 confocal microscope (Carl Zeiss).

Quantitative real-time PCR. RNA was extracted from ARC brain punches, tissues or mHypoE-N41 cells using the RNAqueous Kit (Thermo Fisher Scientific, AM1912) and was transcribed to complementary DNA using QuantiTect Reverse Transcription Kit (Qiagen, 205311), following manufacturers' instructions. Expression of selected genes was analysed using the LightCycler 480 System (Roche) and SYBR Green chemistry. The oligonucleotide sequences used are listed in the Supplementary Table 2. All qPCR results were presented relative to the mean of *36b4* and *B2m* housekeeping genes (DDCt method). The average of at least three technical repeats was used for each biological data point.

Western blotting. Samples were lysed in RIPA buffer (50 mM Tris-HCl (pH 7.4), 150 mM KCl, 1 mM EDTA, 1% Triton X-100, 0.5% sodium deoxycholate, protease and phosphatase inhibitors). Proteins were separated by SDS-PAGE and transferred onto nitrocellulose membranes. Blocking and antibody incubations were performed in 5% BSA. Myosin light chain 2 (MLC2; 3672; 1:1,000 dilution), phospho-MLC2 (Ser19; 3671; 1:1,000 dilution), COFILIN (5175; 1:1,000 dilution) and phospho-Cofilin (3311; 1:1,000 dilution) antibodies were purchased from Cell Signaling; beta-ACTIN (Sigma-Aldrich, A5441; 1:1,000 dilution) antibody detection was used as the loading control. Antibody detection reactions were developed by enhanced chemiluminescence (Advansta) and imaged using the c300 imaging system (Azure Biosystems). Quantification was performed using ImageJ software.

BA quantification. BAs and INT-777 were profiled by stable isotope dilution mass spectrometry assay at the Metabolomics Platform of University of Lausanne. Standard solutions for calibration and samples were prepared as described previously³⁹. Briefly, calibrators were prepared by serial dilutions with stripped serum (C0–C7). The internal standard mixture contained 13 deuterium-labelled BAs. For sample preparation, the frozen hypothalamus was homogenized in tissue homogenizer (Precellys) by the addition of MeOH:H₂O (2:1 ratio) with 0.1% formic acid (300 µl) and ceramic beads (for 2 × 20 s at 10,000 r.p.m.). Homogenized extracts were centrifuged for 15 min at 14,000g at 4 °C, and the supernatants were further processed using solid-phase extraction, as described previously³⁹. For analyses with liquid chromatography–high-resolution mass spectrometry, BA quantification was performed on a Vanquish Horizon (Thermo Fisher Scientific) ultra-high performance liquid chromatography system coupled to a Q-Exactive Focus mass spectrometer interfaced with a HESI source operating in negative ionization mode. Chromatographic separation was carried out using an Acquity UPLC HSS T3 1.8-µm 2.1 × 100 mm column. The mobile phase was composed of A = 5 mM ammonium acetate and 0.1% formic acid in H₂O and B = 0.1% formic acid in acetonitrile. Gradient elution was set as described in Supplementary Table 1. The flow rate was 350 µl min⁻¹, the column temperature was 30 °C, and the injection volume was 20 µl. Mass spectrometry parameters were set to: full scan in narrow mass range of *m/z* 370–522, mass resolving power of 70,000 full width at half maximum, and an automatic gain control target of 5e5. Data were processed as described previously³⁹. BA concentrations were reported to the protein concentration.

Statistics. Differences between two groups were assessed using two-tailed *t*-tests. Differences between more than two groups were assessed using ANOVA. To compare the interaction between two factors, two-way ANOVA post hoc corrections were performed. ANOVA, assessed by Bonferroni's post hoc correction, was used when comparing more than two groups. GraphPad Prism 9 was used for all statistical analyses. The studies were either replicated or the results were confirmed by using different approaches (RT-qPCR, western blot and immunohistochemistry) yielding similar results. All *P* values ≤ 0.05 were considered significant. **P* ≤ 0.05, ***P* ≤ 0.01, ****P* ≤ 0.001 and *****P* ≤ 0.0001.

Reporting Summary. Further information on research design is available in the Nature Research Reporting Summary linked to this article.

Data availability

All the datasets generated during the current study are available upon request to the corresponding author. Source data are provided with this paper.

Received: 13 September 2020; Accepted: 26 April 2021;
Published online: 24 May 2021

References

- McMillin, M. & DeMorrow, S. Effects of bile acids on neurological function and disease. *FASEB J.* **30**, 3658–3668 (2016).

- Kawamata, Y. et al. A G-protein-coupled receptor responsive to bile acids. *J. Biol. Chem.* **278**, 9435–9440 (2003).
- Watanabe, M. et al. Bile acids induce energy expenditure by promoting intracellular thyroid hormone activation. *Nature* **439**, 484–489 (2006).
- Thomas, C. et al. TGR5-mediated bile acid sensing controls glucose homeostasis. *Cell Metab.* **10**, 167–177 (2009).
- Pols, T. W. H. et al. TGR5 activation inhibits atherosclerosis by reducing macrophage inflammation and lipid loading. *Cell Metab.* **14**, 747–757 (2011).
- Perino, A. et al. TGR5 reduces macrophage migration through mTOR-induced C/EBPβ differential translation. *J. Clin. Invest.* **124**, 5424–5436 (2014).
- Velazquez-Villegas, L. A. et al. TGR5 signalling promotes mitochondrial fission and beige remodelling of white adipose tissue. *Nat. Commun.* **9**, 245 (2018).
- Perino, A., Demagny, H., Velazquez-Villegas, L. A. & Schoonjans, K. Molecular physiology of bile acid signaling in health, disease and aging. *Physiol. Rev.* **101**, 683–731 (2020).
- Angelin, B., Björkhem, I., Einarsson, K. & Ewerth, S. Hepatic uptake of bile acids in man. Fasting and postprandial concentrations of individual bile acids in portal venous and systemic blood serum. *J. Clin. Invest.* **70**, 724–731 (1982).
- Higashi, T. et al. Unconjugated bile acids in rat brain: analytical method based on LC/ESI-MS/MS with chemical derivatization and estimation of their origin by comparison to serum levels. *Steroids* **125**, 107–113 (2017).
- Mano, N. et al. Presence of protein-bound unconjugated bile acids in the cytoplasmic fraction of rat brain. *J. Lipid Res.* **45**, 295–300 (2004).
- Zheng, X. et al. The brain metabolome of male rats across the lifespan. *Sci. Rep.* **6**, 24125 (2016).
- Kiriya, Y. & Nochi, H. The biosynthesis, signaling and neurological functions of bile acids. *Biomolecules* **9**, 232 (2019).
- Lorbek, G., Lewinska, M. & Rozman, D. Cytochrome P450s in the synthesis of cholesterol and bile acids—from mouse models to human diseases. *FEBS J.* **279**, 1516–1533 (2012).
- Yanguas-Casas, N., Barreda-Manso, M. A., Nieto-Sampedro, M. & Romero-Ramírez, L. TUDCA: an agonist of the bile acid receptor GPBAR1/TGR5 with anti-inflammatory effects in microglial cells. *J. Cell. Physiol.* **232**, 2231–2245 (2017).
- Keitel, V. et al. The bile acid receptor TGR5 (Gpbar-1) acts as a neurosteroid receptor in brain. *Glia* **58**, 1794–1805 (2010).
- Pellicciari, R. et al. Discovery of 6α-ethyl-23(S)-methylcholic acid (S-EMCA, INT-777) as a potent and selective agonist for the TGR5 receptor, a novel target for diabetes. *J. Med. Chem.* **52**, 7958–7961 (2009).
- Waterson, M. J. & Horvath, T. L. Neuronal regulation of energy homeostasis: beyond the hypothalamus and feeding. *Cell Metab.* **22**, 962–970 (2015).
- Schöne, C. & Burdakov, D. Glutamate and GABA as rapid effectors of hypothalamic 'peptidergic' neurons. *Front. Behav. Neurosci.* **6**, 81 (2012).
- Meunier, F. A. & Gutiérrez, L. M. Captivating new roles of F-actin cortex in exocytosis and bulk endocytosis in neurosecretory cells. *Trends Neurosci.* **39**, 605–613 (2016).
- Amano, M., Nakayama, M. & Kaibuchi, K. Rho-kinase/ROCK: a key regulator of the cytoskeleton and cell polarity. *Cytoskeleton* **67**, 545–554 (2010).
- Sit, S.-T. & Manser, E. Rho GTPases and their role in organizing the actin cytoskeleton. *J. Cell Sci.* **124**, 679–683 (2011).
- Symons, M. & Rusk, N. Control of vesicular trafficking by Rho GTPases. *Curr. Biol.* **13**, R409–R418 (2003).
- Wolf, M. et al. ADF/cofilin controls synaptic actin dynamics and regulates synaptic vesicle mobilization and exocytosis. *Cereb. Cortex* **25**, 2863–2875 (2015).
- Varela, L. & Horvath, T. L. Leptin and insulin pathways in POMC and AgRP neurons that modulate energy balance and glucose homeostasis. *EMBO Rep.* **13**, 1079–1086 (2012).
- Perino, A. & Schoonjans, K. TGR5 and immunometabolism: insights from physiology and pharmacology. *Trends Pharmacol. Sci.* **36**, 847–857 (2015).
- Orskov, C., Poulsen, S. S., Møller, M. & Holst, J. J. Glucagon-like peptide-1 receptors in the subfornical organ and the area postrema are accessible to circulating glucagon-like peptide-1. *Diabetes* **45**, 832–835 (1996).
- Yamamoto, H. et al. Glucagon-like peptide-1-responsive catecholamine neurons in the area postrema link peripheral glucagon-like peptide-1 with central autonomic control sites. *J. Neurosci.* **23**, 2939–2946 (2003).
- Rüttimann, E. B., Arnold, M., Hillebrand, J. J., Geary, N. & Langhans, W. Intrameal hepatic portal and intraperitoneal infusions of glucagon-like peptide-1 reduce spontaneous meal size in the rat via different mechanisms. *Endocrinology* **150**, 1174–1181 (2009).
- Wu, X. et al. Satiety induced by bile acids is mediated via vagal afferent pathways. *JCI Insight* **5**, e132400 (2020).
- Pinto, S. et al. Rapid rewiring of arcuate nucleus feeding circuits by leptin. *Science* **304**, 110–115 (2004).
- Zhu, Y. et al. Ablation of NF1 function in neurons induces abnormal development of cerebral cortex and reactive gliosis in the brain. *Genes Dev.* **15**, 859–876 (2001).

33. Tong, Q., Ye, C.-P., Jones, J. E., Elmquist, J. K. & Lowell, B. B. Synaptic release of GABA by AgRP neurons is required for normal regulation of energy balance. *Nat. Neurosci.* **11**, 998–1000 (2008).
34. Balthasar, N. et al. Leptin receptor signaling in POMC neurons is required for normal body weight homeostasis. *Neuron* **42**, 983–991 (2004).
35. Argmann, C. A., Champy, M.-F. & Auwerx, J. Evaluation of energy homeostasis. *Curr. Protoc. Mol. Biol.* **29**, 29B.1 (2006).
36. Paxinos, G. & Franklin, K. B. J. *The Mouse Brain in Stereotaxic Coordinates: Compact Second Edition* (Academic Press, 2003).
37. Bellocchio, L. et al. Activation of the sympathetic nervous system mediates hypophagic and anxiety-like effects of CB₁ receptor blockade. *Proc. Natl Acad. Sci. USA* **110**, 4786–4791 (2013).
38. Saucisse, N. et al. POMC neurons functional heterogeneity relies on mTORC1 signaling. Preprint at *bioRxiv* <http://biorxiv.org/lookup/doi/10.1101/2020.03.25.007765> (2020).
39. Sorrentino, G. et al. Bile acids signal via TGR5 to activate intestinal stem cells and epithelial regeneration. *Gastroenterology* **159**, 956–968.e8 (2020).

Acknowledgements

We thank A. Fouassier, S. Bichet, T. Clerc, P. Colin, A. Aebi, T. Teav (Metabolomics Platform), the Histology facility and the Phenotyping Unit (UDP) for technical assistance, the Mouse Clinical Institute in Strasbourg for the generation of the TGR5:GFP mouse strain, and the Bordeaux Imaging Center (CNRS-INSERM and Bordeaux University; ANR-10-INBS-04) for confocal microscopy. This work was funded by the Swiss National Science Foundation (SNSF nos. 310030_189178 and CRSII5_180317/1, the Kristian Gerhard Jebsen Foundation and the Ecole Polytechnique Fédérale de Lausanne (EPFL; to K.S.), the National Institutes of Health (DK097566 to S.D.) and INSERM, ANR-17-CE14-0007, ANR-10-EQX-008-1 OPTOPATH (to D.C.). L.A.V.-V. and A.P. were supported by a postdoctoral fellowship from the AXA Research Fund.

Author contributions

A.P., L.A.V.-V. and K.S. conceived and designed the project. B.S., S.D. and D.C. provided critical expertise. A.G. and R.P. provided chemical compounds. A.P., L.A.V.-V., N.B., Y.S., Q.H., V.F., A.C.-J., P.Z., G.B., S.J. and A.B. performed experiments. A.P., L.A.V.-V., N.B., V.F., A.C.-J., P.Z., G.B., S.J. and J.I. analysed the data. A.P., L.A.V.-V. and K.S. wrote the manuscript. All the authors read and approved the manuscript.

Competing interests

A.G. and R.P. are cofounders of TES Pharma. R.P. is the president and CEO of TES Pharma. The other authors declare no competing interests.

Additional information

Extended data is available for this paper at <https://doi.org/10.1038/s42255-021-00398-4>.

Supplementary information The online version contains supplementary material available at <https://doi.org/10.1038/s42255-021-00398-4>.

Correspondence and requests for materials should be addressed to K.S.

Peer review information *Nature Metabolism* thanks Richard Palmiter and the other, anonymous, reviewer(s) for their contribution to the peer review of this work. Primary Handling Editor: Christoph Schmitt.

Reprints and permissions information is available at www.nature.com/reprints.

Publisher's note Springer Nature remains neutral with regard to jurisdictional claims in published maps and institutional affiliations.

© The Author(s), under exclusive licence to Springer Nature Limited 2021